REYNOLDS AND MACH NUMBER SCALING IN STATIONARY COMPRESSIBLE TURBULENCE USING MASSIVELY PARALLEL HIGH RESOLUTION DIRECT NUMERICAL SIMULATIONS

A Dissertation

by

SHRIRAM JAGANNATHAN

Submitted to the Office of Graduate and Professional Studies of
Texas A&M University
in partial fulfillment of the requirements for the degree of

DOCTOR OF PHILOSOPHY

Chair of Committee,	Diego A. Donzis
Committee Members,	Sharath Girimaji
	Rodney D. W. Bowersox
	Nancy M. Amato
Head of Department,	Rodney D. W. Bowersox

August 2014

Major Subject: Aerospace Engineering

ABSTRACT

Turbulence is the most common state of fluid motion in both natural and engineering systems. Many real world applications depend on our ability to predict and control turbulent processes. Due to the presence of both hydrodynamic and thermodynamic fluctuations, simulations of compressible flows are more expensive than incompressible flows. A highly scalable code is presented which is used to perform direct numerical simulations (DNS) aimed at understanding fundamental turbulent processes. The code is parallelized using both distributed and shared memory paradigms and is shown to scale well up to 264144 cores. The code is used to generate a large database of stationary compressible turbulence at world-record resolutions and a range of Reynolds and Mach numbers, and different forcing schemes to investigate the effect of compressibility on classical scaling relations, to study the role of thermodynamic fluctuations and energy exchanges between the internal and kinetic modes of energy, and to investigate the plausibility of a universal behavior in compressible flows. We find that pressure has a qualitatively different behavior at low and high levels of compressibility. The observed change in the likelihood of positive or negative fluctuations of pressure impacts the direction of energy transfer between internal and kinetic energy. We generalize scaling relations to different production mechanisms, and discover a plausible universal behavior for compressible flows, which could provide a path to successful modeling of turbulence in compressible flows. Our results, unprecedented in size, accuracy and range of parameters will be helpful in addressing a number of additional open issues in turbulence research.

To my parents and sister,

ACKNOWLEDGEMENTS

This work was supported by the National Science Foundation (grant OCI-1054966). The computational resources of NICS (University of Tennessee), Extreme Science and Engineering Discovery Environment (XSEDE), TACC (University of Texas at Austin), Oak Ridge and Argonne National Laboratories were used to perform our simulations.

I would like to express my thanks and gratitude to my advisor, Prof. Donzis, for his constant support and encouragement throughout my PhD. His expertise in Linux, scientific computing and turbulence, and the tenor with which he pursues excellence in every endeavor, has left with me a constant admiration for his talent and commitment. His humility and professional ethics have also been a great inspiration for me. I did not have to look any further for a dedicated mentor and an inspirational role model. I am also thankful to him for giving me plenty of opportunities to interact with some of the eminent scholars in the field of turbulence.

I would also like to thank the inspirational teachers, T.R.S and Dr. Salih, with whom I have had the pleasure of interacting with. Their knowledge in the subject and rigor in the pursuit of perfection commands every bit of my respect. I am also thankful to Drs. Bowersox, Girimaji and Amato for agreeing to be part of my committee. I am especially thankful to Dr. Girimaji for giving a very conceptual introduction to turbulence in his course and occasional help.

I also thank the consultants at NICS and XSEDE for their timely support and help. I am thankful to the staff at Argonne National Lab for their hospitality and

warm welcome during the Leap-to-Petascale workshop. A big thanks to an extremely supportive and warm staff of our Department, Ms. Leatherman, Ms. Knabe and Ms. Gilbert. For their timely help in resolving IT issues, I am thankful to Mr. Munnerlyn and Mr. Pollard. Many thanks to the Scholarships and Financial Aid at Texas A&M University for constantly supporting me with scholarships.

To my animated and lively lab-mates Agustin and Aditya, thanks for being very supportive and making this journey more cheerful, and to Chang-Hsin and Sualeh for their occasional help. The coffee hour discussions with Pratanu, Vishnu and Pooyan will always be something that I remember. My special thanks to Vijay, Vivek, Siddhartha, Rajsekar, Somasundaram, Madhuri and Nandita for all the lively conversations and friendly banters that we have had for years. These are memories I shall cherish for years to come. And a big thanks to the innumerable number of friends who made this possible (Radhi, Raga, Siva, Srini, Vishal, Yeshwanth, Malini, Venky, Ashwin.N, Prasanna, Preethi, Sandhya, Ashwin.P, Shriram, Harsha). And for all the help when times weren't great, thanks to Milind, Pradeep, and UV who motivated me as often as they could.

I am very grateful and shall remain indebted to everyone who helped me during my ailment. My special thanks to Madhuri's and Vijay's parents and my sister for extending their help when I needed the most. Words fail me when I try to express how much I owe you all.

Finally, I am most thankful to my parents and sister for their boundless love and emotional support.

TABLE OF CONTENTS

Page

CHAPTER Page

CHAPTER Page

LIST OF FIGURES

FIGURE Page

FIGURE Page

LIST OF TABLES

CHAPTER I

INTRODUCTION

I.A. Turbulence: An Overview

Turbulence is the most common state of fluid motion and an ubiquitous phenomenon in natural and engineering systems. Understanding turbulent processes has real world applications including aerospace sciences, climate modeling and hypersonic flows among others. However, a complete understanding of it is still lacking, in part, due to the randomness and non-linearity associated with the governing equations of motion, known as the Navier-Stokes equation. This randomness, associated with the chaotic nature of the solutions, makes the velocity field sensitive to initial conditions, in the sense that a small change in the initial conditions could bring a large variation in the motion of the fluid. This poses a great challenge to experimentalists since infinitesimal changes in flow conditions, that are inevitable, are amplified by the flow and evolve differently. The non-linear nature of the equation has two profound impacts: *a*) makes exact solution of the complete Navier-Stokes equation very difficult to derive unless simplifying assumptions are made, *b*) creates a wide range of spatial and temporal scales. The multiplicity of scales makes it a computationally demanding problem since all the scales, including the smallest in time and space, needs to be resolved.

Though the velocity field is chaotic, it has been observed that when the experiments are repeated under the same initial conditions, the statistical properties of

the flow field change very little. Hence it is not surprising that the theories so far had to contend with statistical rather than deterministic methods.

Flows can typically be classified as incompressible or compressible depending on whether the fluid elements preserve their volume or not. While in the former, density and temperature fluctuations are entirely decoupled from the hydrodynamics, they are coupled in the latter case. This additional level of complexity in flows that are already turbulent makes compressible turbulence a very challenging problem from theoretical, experimental and numerical perspectives. Hence, understanding and advancements in compressible flows have been much slower than its incompressible counterpart. Here, we aim to numerically investigate the effects of compressibility in a homogeneous isotropic turbulent flow where the anisotropy and wall effects are not present.

I.B. Background and Literature Review: Compressible Flows

Compressible flows, as mentioned before, are characterized by fluctuations in velocity, pressure, density and temperature over a wide range of spatial and temporal scales. Both the ranges widen with Reynolds number (R_λ), a measure of inertial to viscous forces, which is very high for practical applications. They need to be resolved completely, up to the smallest dynamically relevant scales if all the details in the flow are to be captured. The domain size must be larger than the largest scale in the flow and the grid size smaller than the smallest scale. Similarly, the simulated time must be longer than the slowest time scale and time step smaller than the fastest time scale. Simulations that satisfy this criteria are known as Direct

Numerical Simulation (DNS) and has been a unique scientific tool in understanding turbulent flows (Moin & Mahesh, 1998). Such stringent resolution requirement grow with R_λ^6, demanding a steep increase in computational resource, for instance, to double the Reynolds number the computational work has to increase sixty four times. They demand robust numerical schemes and highly scalable parallel algorithms with minimal communication. Rapid advancements in computing power has made large simulations possible which currently allow us to reach Reynolds numbers much closer to real application than previously thought. As the Reynolds number is increased new physics in turbulence is unraveled; but increasing the Reynolds number, increases the resolution requirement further emphasizing the need for exceptional computational algorithms and tools.

The general disposition towards accounting for compressibility effects has been to decompose the velocity field into an incompressible (solenoidal) and compressible (dilatational) component based on Helmholtz decomposition. A similar form of decomposition has been extended to, though its definition is somewhat arbitrary, pressure. Other attempts have also been made to isolate compressiblity effects. For instance, Kovasznay (1953) linearized the Navier-Stokes equation to obtain the solution as superposition of vorticity, entropy and acoustic modes under the assumption that extent of compressibility is very small. Chu & Kovásznay (1958) extended the analysis as a second-order approximation to account for stronger compressiblility effects. Dastgeer & Zank (2005) employed a similar approach. This assumption, however, is very restrictive for a large class of engineering flows that operate at high speeds. Since, the Helmholtz decomposition provides an easy and unambiguous

means to account for the effects of compressiblility through the dilatational component, we employ this decomposition in the present study.

The thermodynamic variables are related by equation of state for an ideal gas and are accompanied by acoustic phenomenon, such as, propagation of sound waves. Depending on the level of compressibility, which is commonly quantified in a large manner by the turbulent Mach number ($M_t = \langle u_i u_i \rangle / \langle c \rangle$, summation implied and $\langle c \rangle$ is the mean speed of sound), different approximations can be made that lead to distinct flow regimes. For instance, at low M_t, the acoustic time scale is much smaller than the convective and viscous time scale. Thus the viscous and heat conduction terms in Navier-Stokes equation remain relatively unaffected based on the acoustic time scale leading to a simplified set of equations (Erlebacher *et al.*, 1990; Sarkar *et al.*, 1991). This leads to a flow regime known as low-Mach number quasi-isentropic regime, where the flow evolves only on acoustic time scale and characterized by small dilatational fluctuations (Sagaut & Cambon, 2008). Under these conditions, Sarkar *et al.* (1991) observed an equipartition of energy between the compressible kinetic energy and potential energy due to the pressure. The phenomenon of equipartition, has been verified by simulations of decaying turbulence (Lee & Girimaji, 2013) and in shear flows (Bertsch *et al.*, 2012) for low M_t. However, at higher levels of compressibility, the dilatational fluctuations are substantial and cannot be neglected. Furthermore, the different timescales become comparable. This flow regime, where the dilatational fluctuations are significant and Mach number is still less than one, is classified as non-linear subsonic regime and is the principal regime of investigation in this paper.

A basic yet very fundamental aspect of turbulence is the presence of a wide range of length scales, the smallest of which are known as Kolmogorov microscales. While its scaling have been verified extensively in incompressible turbulence (Ishihara *et al.*, 2009), there isn't enough evidence yet to suggest that the effects of compressibility are weak. As we will show in Ch III, the scaling of the Kolmogorov microscales remain intact in compressible flows for M_t as high as 0.6.

At low Mach numbers, compressible turbulence exhibits certain characteristic similar to its incompressible counterpart. For instance, at sufficiently high Reynolds number, the mean energy dissipation rate becomes independent of the fluid viscosity in incompressible turbulence ($D \equiv \langle\epsilon\rangle u^3/L$). This phenomenon, often known as dissipative anomaly, is central to the dynamics of energy cascade and has been verified over the past several years (Sreenivasan, 1984, 1998; Kaneda *et al.*, 2003; Donzis *et al.*, 2005). However, it is still not well-reported in the literature whether D asymptotes to a constant at high Reynolds and Mach number, and if it does, the asymptotic magnitude is not clear. Much like velocity and pressure, the mean dissipation rate can be decomposed into a solenoidal ($\langle\epsilon^s\rangle$) and dilatational ($\langle\epsilon^d\rangle$) component and a similar constant can also be established for each.

Employing this type of decomposition for dissipation rate, and based on the asymptotic analysis of Navier-Stokes equation by Erlebacher *et al.* (1990), Sarkar *et al.* (1991) derived a model for the dilatational dissipation rate in the low-Mach number regime ($\epsilon^d \propto M_t^2\epsilon^s$). Available literature suggest $\langle\epsilon^d\rangle/\langle\epsilon^s\rangle$ scale as M_t^2 based on an EDQNM analysis at low Mach numbers (Bertoglio *et al.*, 2001), M_t^4 based on statistical analysis (Ristorcelli, 1997; Fauchet & Bertoglio, 1998) and also M_t^5 at high

turbulent Mach numbers using EDQNM approximation (Sagaut & Cambon, 2008). Some of these results have been validated only at low Mach and Reynolds number using simulations of decaying compressible turbulence that could possibly have the signature of initial conditions (Ristorcelli, 1997; Vreman *et al.*, 1996) or with an EDQNM approximation (Bertoglio *et al.*, 2001) that assumes (mention disadvantages of EDQNM here). One of the ways of removing the dependence on initial condition is to force the simulation by energizing the large scales of motion so that a statistically stationary state is achieved. This forms the basis of our work.

The dissipation rate also appears in the volume averaged energy budget equation and thus dictates the unidirectional energy transfer from kinetic to internal energy modes. Another term that appears in the budget equation, that is native only to compressible flows, is the correlation between pressure and dilatation, often known as pressure-dilatation correlation ($p'\theta'$). Unlike dissipation rate, the latter facilitates a bi-directional energy exchange between the internal and kinetic energy modes. It is also easily perceivable that any influence of compressibility in pressure fluctuation, could bring about changes in pressure-dilatation correlation and consequently the way energy is exchanged, affecting the global dynamics of flow. Thus it is very important to understand the effects of compressiblity on the behavior of pressure, for example, by investigating some of the basic scaling relations. In the low M_t limit, Sarkar *et al.* (1991) assumed the normalized solenoidal and dilatational pressure fluctuations scale as M_t^2, however it has not been verified by simulations or the range of M_t for which it is valid. The probability distribution function (PDF) of pressure (f_p), for instance, is negatively skewed at low M_t, but tends to be positively skewed

at high M_t (Donzis & Jagannathan, 2013a). While it can be trivially explained from Reynolds decomposition that p' is likely to take more positive values than negative, a physical reasoning is still lacking. We attempt to provide some physical arguments for these qualitative changes in the flow. This is our second major objective, to build a large database of compressible isotropic turbulence and investigate separately, the effects of Reynolds and Mach number on the scaling relations in compressible turbulence.

A phenomenon that is unique to compressible flows is the presence of compressing and expanding regions in the flow. These are purely dilatational motions which could interact with the incompressible (or solenoidal) motions (Lele, 1994). The need to understand the role of each component and develop models that can reproduce the observed behavior, has led to several decades of analytical, experimental and numerical efforts (Sagaut & Cambon, 2008). Yet, the scaling of these different components is currently unknown at realistic conditions, largely, because of lack of reliable data especially at high Reynolds numbers and at a range of Mach numbers. Dilatational modes, could give rise to so-called shocklets–very strong local compressions randomly distributed in space which possess some of the characteristics of shock waves (Lee *et al.*, 1991; Samtaney *et al.*, 2001; Pirozzoli & Grasso, 2004). How these intense fluctuations, and compressibility in general, affect classical similarity theories (Kolmogorov, 1941) for incompressible flows is an important step towards a general understanding of high-Reynolds number compressible flows.

I.C. Objective of the Present Work

The objectives of the current work are to:

1. develop a massively parallel code that solves the compressible Navier-Stokes equation and is scalable across different platforms

2. generate a large database of stationary compressible turbulence at different R_λ and M_t and to identify their effects independently

3. study how classical scaling relations are affected by compressibility and investigate their dependence on the mode of forcing

4. understand how thermodynamic fluctuations and dilatation of the fluid affect the flow statistics.

5. understand how compressibility effects can be accounted for in homogeneous compressible flows

CHAPTER II

DIRECT NUMERICAL SIMULATIONS*

II.A. Computational Approach

II.A.1. Numerical Scheme and Accuracy

Turbulence is governed by the conservation of mass, momentum and energy, also known as Navier-Stokes equations and are:

$$\frac{\partial \rho}{\partial t} + \frac{\partial}{\partial x_i}\left(\rho u_i\right) = 0, \tag{2.1}$$

$$\frac{\partial}{\partial t}\left(\rho u_i\right) + \frac{\partial}{\partial x_j}\left(\rho u_i u_j\right) = -\frac{\partial p}{\partial x_i} + \frac{\partial}{\partial x_j}\left(\sigma_{ij}\right) + \rho f_i, \tag{2.2}$$

$$\frac{\partial}{\partial t}\left(\rho e\right) + \frac{\partial}{\partial x_i}\left(\rho e u_i\right) = -p\frac{\partial u_i}{\partial x_i} + \frac{\partial}{\partial x_i}\left(k\frac{\partial T}{\partial x_i}\right) + \sigma_{ij}S_{ij} - \Lambda. \tag{2.3}$$

where, ρ is density, u_i is the i^{th} component of velocity, p is pressure, e is internal energy per unit mass, T is temperature, k is thermal conductivity and f_i is the external forcing. The viscous stress tensor, σ_{ij}, and strain rate tensor, S_{ij}, are given by,

$$\sigma_{ij} = \mu\left(\frac{\partial u_i}{\partial x_j} + \frac{\partial u_j}{\partial x_i} - \frac{2}{3}\delta_{ij}\frac{\partial u_k}{\partial x_k}\right), \tag{2.4}$$

$$S_{ij} = \frac{1}{2}\left(\frac{\partial u_i}{\partial x_j} + \frac{\partial u_j}{\partial x_i}\right). \tag{2.5}$$

The internal energy per unit mass, e, is related to temperature according to a perfect gas law and the viscosity, μ, has a power-law dependence on temperature.

---

*Reprinted with permissions from Jagannathan, S. & Donzis, D. A. 2012 Massively parallel direct numerical simulations of forced compressible turbulence: a hybrid MPI/OpenMP approach. In XSEDE 2012 Conference, Chicago, IL, July 16-20.

Because of the multi-scale nature of turbulence, numerical methods capable of capturing a wide range of scales are needed. While spectral codes present unique resolution capabilities and have therefore been extensively used in incompressible simulations (Ishihara *et al.*, 2009), the appearances of shocklets may give rise to spurious oscillations due to Gibbs phenomenon (Canuto *et al.*, 1988). Furthermore, handling more complex geometries as well as boundary conditions (other than periodic as in practical flows) may require a different discretization.

An alternative to spectral schemes is based on the so-called compact finite differences which exhibit spectral-like resolution but provide more flexibility in terms of geometrical features of the domain as well as boundary conditions, a common feature of finite difference approaches. However, depending on the order of the scheme, the range of scales that can be effectively resolved, is much wider than conventional explicit finite differences (Lele, 1992). Thus, compact schemes has been widely used in simulations of multi-scale phenomena with a broadband spectral support such as turbulence, especially at high Reynolds numbers.

Formally, for a function f a general representation of its derivative (denoted with a prime) at a general location x_i can be computed in terms of finite differences according to

$$\sum_{j=-m}^{m} \alpha_j f'_{i+j} = \sum_{j=-n}^{n} a_j f_{i+j}, \tag{2.6}$$

where α_j, a_j are the coefficients of the stencil, m and n define the stencil size. Clearly if $m = 0$, the left-hand side consists of f' only at the location of interest and the result is a classical explicit finite difference formulation. If $m > 0$, the left-hand-side consists of a linear combination of the value of the derivative at neighboring

locations. The result is a linear system of equations of the form $\mathbf{Af}' = \mathbf{Bf}$. Different orders in the truncation error can be achieved by changing the size of the stencils m and n. Depending on the type of grid distribution, boundary conditions and the number of stencil points (m and n), a family of schemes can be obtained. Specifically, for uniform grids with periodic boundary condition and $m = 1$ and $n = 2$, a widely used sixth order accurate scheme is obtained (e.g. (Lee *et al.*, 1991, 1993; Petersen & Livescu, 2010)). This is, in fact, the maximum accuracy that can be achieved with a tridiagonal system (Lele, 1992). For $m = 2$ and $n = 3$ one obtains a tenth-order scheme with a penta-diagonal system of equations (Lele, 1992). The higher the order of the scheme, the wider the range of scales that can be accurately resolved numerically. Because our interest in capturing all dynamically relevant scales as accurately as possible, we use a tenth-order scheme for the present work. It is also important to note that depending on the problems of interest one may require a non-uniform distribution of grid spacing. It is possible to extend the compact schemes for arbitrarily spaced grids (Gamet *et al.*, 1999). However, due to the variable grid spacing, the coefficients α_j and a_j will depend on the grid spacing. In general, it may not be possible to realize the equivalent highest order of accuracy that is obtained on a uniform grid.

In the forthcoming section, we will briefly describe the numerical schemes used for different grid configurations and boundary conditions.

II.A.1.a. Uniform grids with periodic boundary conditions

For uniform grids with periodic boundary conditions, the coefficients α_j and a_j change only with the number of stencil points (m, n). For a sixth order scheme, this leads to,

$$\alpha_{-1} f'_{i-1} + \alpha_0 f'_i + \alpha_1 f'_{i+1} = a_{-2} f_{i-2} + a_{-1} f_{i-1} + a_0 f_i + a_1 f_{i+1} + a_2 f_{i+2}, \tag{2.7}$$

where the coefficients $\alpha_{-1} = \alpha_1 = 1/3$, $\alpha_0 = 1$, and $a_{-2} = a_2 = 1/36\Delta h$, $a_{-1} = a_1 = 7/9\Delta h$, $a_0 = 0$. This leads to a system of equations of the form $\mathbf{A}\mathbf{f}' = \mathbf{b}$, where matrices $\mathbf{A}$ and $\mathbf{B}$ are given by,

$$A = \begin{pmatrix} \alpha_0 & \alpha_1 & 0 & 0 & \cdots & \boxed{\alpha_{-1}} \\ \alpha_{-1} & \alpha_0 & \alpha_1 & 0 & 0 & \cdots \\ 0 & \alpha_{-1} & \alpha_0 & \alpha_1 & 0 & \cdots \\ \vdots & 0 & \alpha_{-1} & \alpha_0 & \alpha_1 & \cdots \\ \boxed{\alpha_1} & \ddots & \ddots & \ddots & \alpha_{-1} & \alpha_0 \end{pmatrix} \tag{2.8}$$

$$B = \begin{pmatrix} a_0 & a_1 & a_2 & \cdots & a_{-2} & a_{-1} \\ a_{-1} & a_0 & a_1 & a_2 & \cdots & a_{-2} \\ a_{-2} & a_{-1} & a_0 & a_1 & a_2 & \cdots \\ \cdots & \ddots & \ddots & \ddots & \ddots & \cdots \\ a_1 & \cdots & a_{-2} & a_{-1} & a_0 & a_1 \\ a_2 & a_1 & \cdots & a_{-2} & a_{-1} & a_0 \end{pmatrix} \tag{2.9}$$

and $\mathbf{b} = \mathbf{B}\mathbf{f}$. The matrix $\mathbf{A}$ is of the cyclic tri-diagonal form which resembles a tri-diagonal matrix except for the boxed terms that arise due to the periodic boundary condition: ($f_{N+i} = f_i, f_{1-i} = f_{N-i+1}$) and similarly for the derivatives f' which is

seen in matrix **B**. The matrix A can be written as sum of two matrices $\mathbf{A_1}$ and $\mathbf{A_2}$ where $\mathbf{A_1}$ would retain the tridiagonal system and the sparse $\mathbf{A_2}$ matrix comprising of only boxed terms and rest zeros. The solution for matrices of this form can be obtained using the Shermann-Morrison formula (**?**) where $\mathbf{A_2}$ is written as a kronecker product of two one dimensional vectors, **u** and **v** that are given as,

$$\mathbf{u} = \begin{pmatrix} \gamma \\ 0 \\ \vdots \\ 0 \\ \alpha_1 \end{pmatrix} \mathbf{v} = \begin{pmatrix} \alpha_0 \\ 0 \\ \vdots \\ 0 \\ \alpha_{-1}/\gamma \end{pmatrix}, \tag{2.10}$$

where γ is an arbitrary constant. This reduces to $(\mathbf{A_1} + (\mathbf{u} \otimes \mathbf{v}))\mathbf{x} = \mathbf{b}$, the solutions to which are given below,

$$\mathbf{A_1}\,\mathbf{y} = \mathbf{b},\ \mathbf{A_1}\,\mathbf{z} = \mathbf{u}, \tag{2.11}$$

where **x**, **y**, **z** are related by,

$$\mathbf{x} = \mathbf{y} - \left[\frac{\mathbf{v}\cdot\mathbf{y}}{1 + \mathbf{v}\cdot\mathbf{z}}\right]\mathbf{z} \tag{2.12}$$

Since the vector **u** is independent of the value of the function itself, the solution to $\mathbf{A_1}\,\mathbf{z}$=**u** has to be computed only once, while that of $\mathbf{A_1}\,\mathbf{y}$=**b** is computed every time-step. The solution for the latter can be easily obtained from the tri-diagonal matrix algorithm and is readily available in numerical algebra packages like LAPACK.

As mentioned before, for $m = 2$ and $n = 3$, we arrive at a tenth order scheme (Lele, 1992),

$$\begin{aligned} \alpha_{-2}f'_{i-2} + \alpha_{-1}f'_{i-1} + \alpha_0 f'_i + \alpha_1 f'_{i+1} + \alpha_2 f'_{i+2} = a_{-3}f_{i-3} + a_{-2}f_{i-2} + a_{-1}f_{i-1} \\ + a_0 f_i + a_1 f_{i+1} + a_2 f_{i+2} + a_3 f_{i+3}, \end{aligned} \tag{2.13}$$

where the coefficients are $\alpha_{-2} = \alpha_2 = 1/20$, $\alpha_{-1} = \alpha_1 = 1/2$, $\alpha_0 = 1$, and $a_{-3} = a_3 = 1/600\Delta h$, $a_{-2} = a_2 = 101/600\Delta h$, $a_{-1} = a_1 = 17/24\Delta h$, $a_0 = 0$. The coefficients are also given in Lele (1992). This leads to a penta-diagonal matrix for $\mathbf{A}$ which can be efficiently solved following the algorithm mentioned in Lv & Le (2008). The matrices $\mathbf{A}$ and $\mathbf{B}$ are then given by,

$$A = \begin{pmatrix} \alpha_0 & \alpha_1 & \alpha_2 & 0 & \cdots & \boxed{\alpha_{-2}} & \boxed{\alpha_{-1}} \\ \alpha_{-1} & \alpha_0 & \alpha_1 & \alpha_2 & \cdots & 0 & \boxed{\alpha_{-2}} \\ \alpha_{-2} & \alpha_{-1} & \alpha_0 & \alpha_1 & \alpha_2 & \cdots & 0 \\ 0 & \alpha_{-2} & \alpha_{-1} & \alpha_0 & \alpha_1 & \alpha_2 & \cdots \\ \vdots & \ddots & \alpha_{-2} & \alpha_{-1} & \alpha_0 & \alpha_1 & \cdots \\ \boxed{\alpha_2} & 0 & \ddots & \ddots & \alpha_{-1} & \alpha_0 & \alpha_1 \\ \boxed{\alpha_1} & \boxed{\alpha_2} & \ddots & \ddots & \ddots & \alpha_{-1} & \alpha_0 \end{pmatrix} \tag{2.14}$$

$$B = \begin{pmatrix} a_0 & a_1 & a_2 & a_3 & \cdots & a_{-2} & a_{-1} \\ a_{-1} & a_0 & a_1 & a_2 & a_2 & \cdots & a_{-2} \\ a_{-2} & a_{-1} & a_0 & a_1 & a_2 & \cdots & a_{-3} \\ \cdots & \cdots & \ddots & \ddots & \ddots & \ddots & \cdots \\ a_3 & \cdots & a_{-3} & a_{-2} & a_0 & a_1 & a_2 \\ a_2 & a_3 & \cdots & a_{-2} & a_{-1} & a_0 & a_1 \\ a_1 & a_2 & a_3 & \cdots & a_{-2} & a_{-1} & a_0 \end{pmatrix} \tag{2.15}$$

A similar method is employed for computing the second derivatives,

$$\sum_{j=-m}^{m} \beta_j f'_{i+j} = \sum_{j=-n}^{n} b_j f_{i+j}, \tag{2.16}$$

where β_j, b_j are the coefficients of the stencil, and m, n are the stencil sizes. The family of schemes for second derivatives are mentioned in detail in Lele (1992) and

we discuss here only the tenth order schemes,

$$\beta_{-2}f''_{i-2} + \beta_{-1}f''_{i-1} + \beta_0 f''_i + \beta_1 f''_{i+1} + \beta_2 f''_{i+2} = b_{-3}f_{i-3} + b_{-2}f_{i-2} + b_{-1}f_{i-1} + b_0 f_i + b_1 f_{i+1} + b_2 f_{i+2} + b_3 f_{i+3}, \tag{2.17}$$

where the coefficients are $\beta_{-2} = \beta_2 = 43/1798$, $\beta_{-1} = \beta_1 = 334/899$, $\beta_0 = 1$, and $b_{-3} = b_3 = 79/16182\Delta h^2$, $b_{-2} = b_2 = 519/1798\Delta h^2$, $b_{-1} = b_1 = 1065/1798\Delta h^2$, $b_0 = 0$. The resulting system of equations, which is penta-diagonal, is then solved using the algorithm mentioned in Lv & Le (2008) in $\mathcal{O}(59n)$ operations.

II.A.1.b. Non-Uniform grids with periodic boundary conditions

For the case of non-uniform grids, as mentioned before, the coefficients α_j and a_j change with the grid spacing. The value of coefficients can be obtained by a rather inexpensive computational algorithm mentioned in Fornberg (1998). The algorithm computes derivatives of any order for both implicit and explicit schemes, however, for the latter additional fictitious points have to be considered. Since this has more relevance to the present grid, the algorithm for non-uniform grid is discussed below.

Consider that the k^{th} derivative of a function f, $\partial^k f/\partial x^k$, is to be computed at $x = z$ based on n number of stencil points for function f. Formally, this can be expressed as (Fornberg, 1998),

$$\left[\frac{d^k f}{dx^k}\right]_{x=z} \approx \sum_{i=0}^{n} c_i^k f(x_i), \tag{2.18}$$

where c_i^k are the coefficients or the weights to be determined. If the derivative of f has an implicit dependence (as in Eq. (2.16)) a fictitious point on either side of the stencil is considered and the resulting system is solved such that the coefficients for the fictitious points are zero thereby restoring the original scheme. The number

of fictitious points on either side of the right-hand side stencil is determined by the number of the stencil points for the derivatives (which is m in Eq. (2.16)) and is discussed in detail towards the end of this section. Since $m = 1$ for sixth order scheme, we will consider one fictitious point on either side of the stencil on the right-hand side. So, for a sixth order scheme, Eq. (2.16) with fictitious points becomes (refer figure II.1 for the stencil),

$$\sum_{j=-1}^{1} \alpha_j f'_{i+j} = \sum_{j=-3}^{3} a_j f_{i+j}. \tag{2.19}$$

Following Eq. (2.18), we express each derivative in terms of the value of function (as in Eq. (2.19)):

$$f'_{i-1} = \sum_{j=-3}^{3} a'_j f_{i+j}, \tag{2.20}$$

$$f'_i = \sum_{j=-3}^{3} a''_j f_{i+j}, \tag{2.21}$$

$$f'_{i+1} = \sum_{j=-3}^{3} a'''_j f_{i+j}, \tag{2.22}$$

and combine them according to Eq. (2.19),

$$\begin{aligned} \alpha_{-1} f'_{i-1} + f'_i + \alpha_1 f'_{i+1} = & \left[\sum_{j=-2, \neq 0}^{2} \left(\alpha_{-1} a'_j + a''_j + \alpha_1 a'''_j \right) f_{i+j} \right] \\ & + \left(\alpha_{-1} a'_0 + a''_0 + \alpha_1 a'''_0 \right) f_i \\ + \left(\alpha_{-1} a'_{-3} + a''_{-3} + \alpha_1 a'''_{-3} \right) f_{i-3} & + \left(\alpha_{-1} a'_3 + a''_3 + \alpha_1 a'''_3 \right) f_{i+3}. \end{aligned} \tag{2.23}$$

It is also necessary to note that in the original compact schemes (Lele, 1992), the stencil points were weighted equally on either side of the stencil points and hence we maintain that α_{-j} and α_j are same and similarly a_{-j} and a_j. We retrieve the original form of compact schemes for sixth order ($m = 2, n = 1$) when the last two

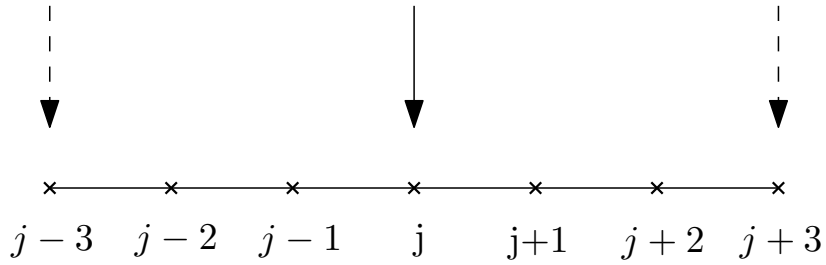

Figure II.1. A stencil of the right-hand side of Eq. (2.16) with fictitious points. The fictitious points are indicated by dotted arrows and the solid arrow indicates the point at which the derivative is sought.

terms in the RHS of Eq. (2.23) vanish and hence the coefficients of f_{i-3} and f_{i+3} are equated to zero. This gives the coefficients α_{-1} $(= \alpha_1)$ in terms of $a_j^{'}$, $a_j^{''}$, $a_j^{'''}$ which is yet to be determined. However, the coefficient of f_i is expected to have a non-vanishing contribution in the case of non-uniform grid and hence is retained (as was also done in Gamet *et al.* (1999)). This coefficient automatically approaches zero when the grid spacing is equal. The weights, $a_j^{'}, a_j^{''}, a_j^{'''}$ can be readily obtained by expanding $f_i^{'}$ using a Taylor expansion for f about the point i. This is given by the algorithm mentioned in Fornberg (1998). The need for fictitious points is clear now: they are needed to determine the coefficients α_{-1} and α_1. Suppose, one does not include fictitious points in Eq. (2.19) (i.e. if the limits for j vary from -2 to 2), it is not possible to find the coefficients α_{-1} and α_1 that could otherwise be easily obtained if fictitious points are considered. Hence the number of fictitious points to be chosen directly depends on the number of unknowns in the implicit derivative function and hence is likely to change, for instance, for tenth order schemes.

To complete the process, this procedure is repeated for all the grid points in the domain (for different i). However, this has to be done only once since the grid points, though no-uniform, does not change with time. Hence, this is done during

the initialization process in the code. When the grid spacing is uniform, the above procedure automatically returns the coefficients of the original sixth order scheme and hence can be used for both uniform and non-uniform grids types. In view of optimization, however, the code computes the coefficients only if there is a non-uniform grid type and uses the default coefficients for uniform grids. The accuracy of the sixth order scheme when applied to non-uniform grids approaches six only when the grid spacing is close to uniform. For skewed grids with large expansion or contraction coefficients, the accuracy reduces to fourth order (Gamet *et al.*, 1999).

A similar procedure could be followed for tenth order schemes, however since $m = 2$ in this case, we will have to consider two fictitious points and solve these two smaller systems in-order to find the coefficients α_1 and α_2 and subsequently other coefficients. However, when one considers two fictitious points on either side of the stencil, the system of equations result in a dependent system. Hence, the coefficients cannot be determined. It may be possible that with a different choice of fictitious points, a linear system with unique solution may exist.

II.A.1.c. Uniform grids with non-periodic boundary conditions

Though periodic boundary conditions offer easier way of computing derivatives, they are limited in scope while applying for a wide class of flows (for instance, they cannot be used in wall bounded flows like a cavity). Hence, engineering applications motivate a need for schemes that can incorporate non-periodic boundary condition. For such schemes, the leading order of truncation error can be either dispersive (odd-order schemes) or dissipative (even-order schemes) depending on the order of

schemes. While the former causes oscillations in the solutions, the latter smoothens the gradients; both of them being artifacts of the numerical scheme and thus undesirable. Hence, one needs to choose schemes such that both the errors are minimal and at the same time remain robust. For this purpose, different schemes are used for the interior and boundary nodes such that global conservation is achieved (Mahesh, 1996). For the boundary, a third order scheme is used:

$$f_1^{'} + \gamma_1 f_2^{'} = a_1 f_1 + a_2 f_2 + a_3 f_3, \quad i = 1 \tag{2.24}$$

where $\gamma_1 = 2$, $a_1 = -\left(11 + 2\gamma_1\right)/6\Delta h$, $a_2 = \left(6 - \gamma_1\right)/2\Delta h$, $a_3 = \left(2\gamma_1 - 3\right)/2\Delta h$, and Δh is the grid spacing. For the adjacent point, a the fourth order scheme of the following form is used,

$$\gamma_2 f_1^{'} + f_2^{'} + \gamma_2 f_3^{'} = b_3 f_3 - b_1 f_1, \quad i = 2, \tag{2.25}$$

with $\gamma_2 = 1/4$, $b_3 = b_1 = 3/4\Delta h$ (Mahesh, 1996). To ensure the global conservation, the following scheme is used for the next node,

$$\gamma_3 f_2^{'} + f_3^{'} + \gamma_3 f_4^{'} = c_5 f_5 + c_4 f_4 - c_2 f_2 - c_1 f_1, \quad i = 3, \tag{2.26}$$

where the coefficients are related by,

$$\gamma_3 = \frac{40\hat{\gamma} - 1}{16\left(\hat{\gamma} + 2\right)}, \quad c_1 = c_5 = \frac{\left(\gamma_3 + 2\right)}{2\Delta h}, \quad c_2 = c_4 = \frac{\left(4\gamma_3 - 1\right)}{12\Delta h}. \tag{2.27}$$

Here, $\hat{\gamma}$ is related to the scheme used in the interior grid points,

$$\hat{\gamma} f_{i-1}^{'} + f_i^{'} + \hat{\gamma} f_{i+1}^{'} = c_1(f_{j+1} - f_{j-1}) + c_2(f_{j+2} - f_{j-2}) \quad i = 4, N - 3, \tag{2.28}$$

where $\hat{\gamma}$, d_1 and d_2 are given by,

$$\hat{\gamma} = 1/3 \quad d_1 = \frac{\left(\hat{\gamma} + 2\right)}{2\Delta h}, \quad d_2 = \frac{\left(4\hat{\gamma} - 1\right)}{12\Delta h}. \tag{2.29}$$

It is evident that the maximum global error will be due to the boundary terms. After applying the above treatment for the other side of the boundary which is also non periodic ($i = N-1, N-2, N$), we arrive at the following matrix for $\mathbf{A}$ and $\mathbf{B}$,

$$A = \begin{pmatrix} 1 & \gamma_1 & 0 & 0 & 0 & 0 & \cdots & 0 \\ \gamma_2 & 1 & \gamma_2 & 0 & 0 & 0 & \cdots & 0 \\ 0 & \gamma_3 & 1 & \gamma_3 & 0 & 0 & \cdots & 0 \\ 0 & 0 & \hat{\gamma} & 1 & \hat{\gamma} & 0 & \cdots & 0 \\ 0 & 0 & 0 & \hat{\gamma} & 1 & \hat{\gamma} & \cdots & 0 \\ \vdots & \vdots & \vdots & \vdots & \ddots & \ddots & \ddots & \vdots \\ 0 & \cdots & \cdots & 0 & 0 & \gamma_2 & 1 & \gamma_2 \\ 0 & \cdots & \cdots & 0 & 0 & 0 & \gamma_1 & 1 \end{pmatrix} \tag{2.30}$$

$$B = \begin{pmatrix} a_1 & a_2 & a_3 & 0 & 0 & 0 & \cdots & 0 \\ -b_1 & 0 & b_3 & 0 & 0 & 0 & \cdots & 0 \\ -c_1 & -c_2 & 0 & c_4 & c_5 & 0 & \cdots & 0 \\ 0 & -d_1 & -d_2 & 0 & d_4 & d_5 & \cdots & 0 \\ 0 & 0 & -d_1 & -d_2 & 0 & d_4 & d_5 & \cdots \\ \vdots & \vdots & \vdots & \vdots & \vdots & \vdots & \vdots & 0 \\ 0 & 0 & 0 & 0 & 0 & -b_1 & 0 & b_3 \\ 0 & 0 & 0 & 0 & \cdots & a_3 & a_2 & a_1 \end{pmatrix} \tag{2.31}$$

This system is easier to solve than Eq. (2.8) since the cyclic terms that was previously present due to the treatment of periodic boundary condition is not present. This resembles the tri-diagonal form and can be easily solved using the Thomas algorithm.

Similar expressions can be derived for second derivatives and is mentioned in

Mahesh (1996) and Lele (1992). We mention here only the schemes used in the boundary and interior points,

$$f_1^{''} + 11 f_2^{''} = \frac{1}{\Delta h^2}\left(13 f_1 - 27 f_2 + 15 f_3 - f_4\right), \quad i = 1 \tag{2.32}$$

$$f_1^{''} + 10 f_2^{''} + f_3^{''} = \frac{12}{\Delta h^2}\left(f_1 - 2 f_2 + f_3\right), \quad i = 2 \tag{2.33}$$

$$\begin{aligned} f_{i-1}^{''} + b_1 f_i^{''} + f_{i+1}^{''} = \frac{b_2}{\Delta h^2}\left(f_{i+1} + f_{i-1}\right) + \frac{b_3}{\Delta h^2}\left(f_{i+2} + f_{i-2}\right) \\ - \frac{2 f_i}{\Delta h^2}\left(b_2 + b_3\right), \quad i = 3, N-2, \end{aligned} \tag{2.34}$$

where $b_1 = 11/2$, $b_2 = 6$, $b_3 = 3/8$. A similar set of equations are written for the other side of the boundary ($i = N, N-1$) and is then solved using the Shermann-Morrison formula (**?**) mentioned in Sec II.A.1.a.

Using some of the schemes mentioned above, it is now possible to compute the first and second derivatives in eqns Eq. (2.1)-Eq. (2.3). Considering that the flow is homogeneous, we use uniform grids in all the three directions. The tenth order scheme is used for both first and second derivatives to resolve a wide range of scales.

II.A.2. Solving the System of Equations

Eqs. (2.1)-(2.3) contain derivatives in all three directions. Therefore, Eq. (2.16) needs to be solved along those directions. After the domain is mapped into processors, the systems could be solved, in principle, by either (i) solving the system across processors or (ii) solving the linear systems in-core and transposing the data. In method (i), all the processors exchange data at their boundaries, followed by a collective communication call for a global overlap of data (Cook *et al.*, 2005). In method (ii), derivatives in one direction are computed in-core with highly optimized mathematical libraries and data is subsequently transposed so that each core holds

other direction entirely. Since a collective exchange of information involves all the processors in a communicator, they may represent a significant amount of time. However, unlike method (i), method (ii) is straightforwardly extended to banded systems with any band size or equivalently to any order of accuracy. Furthermore, while it is unclear which method will be better at extreme scales, studies show that they are, in fact, comparable in some architectures (Cook *et al.*, 2005). The code presented here is based on method (ii) and has been implemented in a modular fashion to accommodate arbitrary orders.

The non-linear terms in Eq. (2.2)-(2.3) are computed using a skew-symmetric formulation which has been shown to be robust and to have better aliasing characteristics (Blaisdell *et al.*, 1996; Ducros *et al.*, 2000). Time-advancement is performed with an explicit third-order low-storage Runge-Kutta scheme (Williamson, 1980). The time-step size is controlled with a CFL condition to avoid numerical instability.

II.A.3. Domain Decomposition and Parallelization

The domain decomposition is a crucial element in designing algorithms that can scale to extreme large number of processors. In a broad sense, the domain decomposition imposes a constraint in the maximum number of processors that can be used for a given problem size, determines the memory footprint of the code, affects the efficiency in which caches can be used, among others. However, perhaps the most important element determined by the decomposition of the domain is the interprocessor communications. In fact, for communication intensive applications, careful investigations of number and size of messages and communication patterns

may be critical to scaling codes to very high levels of parallelism.

The domain considered here is cubic with periodic boundary conditions in all three dimensions. The simplest domain decomposition for this type of domain is a 1D or "slab" decomposition that obviously restrict the number of MPI tasks M according to $M \leq N$ for a problem size of N. For a pure MPI implementation M is usually also equal to the number of cores requested, N_c. To take full advantage of available Petascale systems comprising $\mathcal{O}(10^5)$ processors, this constraint must be relaxed. Clearly a 2D domain decomposition into "pencils" enables the use of $M \leq N^2$ MPI tasks and has indeed shown very good scaling for large processor counts (Donzis *et al.*, 2008*a*). For current problems of interest at 2048^3 resolutions a 2D decomposition allows the use of over 4 million cores (or threads) which may indeed be of the same order of magnitude as those available on future Exascale systems.

The present work is based on a 2D decomposition. Equations (2.1)-(2.3) are grouped separately into terms with derivatives in directions x, y and z. The main reason for this splitting is that derivatives can be computed effectively when a pencil of data is aligned in that direction. For instance, the terms with derivatives in x are computed when the data is aligned in x. Thus, Eq. (2.16) can be solved in core using highly optimized mathematical libraries. For periodic domains like those presented here, the resulting system of equations is cyclic for which a direct solver for banded systems is used in combination with Sherman-Morrison formula (**?**) for tridiagonal systems or extensions to wider bands (Lv & Le, 2008). Since the factorization step can be done at the beginning of the simulation, the solution of the necessary systems

requires only $\mathcal{O}(N)$ operations.

To compute the derivatives in y, a collective communication call (specifically MPI_ALLTOALL) is used and the data is transposed from x to y as shown in figure II.2. Two different communicators along directions y and z are defined for this purpose. Since collective calls are typically expensive and forces synchronization across processors in that communicator, it is highly desirable to achieve high levels of load balance to reduce idling time. After derivatives in y are computed a transpose from y to z is performed and derivatives in z are then computed. The right-hand-side of Eqs. (2.2)-(2.3) at this point is complete. We can summarize these procedure symbolically as

$$\partial_x \rightarrow \mathrm{T(x,y)} \rightarrow \partial_y \rightarrow \mathrm{T(y,z)} \rightarrow \partial_z \tag{2.35}$$

where T(x,y) represents a transpose of pencils from x to y. While two transposes are needed in order to compute all the terms in the governing equations, unlike a 1D decomposition, only processors within a communicator are involved which typically consists of $\mathcal{O}(\sqrt{M})$ processors.

After the operations just described are completed, pencils are aligned with the z direction. The solution is then advanced one step in time. To continue with the time integration, the right-hand-side of Eqs. (2.2)-(2.3) need to be re-computed. This can be accomplished in two ways, (i) transpose data from z to x and follow the procedure outlined above, namely, Eq. (2.35), or (ii) compute terms in z, followed by transposes z to y and y to x. That is

$$\partial_z \rightarrow \mathrm{T(z,y)} \rightarrow \partial_y \rightarrow \mathrm{T(y,x)} \rightarrow \partial_x. \tag{2.36}$$

Although option (ii) adds more complexity to the code due to the alternating scheme

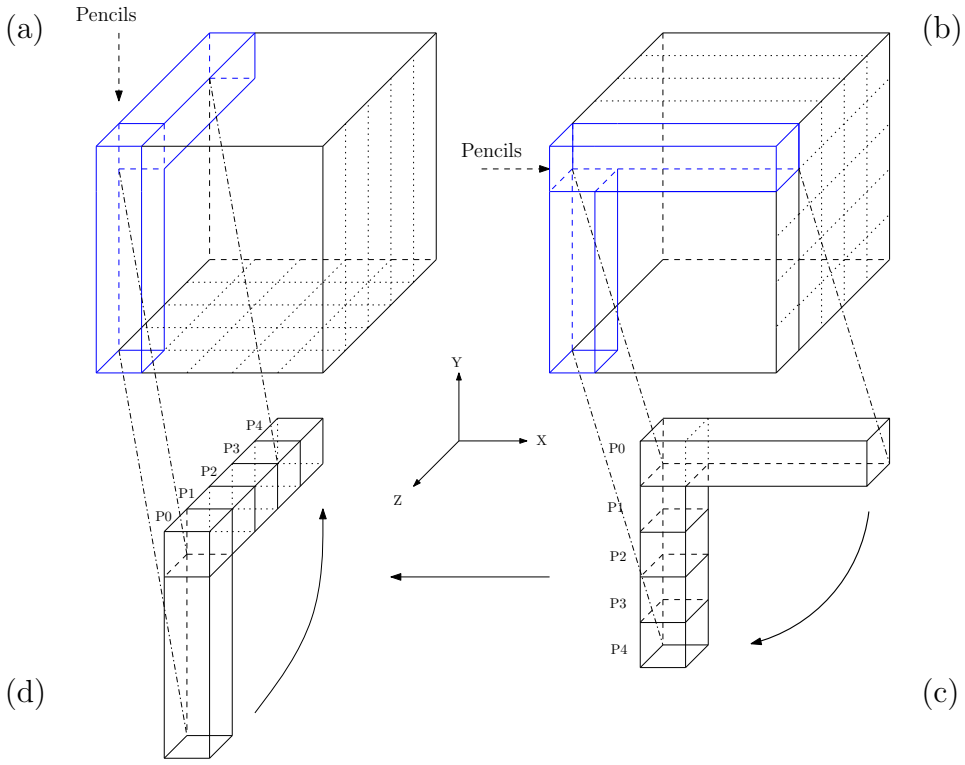

Figure II.2. Two-dimensional domain decomposition for $(iproc, jproc, kproc) = (1, 5, 5)$. Pencils in x (b) are transposed to y (c) and z (d) The final configuration is in z (a).

used for each Runge-Kutta sub-step, it clearly saves one transpose per two of these sub-steps and has, therefore, been chosen here.

In order to understand communication operations, one can estimate the number of messages in MPI_ALLTOALL for a given processor grid configuration. As already mentioned, to complete the transposes, two communicators that communicate along the rows (y) and columns (z) are created. We denote the processor grid configuration by $(iproc, jproc, kproc)$ where $iproc$, $jproc$ and $kproc$ are the number of MPI tasks used to divide data in the first, second and third directions, respectively. The total number of MPI tasks is $M = iproc$ x $jproc$ x $kproc$. Obviously, for a 2D domain

decomposition, one of the processor grid dimensions must be unity. For our current isotropic simulations with equal number of grid points (and boundary conditions) in all three directions, one can choose any direction without loss of generality. We have chosen $iproc = 1$.

Lets now consider, T(x,y), the transpose x to y. From figure II.3, we can see that for each pencil in x, there are $jproc^2$ messages to be sent. Since there are $kproc$ pencils in the z direction, the total number of messages is roughly $jproc^2$ x $kproc$. A similar argument for T(y,z) results in $kproc^2$ x $jproc$ messages. Since $jproc$ and $kproc$ can be chosen arbitrarily (as long as $jproc \times kproc = M$) we should expect communication performance to depend on the grid configuration. In principle three cases can be considered: $jproc > kproc$, $jproc < proc$ and $jproc = kproc$. For the first case, the time spent in x-to-y transposes is expected to be higher than y-to-z transposes. In the second case, we expect to see the opposite. Similar timings are expected for both transposes in the last case.

A simple performance model can be constructed using these approximations. Clearly the data volume being transferred per step is $2N^3$ regardless of the processor grid, where the factor 2 accounts for the two transposes in either Eqs. (2.35) or (2.36). The number of messages, n_m, however, does depend on $jproc$ and $kproc$ as we have seen. In particular, we can estimate $n_m = jproc^2 kproc + kproc^2 jproc$ which, since $kproc = M/jproc$, can also be written as $n_m = jproc \times M + M^2/jproc$. Typically, to minimize latency issues few large messages are preferred over many small messages. The number of messages will be minimum when $\partial n_m/\partial jproc = 0$ which is readily shown to be satisfied for $jproc = \sqrt{M} = kproc$. Therefore, the

number of messages per step is minimized for a square processor grid. The average size of each of these messages can also be shown to be $N^3/(Mjproc)$ and $N^3 jproc/M^2$ words which shows that for large $jproc$, messages are larger and smaller for the y-to-z and x-to-y transposes, respectively. Thus, for a highly skewed processor grid, latency overhead may dominate the time along one of the communicators.

Results from carefully designed benchmarks (Sec II.A.5) support the previous arguments: T(x,y) and T(y,z) transposes are more expensive for large $jproc$ and large $kproc$ respectively, and best performances are usually achieved when $jproc$ and $kproc$ are close (refer (Jagannathan & Donzis, 2012)). However, we also find that for $jproc = kproc$, the time for both transposes differ which seems to indicate that other factors play an important role in the performance of the code. Preliminary results (to be published elsewhere) may indicate that mapping of MPI tasks on the network topology, does have a different effect on the performance of each transpose.

II.A.4. Hybrid MPI-OpenMP

At large core counts collective communications are the main obstacle to sustained scalability. Depending on the architectural details, the time spent in communication could represent up to 50-75% of the total time as evidenced by detailed profiling of the code at close to 10^5 cores on Kraken at NICS. Therefore, there is a clear need to optimize communications if even larger processor counts are sought to achieve more realistic conditions or include more physical content in the simulations.

A sensible approach to extend the scalability of the code to more cores is a multi-level decomposition suitable for current and emerging platforms. In particular, while

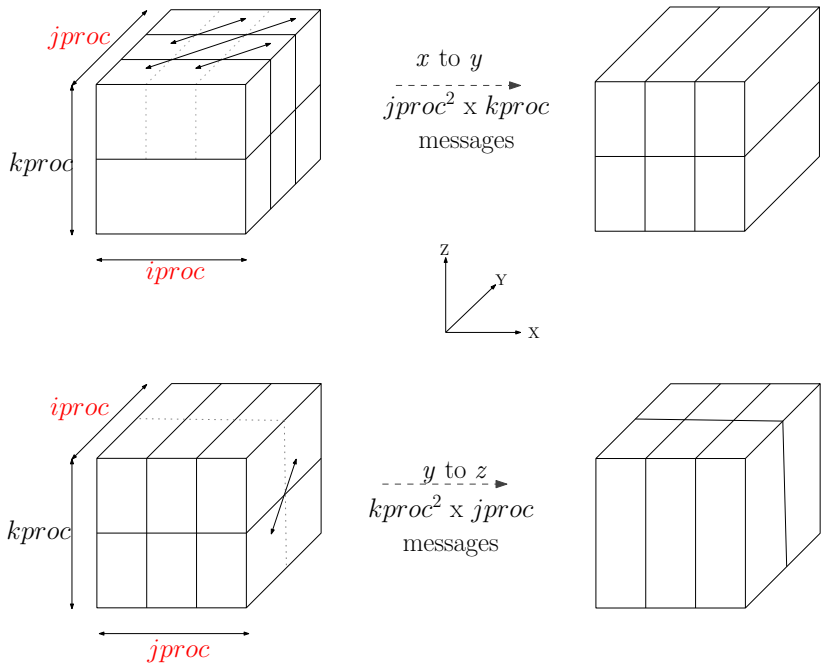

Figure II.3. Communication pattern for ($iproc, jproc, kproc$)=(1,3,2).

MPI can be used for inter-node communication, a shared-memory model (OpenMP) within a node (which usually comprises tens of cores) may provide performance advantages. Such an approach, while not new, has been shown to exhibit application dependent efficiencies (Yilmaz *et al.*, 2009; Mininni *et al.*, 2011). Limiting the number of MPI tasks involved in communications, can also reduce the global communication time since, for example, the number of messages is reduced and their size increased as discussed in Sec II.A.3. In fact, while the number of messages can still be estimated as $n_m = (jproc \times M + M^2/jproc)$, the number of MPI tasks M is now the total number of cores requested N_c divided by the number of threads per MPI task N_t, that is $M = N_c/N_t$.

In general, shared-memory paradigms are expected to perform best when good load balance is maintained and the amount of computation in each thread is high.

While the former is necessary to avoid idling because of the implicit synchronizations at the end of threaded loops or parallel regions, the latter reduces the number of creation, destruction and scheduling of threads. In order to ensure this, the code has been significantly reorganized from a pure MPI version. Particular efforts have been directed towards the very large number of loops to compute the right-hand-side of the governing equations which comprise the most intensive computational tasks. These were threaded at the outermost level, when possible, to maximize the amount of work per thread and minimize management tasks. Furthermore, threading the outermost level also maximizes the stride between data on different threads thus reducing the risk of false sharing.

The use of compact schemes requires solving linear systems of equations as explained in Sec II.A.1. For this LAPACK direct solvers are used for banded systems which require a factorization and a substitution step. While the former can be done as a initialization tasks at the beginning of the simulations, the latter has to be performed at each step for each derivative. Typically, the right-hand-side of the systems is composed of a number of lines of data aligned with the pencil. Thus, when data is in x, for example, there are $ny/jproc \times nz/kproc$ systems to be solved. The threading is introduced explicitly over the last dimension. The right-hand-sides in other directions are formed in such a way that solvers work on stride-1 data.

Despite possible overheads dues to the large number of thread creations and destructions, we show next that this approach is still beneficial at large processor counts. We also found, however, that more aggressive in-node optimization is possible which will increase the scaling of the OpenMP regions.

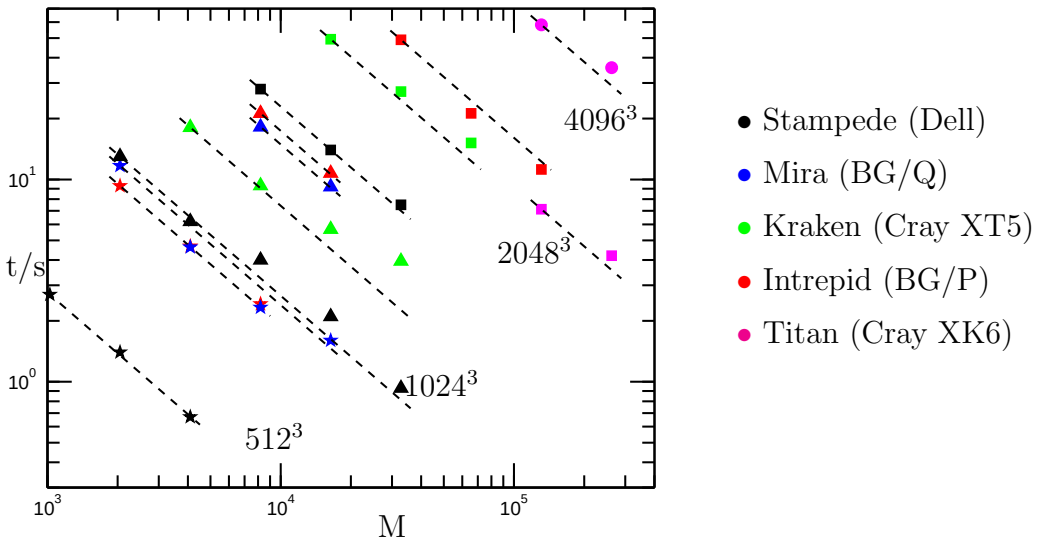

Figure II.4. Time per step for 512^3 (stars), 1024^3 (circles), 2048^3 (triangle), 4096^3 (square). Dashed lines are M^{-1} representing perfect strong scaling. Different colors represent different machines.

II.A.5. Benchmarks

A large number of benchmark tests were performed on different machines including Kraken at the National Institute for Computational Sciences (NICS), Stampede at Texas Advanced Computing Center, and Titan at Oak Ridge National Laboratory. In figure II.4 we show strong scaling data for three problem sizes of relevance to current and future simulations. The largest case was 4096^3 on 262,144 cores on Titan (Cray XK6). We can see almost perfect strong scaling (indicated by dashed lines) for both 2048^3 and 4096^3 resolutions even at the largest processor counts tested. Some departures are apparent for 32K cores for a 1024^3 grid which is not surprising given the fact that the number of grid points per core is small and a typical message size is about 40KB which indicates latency could play a role.

While we have observed very good scaling on several machines at $\mathcal{O}(10^5)$ cores, communication may well be the major obstacle towards even higher levels of paral-

lelism likely to be present on Exascale machines. As discussed in Sec II.A.3, limiting the number of MPI tasks involved in communications, can indeed reduce the global communication time.

$N.N_c.N_t$	*jproc* x *kproc*	t/s	T(x,y)+ T(y,x)	T(y,z)+ T(z,y)	Comm. total
512.1K.1	32 x 32	7.39	1.82	0.86	2.68
512.1K.2	16 x 32	7.59	1.42	1.00	2.42
512.1K.4	8 x 32	8.65	1.53	1.38	2.91
512.2K.1	32 x 64	3.78	1.15	0.67	1.82
512.2K.2	16 x 64	3.87	0.86	0.65	1.51
512.2K.4	8 x 64	4.40	0.84	0.82	1.66
512.4K.1	64 x 64	2.24	0.78	0.43	1.21
512.4K.2	**32 x 64**	**2.10**	**0.56**	**0.37**	**0.93**
512.4K.4	**32 x 32**	**2.35**	**0.62**	**0.36**	**0.98**
1024.8K.1	64 x 128	8.75	2.43	1.68	4.11
1024.8K.2	**64 x 64**	**8.72**	**2.25**	**1.19**	**3.44**
1024.8K.4	128 x 16	9.43	2.35	1.20	3.55
1024.16K.1	128 x 128	5.51	2.25	1.09	3.34
1024.16K.2	**128 x 64**	**4.76**	**1.74**	**0.66**	**2.40**
1024.16K.4	**128 x 32**	**4.90**	**1.53**	**0.68**	**2.21**
1024.32K.1	64 x 512	3.63	1.16	1.43	2.59
1024.32K.2	**128 x 128**	**3.06**	**1.26**	**0.62**	**1.88**
1024.32K.4	256 x 32	3.29	1.55	0.36	1.91

Table II.1. Benchmarks in hybrid configuration on Kraken (NICS). For all cases $iproc = 1$. Bold face cases perform better than the corresponding $N_t = 1$.

A representative collection of benchmarks on Kraken using the hybrid implementation is shown in Table II.1. Each case is denoted by $N.N_c.N_t$ where N^3 is the problem size, N_c is the number of cores requested and N_t is the number of threads. The number of MPI tasks for all cases is given by N_c/N_t. It is to be noted that,

irrespective of number of threads, performance depends on processor grid configuration. To evaluate the overall scaling of the code, we are interested in the time per step (t/s) for the best processor grid which is also indicated in the table. The last three columns represent the time spent in T(x,y) and T(y,x), T(y,z) and T(z,y) and the total time spent in communications, respectively.

If only one thread per MPI task is used, scalability results are similar to those for the pure MPI implementation. For a 512^3 grid, we see that the code presents 97% and 86% strong scaling when cores are doubled from 1024 and 2048, respectively. At 1024^3 strong scaling is 80% and 76% when core count is doubled from 8K and 16K respectively. We note, however, that the performance of the pure MPI implementation is slightly better than MPI/OpenMP with $N_t = 1$ possibly due to overheads in the OpenMP implementation.

With two threads per MPI task and the number of cores fixed (which implies the number of MPI tasks is reduced by a factor of two), we can see that except for the smallest problem presented, the overall time per step decreases. For example, 1024.32K.2 is about 20% faster than 1024.32K.1. This can be traced to a decrease in communication time both for x-y as well as y-z transposes. For the largest cases, namely, 1024.16K.4 and 1024.32K.2, we observe about 33% and 28% reduction in communication time. The difference between the gains in communication time and t/s is the result of some OpenMP parallel regions which scale less than perfectly with number of threads as well as a small number of unavoidable serial regions within an MPI task. Nevertheless, performance gains appear to become greater at scale.

Increasing the number of threads to four results in an increase in t/s for most

cases even though communication time is reduced further. This is associated with the overhead due to the handling of threads. Further optimization of OpenMP parallelization will likely result in further gains at scale.

In all of the above cases the vendor supplied (Cray for both Kraken and Jaguar) LAPACK routines dgbtrf and dgbtrs were threaded manually. The table also furnishes data for weak scaling: for instance, 512.1K.1 and 1024.8K.1 runs have the same load per processor and takes about the same time per step (7.39 and 8.75 secs) which is about 85% weak scaling. Similar observation can be drawn for 512.4K.4 and 1024.32K.4 with a weak scaling of 71%.

The data in Table II.1, also provides support for the analysis of the time spent in transposes in Sec II.A.3. Although OpenMP threads were not considered in the analysis, the data is qualitatively consistent with multiple threads. For illustration purposes we can consider the case 1024.32K. When the processor grid configuration is $(jproc, kproc) = (64,512)$ (i.e. $jproc < kproc$) transposes between y and z are more time consuming that those between x and y. The opposite is true when $kproc < jproc$ for the case $(jproc, kproc) = (256,32)$. However, for a square processor grid $(jproc, kproc) = (128,128)$, the times for both transposes are clearly different. While the reason for this is currently not completely understood, the mapping of MPI tasks onto nodes and processors seems to play a different role on different transposes. A more accurate understanding of the code performance can be obtained by detailed profiling of the code, which is discussed in the next section.

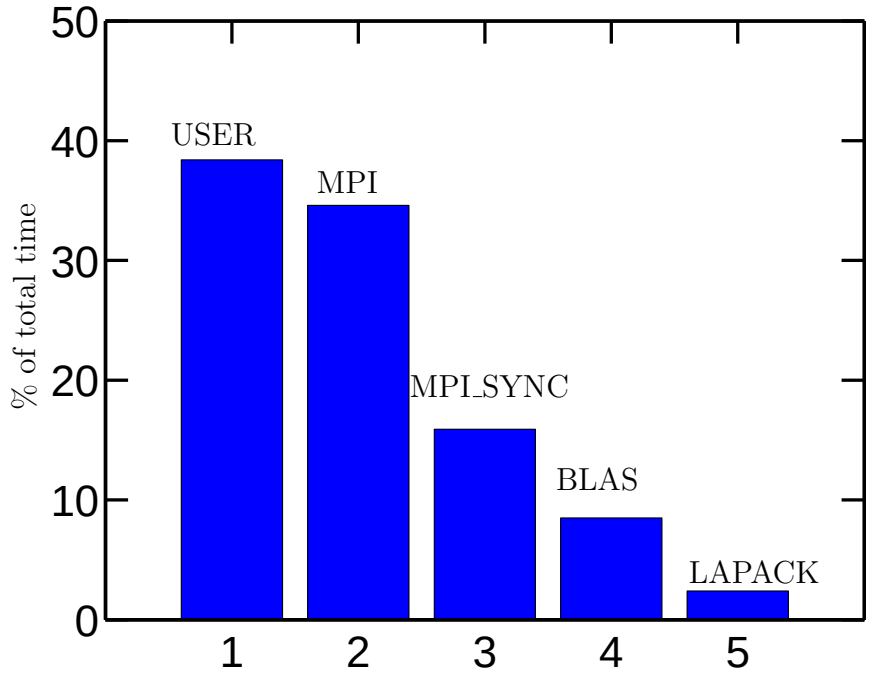

Figure II.5. Time spent in communication and computation for a 512^3 grid on 4096 processors.

II.B. Profiling and Performance Optimizations

In order to identify bottlenecks and possible performance issues, it is useful to study the time spent in different tasks in the code. This exercise, when refined with advanced profilers, can provide information about the memory footprint of the code, cache hits and misses, high watermark memory among others. A representative example of a coarse-grain profiling report is shown in figure II.5 for a 512^3 simulation on 4096 processors using CrayPat available on Cray machines. At this scale, about 35% of the overall time is spent in communication (MPI). However, more than 15% of the time is spent in synchronizing the processors (MPI_SYNC) to initiate the communication process, which increases as we go to a larger number of processors.

This could affect the overall scalability of the code, since even if the communication and computation time scale perfectly, the time spent in synchronizing the processors would not. As we show in Table II.2, the time spent in MPI decreases significantly as we increase the number of threads to two. This is due to the reduction in number of MPI tasks by a factor of two and also a corresponding increase in the MPI message sizes, which hides the effect of latency at large core counts. As a result of this reduction in MPI tasks, the time taken to synchronize processors also reduces significantly. Overall, the profiler shows about a 15% decrease in total time per step and 40% reduction in time spent in communication when the hybrid paradigm is used with two threads. However, as we increase to four threads, though the time spent in MPI and MPI_SYNC is reduced, the overall time per step is higher than that of the pure MPI case. This may happen when the amount of work per thread is very small, and the overhead to create, destroy and manage threads tend to overwhelm the time spent in actual computations.

The code has a smaller memory footprint at large core counts, requiring only about one-fourth of a MB per core per variable for a 512^3 problem size on 4096 processors. Considering that the physical quantities, and their gradients need to be stored (including the gradients of transport terms), a very reasonable approximation of memory usage would be assuming that about 50 words per grid point are used, which makes the overall memory footprint around 15 MB per core for this case. However, at any timestep, due to the usage of temporary arrays and the overhead due to MPI, the maximum memory requirement would be much more than this, which for this case is about 110 MB (from CrayPat). Considering the installed memory

capacity of current state-of-the-art supercomputers of about 2-3 GB of memory per core, this is still only a fraction of what is available.

Type	Pure MPI (s)	2 threads(s)	4 threads (s)
Total	16.69	15.31	17.75
User	6.41	7.07	8.74
MPI	5.77	3.61	3.34
MPI SYNC	2.67	2.27	2.14

Table II.2. Communication and Computation time for pure MPI and hybrid confiuration for a 512^3 grid on 4096 processors. The times mentioned here include the time spent for a total of five timesteps

Several performance optimizations specific to the architecture were attempted to reduce the overall time spent in computation, communication, and I/O. The specified environmental variables are in some cases native to the architecture and hence may not be applicable to other machines. Nevertheless, these are crucial in optimizing the code, and in most cases require only changing few environmental variables. A more detailed description of these are given in a manuscript by the NERSC supercomputing facility (**?**):

- MPICH_MAX_SHORT_MSG_SIZE: When MPI sends very short messages, the messages are directly sent to the receiver without any preposts. The threshold to switch between short and long message is given by this variable (default is 128 KB).

- MPICH_PTL_EAGER_LONG: When the message is classified as long, MPI posts a tag to the receiver that a message is slated to be sent to the processor.

As soon as a matching tag from the receiver is sent, MPI sends the long message. If this variable is set, then the long messages are sent via the "EAGER" protocol which ensures that matching receives are pre-posted to avoid a deadlock.

- MPICH_UNEX_BUFFER_SIZE: This controls the size of the buffer that holds all the unexpected events while communicating with MPI. Especially on Cray machines, this may have to be increased from the default value to enable large processor runs. The default is around 60 MB.

- MPICH_PTL_UNEX_EVENTS: Maximum number of unexpected events that can occur in a point-to-point message. The default value is 20480.

- MPI_COLL_OPT_ON: For collective communications, this flag, when set to true, enables some optimizations. This is especially useful while collective buffering is done during I/O for communications like in the present code that involve ALL_TO_ALLs.

Some of these environmental variables have been used at large core counts to effectively utilise the resources. For instance, (MPICH_UNEX_BUFFER_SIZE), has been doubled from its default value on Kraken (Cray XT5 architechture) to successfully run jobs on more than 16K cores. Similarly, to improve the performance while performing I/O, the collective optimization is activated (MPI_COLL_OPT_ON).

II.C. Passive Scalars

We have also added the capability of solving an arbitrary number of passive scalars, each of which is governed by the advection-diffusion equation,

$$\frac{\partial}{\partial t}\left(\rho\phi\right) + \frac{\partial}{\partial x_i}\left(\rho\phi u_i\right) = \frac{\partial}{\partial x_i}\left(D\frac{\partial \phi}{\partial x_i}\right), \tag{2.37}$$

where, ϕ is the scalar and D is the diffusivity. Using Reynolds decomposition, $\phi = \langle\phi\rangle + \phi'$, in Eq. (2.37), we get,

$$\frac{\partial}{\partial t}\left(\rho\phi'\right) + \frac{\partial}{\partial x_i}\left(\rho\phi' u_i\right) = -\boxed{\rho u_i \frac{\partial\langle\phi\rangle}{\partial x_i}} + \frac{\partial\langle\phi\rangle}{\partial x_i}\frac{\partial D}{\partial T}\frac{\partial T}{\partial x_i} + \frac{\partial}{\partial x_i}\left(D\frac{\partial \phi'}{\partial x_i}\right), \tag{2.38}$$

where the boxed term can be interpreted as the forcing term for sustaining scalar fluctuations. The mean scalar gradient, $\dfrac{\partial\langle\phi\rangle}{\partial x_i}$, drives the scalar and is typically prescribed as a constant in simulations (Overholt & Pope, 1996; Yeung *et al.*, 2002).

II.D. Simulation Database and Forcing in Compressible Turbulence

Direct Numerical Simulations (DNS) at different Reynolds and Mach number is required, for instance, to predict asymptotes at high Reynolds number and assess effects of compressibility. Hence, the code was used to generate a large database of homogeneous forced isotropic compressible turbulence which is used to investigate the Reynolds and Mach number scaling of solenoidal and dilatational components of several quantities, effects of dilatation on thermodynamic quantities, and the dynamics of energy transfer between internal and kinetic modes. In order to maintain a stationary state, energy is injected at the large scales through the momentum equation, a technique that has been used extensively in incompressible flows (Eswaran & Pope, 1988; Overholt & Pope, 1998; Rosales & Meneveau, 2005) and recently in

compressible flows (Petersen & Livescu, 2010).

Forcing in compressible turbulence, however, has a much wider and interdependent parameter space because the forcing parameters (mean temperature T_0, number of forced wavenumbers κ_f, amplitude of forcing, extent of solenoidal or dilatational forcing, and time scale of forcing) are used to control not only the Reynolds number but also the turbulent Mach number which in turns depends on e.g. the mean temperature. Each of these parameters may affect the flow variables simultaneously, for instance, if T_0 is decreased, we might expect M_t to increase ($M_t \propto u/\sqrt{T}$), but it could also change μ thus affecting the Reynolds number as well. This interplay of parameters compounded by constraints of achieving (i) well-resolved simulations ($k_{max}\eta \approx 1.5$, to be shown later), (ii) integral length scale being a fraction of the domain size, and (iii) the maximum R_λ for a given grid resolution, makes it a difficult problem to conduct a parametric variation of R_λ and M_t . This may account for why investigations of forced compressible turbulence have been scarce compared to incompressible turbulence. We have implemented a low wavenumber stochastic forcing based on Eswaran & Pope (1988), that forces the wavenumbers (κ) inside a spherical shell of radius κ_f ($\kappa \leq \kappa_f, \kappa_f = 3$). The injected energy cascades by non-linear interactions and is dissipated at the small scales. Since this increases the internal energy, one has to remove energy from the system to maintain a stationary state. We have implemented this in two different ways: by removing energy (i) such that the mean internal energy is constant (ii) homogeneously and with a value equal to the input energy. Consistent with previous studies (Wang *et al.*, 2010) results are virtually unaffected by the specific means in which energy is removed from the

system. The temperature dependence of viscosity and diffusivity (for scalars) follow a power-law dependence in accordance with the Sutherland's law and the fluid, assumed to be an ideal gas, has a Prandtl number, $Pr = 0.72$.

A systematic study has been done to identify how R_λ, M_t, and L vary with change in forcing parameters. Due to the nature of forcing and flow, it is not desirable to have anisotropy in the forcing and hence the maximum number of wavenumbers forced in each direction is kept equal such that force is applied in a spherical shell. However, the number of wavenumbers that is forced, is still a parameter. Previous investigations of forced incompressible turbulence (Eswaran & Pope, 1988) has found that the maximum number of forced wavenumbers markedly affects the integral length scale in the domain. It is also essential that this be not too high, especially for low-Reynolds number simulations, where the forcing would then extend to the small scales potentially affecting the universality concepts. Consistent with the literature, we retain a value of $\kappa_f = 3$. For a simpler analysis, we can consider only solenoidal forcing, and later extend a similar analysis for dilatational forcing. Hence, the major forcing parameters are the mean temperature, amplitude of forcing, extent of solenoidal/dilatational forcing and viscosity. The variation of R_λ, M_t, and L with each of these parameters is discussed below.

II.D.1. Variation with Amplitude of Forcing

A simple way of estimating how the amplitude of forcing varies with resolution is by investigating the kinetic energy equation,

$$\frac{d\langle \mathcal{K} \rangle}{dt} = \langle p'\theta' \rangle - \langle \epsilon \rangle + \langle f_i u_i \rangle \,, \tag{2.39}$$

where $\langle p'\theta' \rangle$ and $\langle \epsilon \rangle$ are the mean pressure-dilatation correlation and dissipation respectively (mentioned in detail in Ch III) and $\langle \mathcal{K} \rangle$ is the mean kinetic energy. The external energy added ($f_i u_i$), should be dimensionally consistent with that of the rate of kinetic energy. Accordingly, the rate at which external energy is added would become $f_0/\Delta t$, where Δt is the time step. Using the CFL condition, $C = u\Delta t/\Delta x$, we can recast the expression as $f_0/C\Delta x$, and since Δx varies inversely with the resolution, this leads to:

$$\text{Rate of addition of external energy} = f_0 N/C.$$

This relation is particularly useful, for instance, if one were to perform resolution studies at fixed Reynolds and Mach number. If the resolution is doubled, the amplitude of forcing needs to be reduced by one-half in order to achieve the same Reynolds and Mach number. Evidently, if the CFL is reduced, the amplitude of forcing should also be correspondingly reduced.

While this analysis gives an estimate of how the parameters need to be varied when the resolution is changed, there is very little information about how R_λ, M_t and $\Delta x/\eta$ change with f_0. Here, $\Delta x/\eta$ is the resolution criteria that shows how well the small scales are resolved, the smaller the number, the more resolved the small scales are. The optimal value of $\Delta x/\eta$, which depends on the quantity of interest, is discussed towards the end of this section. This is shown in figure II.6. As the amplitude of forcing is increased, the quantities R_λ, M_t and $\Delta x/\eta$ increase (but at slightly different rates). While M_t approximately varies as $f_0^{0.9}$, R_λ and $\Delta x/\eta$ have a slightly shallower slope of 0.5 ($M_t \sim f_0^{0.9}, R_\lambda \sim f_0^{0.5}, \Delta x/\eta \sim f_0^{0.5}$).

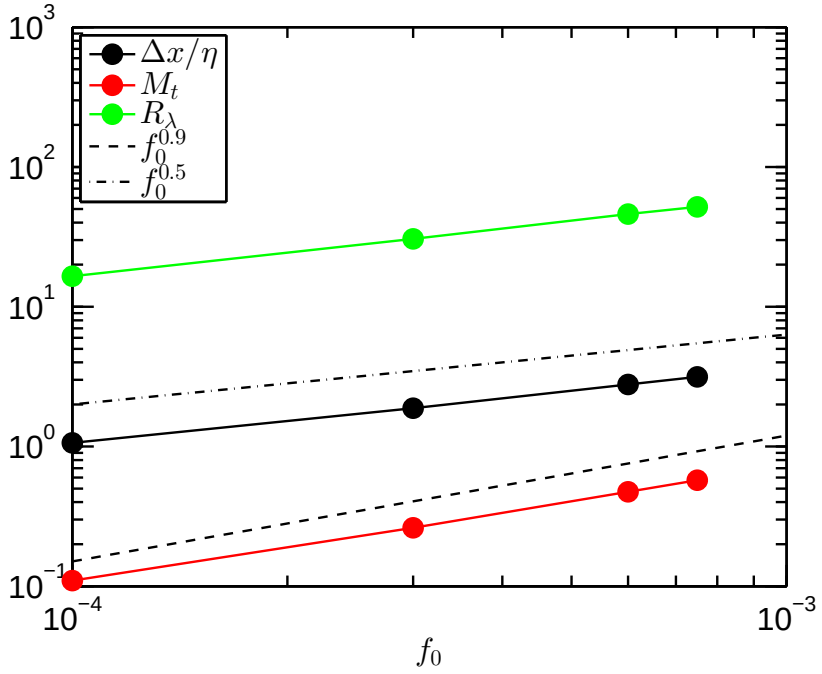

Figure II.6. Variation of R_λ, M_t, and $\Delta x/\eta$ with f_0

II.D.2. Variation with Mean Temperature

The effect of mean temperature, T_0, can be accounted for from the definition of Mach number and speed of sound, $M_t \sim u/\langle c \rangle \sim u/\sqrt{\gamma R T_0}$, which gives the variation $M_t \sim 1/\sqrt{T_0}$, if one doesn't consider the variation of u with T_0. Hence, to achieve a high M_t, the mean temperature should be decreased. The Reynolds number dependence on T_0 is not straightforward and hence a parametric study is conducted as shown in figure II.7. As predicted, M_t increases as T_0 is decreased. For the range of values investigated, the variation is described as $M_t \sim T_0^{-1/4}$, $R_\lambda \sim T_0^{1/4}$ and $\Delta x/\eta \sim T_0^{1/4}$.

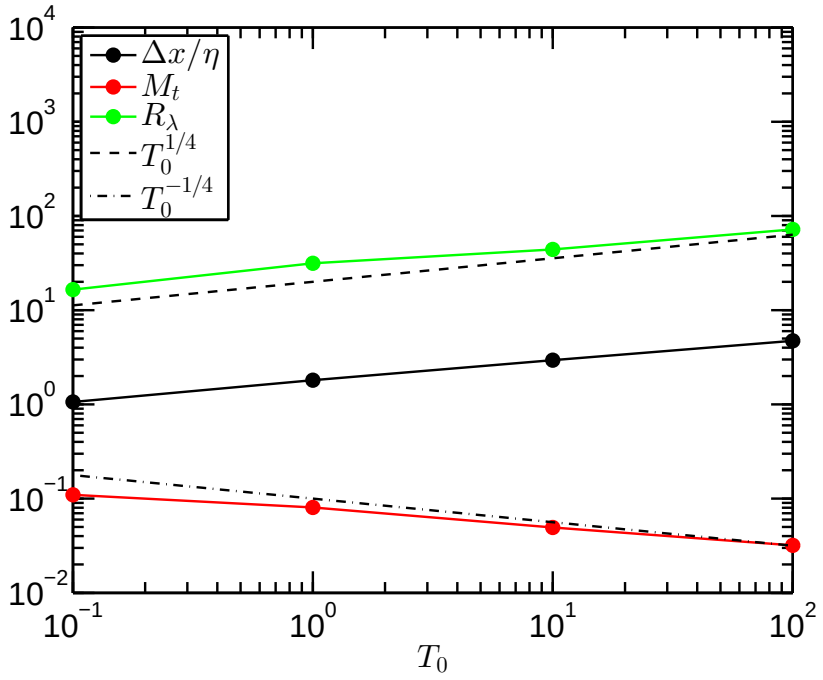

Figure II.7. Variation of R_λ, M_t, and $\Delta x/\eta$ with T_0

II.D.3. Variation with Viscosity

The dependence of Reynolds number on viscosity is however straightforward from the definition of Reynolds number, $R_\lambda \sim 1/\mu$. Its effect of M_t can also be estimated from the Sutherland's Law which relates the temperature and viscosity ($\mu \sim T^{0.5}$). Hence if μ is increased, the temperature increases and from the previous relation ($M_t \sim 1/\sqrt{T_0}$), we know that this would qualitatively lead to a decrease in M_t. This is consistent with what is shown in figure II.8, where M_t decreases with μ, but by a very small amount. The effect on R_λ and $\Delta x/\eta$ is however very prominent and decreases as predicted with a slope of -1. The reference value of viscosity for a prescribed resolution is similar to that of homogeneous isotropic incompressible turbulence that is described in Donzis & Yeung (2010) and is given in Table II.3.

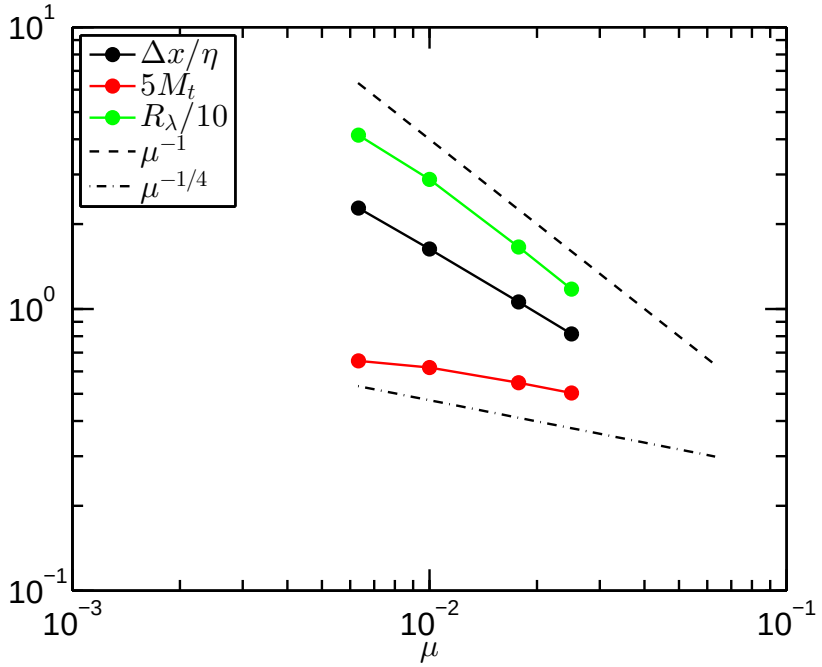

Figure II.8. Variation of R_λ, M_t, and $\Delta x/\eta$ with μ

II.D.4. Small-scale Resolution

While it is possible to force independently both the solenoidal and dilatational mode of velocity, in this work, our main focus will be in simulations where only the solenoidal mode is forced. However, we have also performed simulations with dilatational mode forced and is presented in Ch V. The DNS database, summarized in Table II.4 for solenoidal forcing, consists of grid resolutions from 64^3 to 2048^3 with Taylor Reynolds number ranging from 38 to 450 at different Mach numbers, $M_t = 0.1, 0.2, 0.3, 0.4$ and 0.6. To ensure accurate small-scale resolution, we have done convergence studies. We focus on high-order moments of velocity gradients which are much more sensitive to resolution than other quantities such as correlations and spectra (Donzis *et al.*, 2008*b*), mean dissipation rate ($\langle\epsilon\rangle = 2\langle\sigma_{ij}S_{ij}\rangle$) and mean

N	μ
32	0.04480
64	0.01777
128	0.00705
256	0.002800
512	0.001100
1024	0.000437
2048	0.000173
4096	0.000068734

Table II.3. Values of viscosity (μ) used in the stationary state simulations of incompressible turbulence of Donzis & Yeung (2010).

enstrophy ($\langle\Omega\rangle = \langle\omega_{ij}\omega_{ij}\rangle$). They are presented in figure II.9 for moments up to order 4. At low M_t (≈ 0.1), moments of both the quantities are converged at $\eta/dx \approx 0.5$. A more stringent resolution requirement is seen for higher order moments of mean dissipation rate as M_t increases. Though this may suggest the need for a better resolved grid at high M_t (≈ 0.6), moments up to order two are converged. This would imply that statistics of velocity up to order four are converged at $\eta/dx \approx 0.5$. For results shown in this paper, which are of order 4 or less, a resolution of $\eta/dx \approx 0.5$ is thus sufficient.

II.E. Summary

A highly scalable simulation code for turbulent flows which solves the fully compressible Navier-Stokes equations is presented. The code, which supports one,

N^3	R_λ	M_t	L/η	λ/η	T_E	$\frac{\langle \mathcal{K}^d \rangle}{\langle \mathcal{K}^s \rangle}$ $\times 10^3$	$\frac{\langle \epsilon^d \rangle}{\langle \epsilon^s \rangle}$ $\times 10^3$
64^3	39	0.1	20.6	12.2	0.3	0.01	0.17
64^3	32	0.2	18.1	11.0	0.3	0.20	0.12
64^3	33	0.3	18.4	11.3	0.9	2.38	0.83
64^3	38	0.4	19.5	12.1	0.7	10.98	4.35
64^3	34	0.6	18.1	11.3	1.2	38.82	39.93
128^3	63	0.1	36.5	15.6	0.4	0.03	0.13
128^3	54	0.2	29.0	14.5	0.2	0.43	0.13
128^3	60	0.3	32.8	15.2	0.8	13.19	2.91
128^3	65	0.4	34.9	15.8	0.8	24.50	7.25
128^3	58	0.6	28.7	14.8	1.0	44.03	42.46
256^3	108	0.1	72.4	20.5	0.3	0.02	0.21
256^3	101	0.2	61.8	19.7	0.2	0.72	0.18
256^3	106	0.3	63.8	20.3	0.6	9.69	1.89
256^3	107	0.4	59.3	20.3	0.6	13.83	4.01
256^3	96	0.6	58.3	19.1	1.1	42.30	43.05
512^3	173	0.1	142.2	25.9	0.3	0.01	0.21
512^3	173	0.2	140.0	25.9	0.2	0.11	0.17
512^3	163	0.3	128.0	25.2	0.7	9.98	1.88
512^3	167	0.4	105.5	25.5	0.6	15.74	4.35
512^3	158	0.6	115.2	24.5	1.0	37.88	39.80
1024^3	268	0.3	248.0	32.2	0.6	2.06	0.31
1024^3	241	0.4	168.7	30.4	1.2	36.54	20.23
2048^3	430	0.3	511.9	40.7	0.7	0.92	0.19

Table II.4. Parameters used in the simulation for different R_λ and M_t.

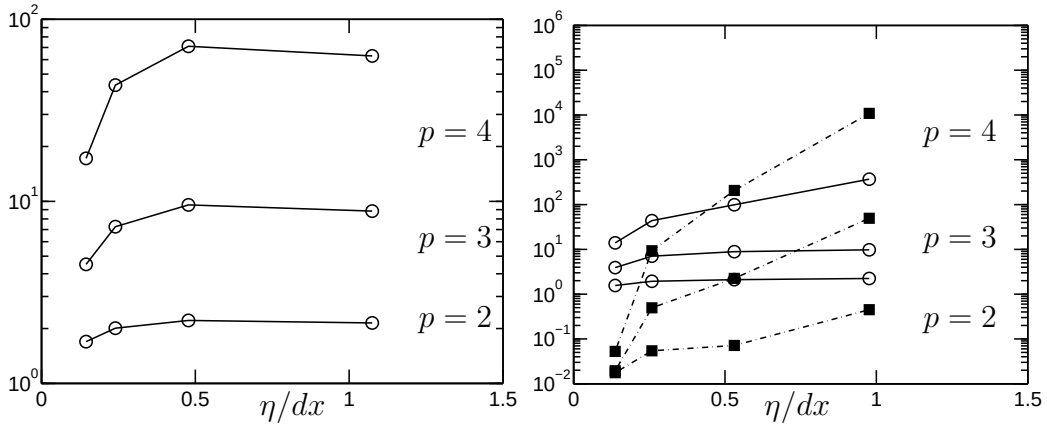

Figure II.9. Normalized moments of dissipation (square) and enstrophy (circle) at $R_\lambda \approx 60$ for (a) $M_t \approx 0.1$ (b) $M_t \approx 0.6$.

two and three dimensional domain decompositions is shown to scale well on up to 262,144 cores. Introducing multiple levels of parallelism based on distributed message passing and shared-memory paradigms results in a reduction of up to 40% of communication time at large core counts. The code has been used to generate a large database of homogeneous isotropic turbulence in a stationary state created by forcing the largest scales in the flow. To attain a statistically stationary state a new scheme is developed which involves large-scale stochastic forcing (solenoidal or dilatational) and a procedure to keep mean internal energy constant. The resulting flows show characteristics consistent with results in the literature. The attainable Reynolds and turbulent Mach numbers for given computational resources depend on the number of grid points and the degree to which the smallest scales are resolved that are given by Kolmogorov scales. A systematic comparison of simulations at different resolutions suggests that the resolution needed depends on the particular statistic being considered.

CHAPTER III

REYNOLDS AND MACH NUMBER SCALING IN STATIONARY COMPRESSIBLE TURBULENCE

Common features that distinguish compressible flows from its incompressible counterpart are the presence of fluctuations of thermodynamic variables and the non-zero dilatation values of the fluid medium. Hence, in order to better understand the nature of compressible flows, it is critical to comprehend the behavior of thermodynamic variables, the changes that the dilatation of fluid bring about, and how they are inter-related. Furthermore, understanding the action of compressibility can advance science in different fields of engineering, for instance, in designing supersonic vehicles, mixing in high speed flows and thermal non-equilibrium among others. The general disposition towards accounting for compressibility effects has been to decompose the velocity field into an incompressible (solenoidal) and compressible (dilatational) component based on Helmholtz decomposition. A similar form of decomposition has been extended to, though it's definition is somewhat arbitrary, pressure. Other attempts have also been made to isolate compressiblity effects. For instance, Kovasznay (1953) linearized the Navier-Stokes equation to obtain the solution as superposition of vorticity, entropy and acoustic modes under the assumption that effect of compressibility is very small. Chu & Kovásznay (1958) extended the analysis as a second-order approximation to account for stronger compressibility effects. Dastgeer & Zank (2005) employed a similar approach. This assumption, however, is very restrictive for a large class of engineering flows that operate at high

speeds where different modes interact and thus superposition may not be always appropriate.

The thermodynamic variables are related by an equation of state for an ideal gas and are accompanied by acoustic phenomenon, such as, propagation of sound waves. Depending on the level of compressibility, which is commonly quantified in a large manner by the turbulent Mach number ($M_t = \langle u_i u_i \rangle / \langle c \rangle$, summation implied and $\langle X \rangle$ is the mean of quantity X), different approximations can be made that lead to distinct flow regimes. For instance, at low M_t, the acoustic time scale is much smaller than the convective and viscous time scale leading to a simplified set of equations (Erlebacher *et al.*, 1990; Sarkar *et al.*, 1991). This results in a flow regime known as low-Mach number quasi-isentropic regime, where the flow evolves only on acoustic time scale and characterized by small dilatational fluctuations (Sagaut & Cambon, 2008). At higher levels of compressibility, the dilatational fluctuations may be substantial and cannot be neglected. This flow regime, in which the dilatational fluctuations are significant and the Mach number is still less than one, is classified as non-linear subsonic regime and is the principal regime of investigation in this paper. One of the simplest frameworks to investigate the role of compressiblity in this regime is that of homogeneous isotropic turbulence where wall effects and anisotropy are not present. Recent advances in computing have enabled large scale simulations of homogeneous compressible turbulence at grid resolutions as high as 1024^3 (Petersen & Livescu, 2010; Wang *et al.*, 2012). Using some of the powerful supercomputers available today, we report results from simulations of homogeneous forced compressible isotropic turbulence with grid resolutions ranging from 64^3 to

2048^3 for Taylor Reynolds number ranging from 38 to 450 and Mach numbers 0.1 to 0.6. The 2048^3 simulation with a Taylor Reynolds number of 450 is, to the authors knowledge, the largest simulation of forced compressible isotropic turbulence available in the literature.

For homogeneous compressible flows, the Helmholtz decomposition allows the velocity field to be written as, $\mathbf{u} = \mathbf{u^s} + \mathbf{u^d}$, where $\mathbf{u^s}$ is the solenoidal ($\nabla \cdot \mathbf{u^s} = 0$) and $\mathbf{u^d}$ is the dilatational ($\nabla \times \mathbf{u^d} = 0$) component of velocity. Compressibility effects have typically been attributed to the small yet non-negligible contribution from the dilatation field (Lee *et al.*, 1991) which is zero in incompressible flows. Thus, in order to understand the effects of compressibility, it is important to delineate the similarities, differences and relative contributions of the solenoidal and dilatational mode and their scaling with Taylor Reynolds number ($R_\lambda = \langle\rho\rangle\, u\lambda/\langle\mu\rangle$, where λ is the Taylor length scale and $\langle\mu\rangle$ is the mean dynamic viscosity) and turbulent Mach number. A fundamental aspect of turbulence is the presence of a wide range of length scales, which typically ranges from the integral scales to the so-called Kolmogorov scale (Kolmogorov, 1941). For scales smaller than that, dissipative effects are assumed to be dominant. Although Kolmogorov scale has been proposed for incompressible flows, it has been used extensively to understand and characterize compressible flows. However, its scaling has not been assessed systematically in these flows, where concerns may appear especially at high M_t. We address this in Sec III.B.

Because in compressible flows energy can be either in the form of kinetic or internal energy, there has also been interest in energy interactions in reacting flows

(Livescu *et al.*, 2002), shock turbulence interactions (Lee *et al.*, 1993) and compressible flows in general (Bataille *et al.*, 1997; Miura & Kida, 1995). To examine the energy transfer process, it is useful to take the dot-product of the Navier-Stokes equation with $\mathbf{u}$, and then average, which after rearrangements results in equation for mean turbulent kinetic energy ($\langle \mathcal{K} \rangle$). Along with the mean internal energy ($\langle \rho e \rangle$) the equations read,

$$\frac{d\langle \mathcal{K} \rangle}{dt} = \langle p'\theta' \rangle - \langle \epsilon \rangle + \langle f_i u_i \rangle \,, \tag{3.1}$$

$$\frac{d\langle \rho e \rangle}{dt} = - \langle p'\theta' \rangle + \langle \epsilon \rangle - \Lambda. \tag{3.2}$$

The terms $\langle p'\theta' \rangle$ and $\langle \epsilon \rangle$ are the mean pressure-dilatation correlation and dissipation rate, which as is clearly seen, represent exchange terms between the equations and $\langle f_i u_i \rangle$ is the mean energy injected into the system and Λ is the amount of energy removed from the system. Eqns Eq. (3.1) and Eq. (3.2) form the basis of our present work. We study the scaling of each of the terms in the above equations with R_λ and M_t and also the nature of energy exchange between the internal and kinetic energies.

The mean energy dissipation rate in incompressible turbulence becomes independent of the fluid viscosity at very high Reynolds numbers ($D \equiv \langle \epsilon \rangle u^3/L$). This phenomenon, often known as dissipative anomaly, is central to the dynamics of energy cascade and has been supported by experiments and simulations over the past several decades (Sreenivasan, 1984, 1998; Kaneda *et al.*, 2003; Donzis *et al.*, 2005). However, a systematic assessment of whether D asymptotes to a constant at high Reynolds and Mach number, and if it does, the asymptotic magnitude has not been thoroughly investigated. The mean dissipation rate, just like velocity and pressure, can be decomposed into a solenoidal ($\langle \epsilon^s \rangle$) and dilatational ($\langle \epsilon^d \rangle$) component and

a similar asymptotic constant can be established for each. Based on an asymptotic analysis of Navier-Stokes equation, Erlebacher *et al.* (1990) and Sarkar *et al.* (1991) derived a model for the dilatational dissipation rate in the low-Mach number regime ($\langle\epsilon^d\rangle \propto M_t^2\langle\epsilon^s\rangle$). This model assumed the ratio of solenoidal and dilatational Taylor scales to be a constant, which as we will show in Sec III.C.1, follows a power law dependence on M_t instead. Available literature suggest $\langle\epsilon^d\rangle/\langle\epsilon^s\rangle$ scale as M_t^2 based on an EDQNM analysis at low Mach numbers (Bertoglio *et al.*, 2001), M_t^4 based on statistical analysis (Ristorcelli, 1997; Fauchet & Bertoglio, 1998) and also M_t^5 at high turbulent Mach numbers using EDQNM approximation (Sagaut & Cambon, 2008). Other relations have also been proposed in the literature (Zeman, 1990; Blaisdell & Zeman, 1992). Some of these results have been validated only at low Mach and Reynolds number using simulations of decaying compressible turbulence that could possibly have the signature of initial conditions (Ristorcelli, 1997; Vreman *et al.*, 1996) or with an EDQNM approximation (Bertoglio *et al.*, 2001). One way of removing the dependence on initial condition, is to force the simulation by adding energy to the large scales so that a statistically stationary state is achieved. This is the case in the present study.

Sarkar *et al.* (1991) proposed an equipartition of energy between the dilatational components of kinetic energy and potential energy (due to pressure). This is also referred to as the weak equilibrium hypothesis (Sagaut & Cambon, 2008) since global quantities like root mean square (rms) of pressure fluctuation, mean density and M_t are used to represent the energies. A more rigorous adaptation, known as the strong equilibrium hypothesis, requires them to be in equilibrium for each wavenum-

ber (Sagaut & Cambon, 2008). Equipartition, in weak equilibrium sense, has been supported by decaying simulations (Shivamoggi, 1997; Lee & Girimaji, 2013) even in shear flows (Bertsch *et al.*, 2012) for low M_t. However, only a few studies have investigated this result for stationary compressible turbulence (Kida & Orszag, 1990; Miura & Kida, 1995), which were also at low Reynolds number ($R_\lambda \leq 40$). While originally proposed to be valid for low M_t and high R_λ, our simulations suggest that equipartition of energy seems to be a good approximation at high M_t in the case of stationary turbulence.

The other exchange term in eqns Eq. (3.1) and Eq. (3.2), is the correlation between pressure and dilatation, often known as pressure-dilatation correlation ($p'\theta'$). While the mean dissipation rate represents a uni-directional energy transfer from kinetic to internal energy modes, the pressure-dilatation correlation facilitates a bi-directional energy exchange mechanism between them. It is also clear, from eqns Eq. (3.1) and Eq. (3.2), that any influence of compressibility in pressure fluctuation, could bring about changes in pressure-dilatation correlation and consequently the way energy is exchanged, affecting the global dynamics of flow. We thus, investigate the effects of compressiblity on the behavior of pressure. We examine some existing scaling relations for the solenoidal and dilatation components of pressure and identify departures, if any. For example, the probability distribution function (p.d.f.) of pressure, is known to be negatively skewed in incompressible flows (Holzer & Siggia, 1993; Pumir, 1994; Vedula & Yeung, 1999) and at low M_t. We findd that at high M_t, the p.d.f. becomes positively skewed following a log-normal distribution for positive fluctuations (Donzis & Jagannathan, 2013*a*). As we show here, this seems to result

from large contributions of dilatational pressure. While in incompressible turbulence the role of pressure is restricted to redistribution of energy across components of momentum by upholding continuity, in compressible turbulence pressure couples both thermodynamics and hydrodynamics. Due to this coupling, it is natural to expect any change in hydrodynamics, like dilatation of the fluid, to affect the thermodynamic fluctuations. Therefore, we investigate statistics conditioned on dilatation and also detail the behavior of dilatation at low and high Mach numbers. An interesting finding is that, regions with high pressure and strong expansions tend to co-exist at high M_t.

It is well-established in incompressible turbulence that regions of low-pressure and high vorticity are highly correlated (Nomura & Post, 1998; Cao *et al.*, 1999). However, such a correlation, though not generally expected to hold at high Mach numbers, has not been explored in compressible flows. In this context, it is useful to consider enstrophy (Ω), which is the square of vorticity, and is a measure of rotation of fluid element. Due to the curl-free nature of the dilatational velocity field, enstrophy, in compressible flows, can be attributed to purely solenoidal motion. We show that this correlation between regions of low/high pressure and enstrophy decreases with increasing Mach number, and thus the skewness of pressure at high M_t cannot be attributed to solenoidal motions. Instead, they can in principle, be affected by dilatational modes.

The behavior, and the effects, of strong dilatation of fluid has been studied before (Samtaney *et al.*, 2001; Pirozzoli & Grasso, 2004), where it is argued that the appearances of these intense events tend to increase with M_t. We have studied the

energy-interactions for both small and strong dilatation of the fluid and at different levels of compressibility. While it is generally believed that a strong compression of fluid increases the energy dissipation (Lee *et al.*, 1991, 2009) triggering transfers from kinetic to internal mode, it is still not well established if a similar picture holds true for equally strong expansions. Moreover, the net transfer between kinetic and internal energies can change due to the contribution from pressure-dilatation. As we demonstrate in Sec IV.A, net energy exchanges in regions of high dilatation could be dominated by pressure-dilatation more than dissipation regardless of M_t.

The rest of this chapter is organized as follows. Effect of compressiblity on classical scaling relations is analyzed in Sec III.B followed by a discussion on equipartition of energy in compressible flows in Sec III.C.

III.A. Solenoidal and Dilatational Components

As mentioned before, the velocity field is decomposed into solenoidal and dilatational field, for which we will use superscripts s and d respectively, which is unique for a homogeneous flow. Since $\mathbf{u}^s$ and $\mathbf{u}^d$ are orthogonal to each other on the average $\left(\left\langle \mathbf{u^s} \cdot \mathbf{u^d} \right\rangle = 0\right)$, respective kinetic energies also follow $\mathcal{K} = \mathcal{K}^s + \mathcal{K}^d$ (Kida & Orszag, 1990; Lele, 1994). The solenoidal and dilatational components of mean kinetic energy is given by $\langle \mathcal{K}^s \rangle = \langle \rho u_i^s u_i^s / 2 \rangle$ and $\langle \mathcal{K}^d \rangle = \left\langle \rho u_i^d u_i^d / 2 \right\rangle$, with summation implied on i. Using Reynolds decomposition, we decompose a random variable X into mean $\langle X \rangle$ and fluctuations X', such that $x = \langle X \rangle + X'$. For quantities with zero mean, the primes are dropped for simplification. Two examples are the velocity field u and forcing term f.

Sarkar *et al.* (1991) proposed a way to decompose $\langle\epsilon\rangle$ into a solenoidal ($\langle\epsilon^s\rangle$) and dilatational ($\langle\epsilon^d\rangle$) component by recasting them in terms of fluctuating vorticity (ω_i) and dilatation (θ).

$$\langle\epsilon^s\rangle = \langle\mu\rangle\langle\omega_i\omega_i\rangle\,, \quad \langle\epsilon^d\rangle = \frac{4}{3}\langle\mu\rangle\left\langle\theta^2\right\rangle. \tag{3.3}$$

We assume here, in accordance with the DNS data, that the fluctuations in μ are small which permits us to write $\langle\mu X\rangle \approx \langle\mu\rangle\langle X\rangle$ for a quantity X. Similarly, the fluctuating pressure can be decomposed into a solenoidal pressure satisfying the incompressible pressure Poisson equation,

$$\nabla^2 p'_s = \langle\rho\rangle \frac{\partial u_i^s}{\partial x_j}\frac{\partial u_j^s}{\partial x_i}, \tag{3.4}$$

and the dilatational pressure, $p'_d = p' - p'_s$, defined as the difference between the total pressure and solenoidal pressure fluctuations.

III.B. Classical Scaling

A number of results strictly valid for incompressible flows, have been used, nonetheless in compressible flows. This includes basic tenets of classical phenomenology of Kolmogorov (1941). While at low Mach numbers one expect similarities between compressible flows and strictly incompressible flows, the departures (if any) from classical scaling have not been studied systematically. These include scaling of Kolmogorov length and velocity scales and dissipative anomaly. One of the intrinsic interest in these scalings is due to the behavior of flow itself. The maximum local Mach number observed in our simulations could be as high as five times the mean. This intense fluctuation is extremely localized in space, but occurs consistently in

time. We investigate the possibility of such extreme events affecting the statistics of quantities mentioned in the following subsections.

III.B.1. Dissipative Anomaly

A particular topic in incompressible turbulence that has accrued several years of research is the phenomenon of dissipative anomaly, the concept that at sufficiently high Reynolds number and away from walls, the mean energy dissipation rate becomes independent of the fluid viscosity (Sreenivasan, 1984, 1998; Kaneda *et al.*, 2003; Donzis *et al.*, 2005). This has also been tested for compressible flows. The limited results that are available in literature suggest that at low M_t the influence of compressibility on the asymptotic value of the constant, $D = \langle\epsilon\rangle L/u^3$, is minimal (Pearson *et al.*, 2004; Schmidt *et al.*, 2006). Pearson *et al.* (2004) argued that there is a delay in time between energy injection and dissipation which should be taken into account while calculating the constant D. Using ensemble averaged quantities, like in figure III.1, eliminates this ambiguity.

Figure III.1 shows D versus R_λ from our database. Qualitatively, the figure is very similar to that in incompressible flows (Sreenivasan, 1984; Donzis *et al.*, 2005). In particular, there is a decrease of D with R_λ for low value of R_λ, but approaches an asymptotic value at high R_λ. The asymptotic state appears to be reached at $R_\lambda \approx 100$ consistent with previous incompressible results (Sreenivasan, 1984; Donzis *et al.*, 2005). The scatter around $R_\lambda \approx 160$ may indicate the onset of compressibility effects. For $M_t \approx 0.3$, the asymptotic value of D is around 0.43 while for other M_t, the R_λ is too low to achieve an asymptotic state.

The phenomenological underpinning of dissipative anomaly is that large scale set the rate at which energy is transferred through increasingly smaller scales until viscosity is effective and dissipates this energy. A straightforward extension to compressible flows would indicate that D approach a constant too at high R_λ, which is approximately, what is seen in figure III.1. However, in compressible flows we have $\langle\epsilon\rangle = \langle\epsilon^d\rangle + \langle\epsilon^s\rangle$. Thus, if dissipative anomaly holds, both components should approach an asymptotic state at high R_λ. Since D_s is just the difference between D and D_d, we show D_d in figure III.1(b) as a function of M_t. Though the overall contribution from D_d is less than 3% for the cases considered, there is a dramatic increase in its relative contribution for $M_t > 0.3$. So, it may be possible that in the high M_t limit, D may be a function of M_t depending on the behavior of D_d, but for the range of M_t considered in this paper, D is only weakly affected by compressiblity. Simulations at increasingly higher Reynolds and Mach numbers are needed to reach an unambiguous conclusion about the dependence of the asymptotic constant on M_t.

III.B.2. Velocity and Length Scales

Kolmogorov (Kolmogorov, 1941) defined the characteristic scales for the small scales as,

$$\eta \equiv \left(\nu^3/\langle\epsilon\rangle\right)^{1/4}, \quad u_\eta \equiv \left(\nu\langle\epsilon\rangle\right)^{1/4}, \quad \tau_\eta \equiv \left(\nu/\langle\epsilon\rangle\right)^{1/2}, \tag{3.5}$$

where η, u_η, τ_η are the Kolmogorov length, velocity and time scales. Here, ν is taken to be a constant since both ρ and μ do not vary in incompressible flows. These relations lead to a simple scaling law if the normalized mean energy dissipation rate

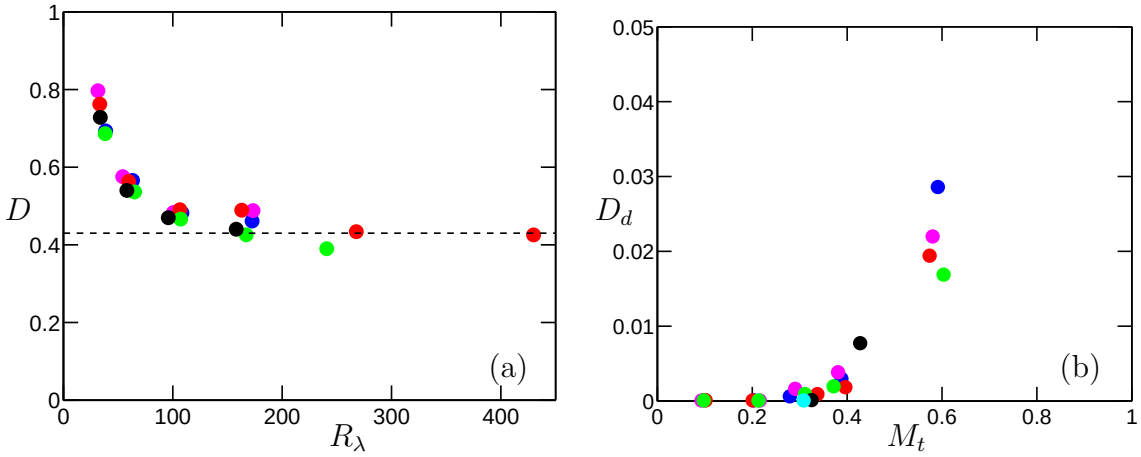

Figure III.1. (a) Normalized mean energy dissipation ratio (D) and its (b) dilatational component (D_d) at different R_λ and M_t. The dashed line in (a) represents $D = 0.43$. Different colors for M_t according to the following: $M_t \approx 0.1$ (blue), 0.2 (magenta), 0.3 (red), 0.4 (green), 0.6 (black). Different colors for R_λ according to the following: $R_\lambda \approx 38$ (blue), 60 (magenta), 100 (red), 160 (green), 275 (black), 450 (cyan).

asymptotes to a constant ($\langle\epsilon\rangle L/u^3 = D$, as shown in Sec III.B.1). Substituting $\langle\epsilon\rangle \propto u^3/L$ in Eq. (3.5) and after some algebra, we get

$$\frac{\lambda}{\eta} \sim R_\lambda^{1/2}, \quad \frac{L}{\eta} \sim R_\lambda^{3/2}, \quad \frac{u}{u_\eta} \sim R_\lambda^{1/2}, \tag{3.6}$$

where L is the integral length scale.

The extension of Eq. (3.5) to compressible flows, though typically straightforward, is not unique. Since ν varies in space and time, one could define $\eta \equiv \langle\nu\rangle^3/\langle\epsilon\rangle$ or $\langle\nu^3/\epsilon\rangle$. Since there is no appreciable difference between the two forms, we compute the characteristic scales by using the mean viscosity ($\langle\nu\rangle$) instead of ν in Eq. (3.5).

We plot the non-dimensionalized Taylor micro-scales and integral length scale in figure III.2(a). While the scaling of Taylor micro-scales conform very well to that of the proposed scaling ($\lambda/\eta \sim R_\lambda^{1/2}$) without any M_t dependence, the scaling of integral length scales deviate slightly from $R_\lambda^{3/2}$ at low Reynolds number. This is not

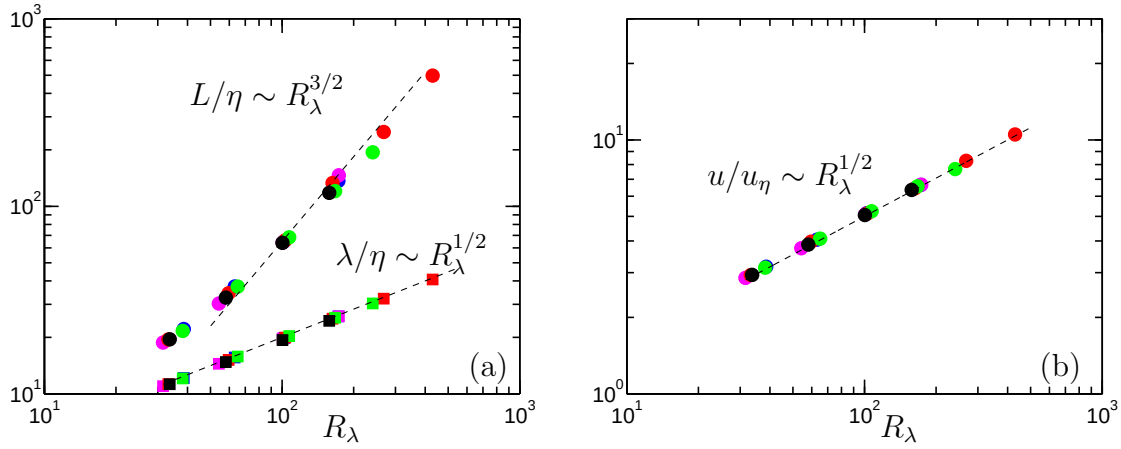

Figure III.2. Scaling of (a) Taylor micro scale (λ) and integral length scale (L) and (b) Kolmogorov velocity scale (u_η). Dashed lines indicate classical Kolmogorov scaling for incompressible turbulence: $\lambda/\eta \sim R_\lambda^{1/2}$, $L/\eta \sim R_\lambda^{3/2}$, $u/u_\eta \sim R_\lambda^{1/2}$. Colors according to figure III.1.

surprising given that Kolmogorov scaling has been proposed only when the Reynolds number is high enough. However, even at high Reynolds numbers, a close inspection of the data seems to suggest a slight correction with the data presenting a shallower power law. Results at higher Reynolds numbers are needed to unambiguously determine this departure. As a result, one could infer that, for turbulent Mach numbers upto 0.6, the effect of compressibility on low order quantities tend to be weak.

III.B.3. Scaling of Spectra

A fundamental property in turbulent flows is the so-called energy cascade in which energy introduced at the largest scales, typically characterized by the integral length scale L, is transferred to smaller scales due to non-linear mechanisms. Based on this concept, Kolmogorov (Kolmogorov, 1941) proposed a self-similar theory which bestows certain universality for turbulent scales much smaller than L. In

particular, the theory predicts (Monin & Yaglom, 1975) a three-dimensional energy spectrum of the form

$$E(k) = C\langle\epsilon\rangle^{2/3}k^{-5/3}f(k\eta), \tag{3.7}$$

where, $\langle\epsilon\rangle$ is the mean energy dissipation rate, C is the Kolmogorov constant, k is the wavenumber, $\eta = (\nu^3/\langle\epsilon\rangle)^{1/4}$ is the Kolmogorov length scale and $f(k\eta)$ is a universal function independent of the large scale features of the flow such as boundary conditions or forcing when Reynolds number is high enough and scales are much smaller than L. Furthermore, if scales are also larger than η, viscous effects are negligible and it is expected that $f(k\eta) \to 1$. This range of scales ($1/L \ll k \ll 1/\eta$) is known as the inertial range.

While Eq. (3.7) is strictly valid for incompressible flows and has been in fact shown to represent numerical and experimental data satisfactorily under this condition (Sreenivasan & Antonia, 1997; Ishihara *et al.*, 2009), the theory has been widely used also for compressible flows (Lele, 1994) though compressibility corrections should in principle be introduced (Sagaut & Cambon, 2008). Therefore, it is important to study, in a systematic manner, how or if classical theories apply to compressible flows with particular emphasis in distinguishing Reynolds and Mach numbers effects. Furthermore, to understand flows of practical interest it is critically important to achieve the highest possible Reynolds number which will, therefore, posses a wide inertial range.

In figure III.3 we show the collection of energy spectra that is normalized as $E(k)k^{5/3}/\langle\epsilon\rangle^{2/3}$. A number of features can be seen that support Kolmogorov universality theory. First, data appears to collapse at high wavenumbers regardless of

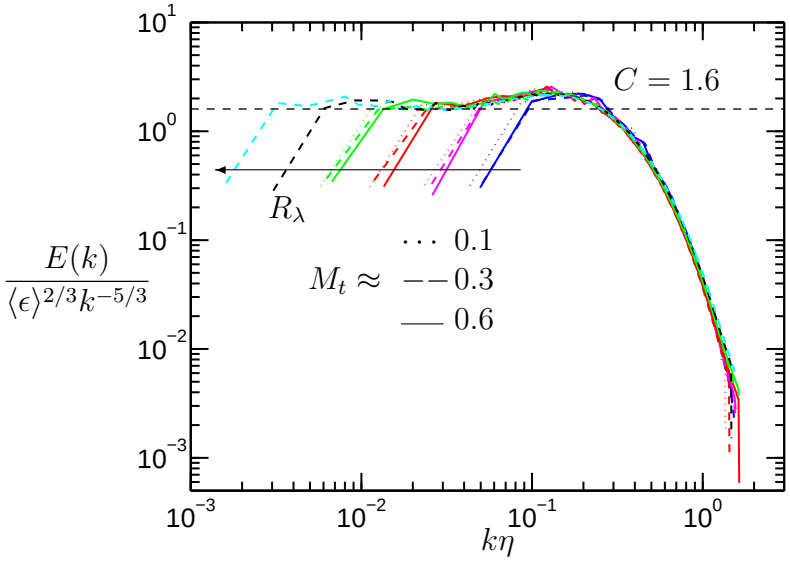

Figure III.3. Normalized energy spectra at different R_λ and M_t. Colors correspond to $R_\lambda \approx 38$ (blue), 60 (magenta), 100 (red), 160 (green), 275 (black), 450 (cyan), and differene line styles correspond to different M_t. The dashed line represents the constant $C = 1.6$ from incompressible turbulence.

Reynolds and Mach numbers even at M_t as high as 0.6. Second, spectra are seen to exhibit a plateau in the inertial range which widens with R_λ. The height of the plateau is the Kolmogorov constant C. Also shown in the picture is the value $C = 1.6$ which is the accepted value for incompressible flows (Sreenivasan, 1995; Donzis & Sreenivasan, 2010*a*). Finally, a spectral bump is also seen at $k\eta \approx 0.13$ similar to the one in incompressible flows. Taken together, the data suggests that Mach number effects are very weak, and the scaling with Reynolds number is similar to incompressible flows.

For reference we also present in figure III.4 the dilatational spectrum $E_d(k)$ obtained from the irrotational or dilatational component of a Helmholtz decomposition of the velocity field (e.g. Kida & Orszag (1990)) for $M_t \approx 0.1, 0.3$ and 0.6 and

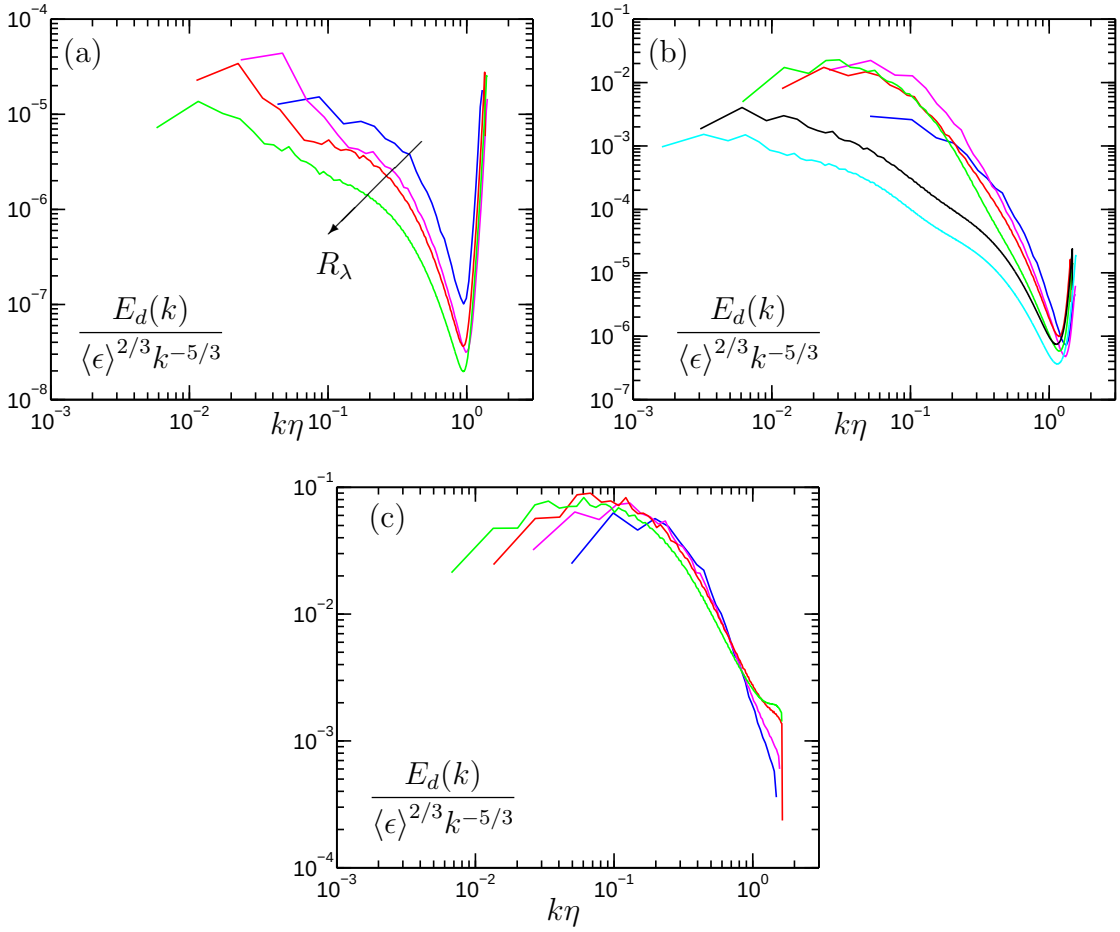

Figure III.4. Normalized dilatational energy spectra at $M_t \approx$ (a) 0.1 (b) 0.3 (c) 0.6. Different colors for R_λ according to figure III.1.

different Reynolds numbers. While inertial-range scaling is difficult to observe, we note that the energy in the dilatational component is orders of magnitude smaller than the total energy, though its contribution grows with Mt. We note that at very high wavenumbers ($k\eta > 1$) some well-known residual errors (e.g. Watanabe & Gotoh (2007); Ishihara *et al.* (2009) etc.) are seen, though their contribution to total energy is negligible (the effect is greatly amplified in the figure due to the multiplication by $k^{5/3}$ that results from the normalization) and have virtually no effect on the quantities of interest here. However, at high M_t, since the contribution from the dilatational component is higher, the residual errors tend to decrease. It is also interesting to note that at high M_t, there is a good collapse of the curves at different R_λ and an incipient inertial range is also seen at high R_λ (see green curve in figure III.4(c)). Based on an EDQNM analysis, Bataille *et al.* (1997) have demonstrated that at high Mach numbers it may be possible for the energy in the dilatational mode to have a similar cascade process as that of incompressible turbulence. While high M_t simulations are necessary to unambiguously confirm this hypothesis, our data seems to suggest a good collapse of the normalized dilatational energy spectra at the range of R_λ and M_t investigated.

III.C. Equipartition of Energy in Homogeneous Compressible Turbulence

The phenomenon of equipartition is often associated with non-dissipative linear waves where the sum total of potential and kinetic energy is constant. But in turbulence, where non-linear as well as dissipative effects are observed at any Reynolds

number, such distribution of energy, in principle, is not expected. However, Kraichnan (1955) observed that for an adiabatically compressible fluid at low Mach numbers, the vorticity and acoustic modes are coupled by the non-linear terms and drive the system to an equilibrium state. Similarly, Sarkar *et al.* (1991) decomposed the Navier-Stokes equation into a compressible and incompressible part and suggested equipartition at low M_t for the compressibile component. The non-dimensional parameter, $F = \gamma^2 M_t^2 \chi \langle p \rangle^2 / \langle p_d'^2 \rangle$, which is the ratio of dilatational kinetic energy and potential energy due to the dilatational pressure, should then tend to unity.

The equipartition of energy, though theoretically derived for the low-Mach number subsonic regime, has found support at M_t as high as 0.5 in DNS of decaying turbulence (Sarkar *et al.*, 1991). In these flows, the initial transient are thought to be dominated by acoustics. At later times, viscous and convective effects are expected to play a larger role. On the other-hand, in stationary flows with external forcing, it is difficult to associate a physical time at which each of these processes dominate independently. It is likely that both the acoustic and turbulent phenomena occur concurrently at different timescales based on the Mach number. At higher levels of compressibility, the coupling between the acoustic and vorticity mode is also enhanced and could possibly distort the equipartition. The existing literature lends support equipartition only in the low Reynolds-low Mach number limit. Due to its widespread application and usefulness in turbulence modeling, we now investigate the validity of equipartition at high M_t limit.

Figure III.5 shows the variation of ensemble-averaged equipartition function, F, with M_t. For $M_t < 0.3$, the data is scattered around $F \approx 1$, with significant

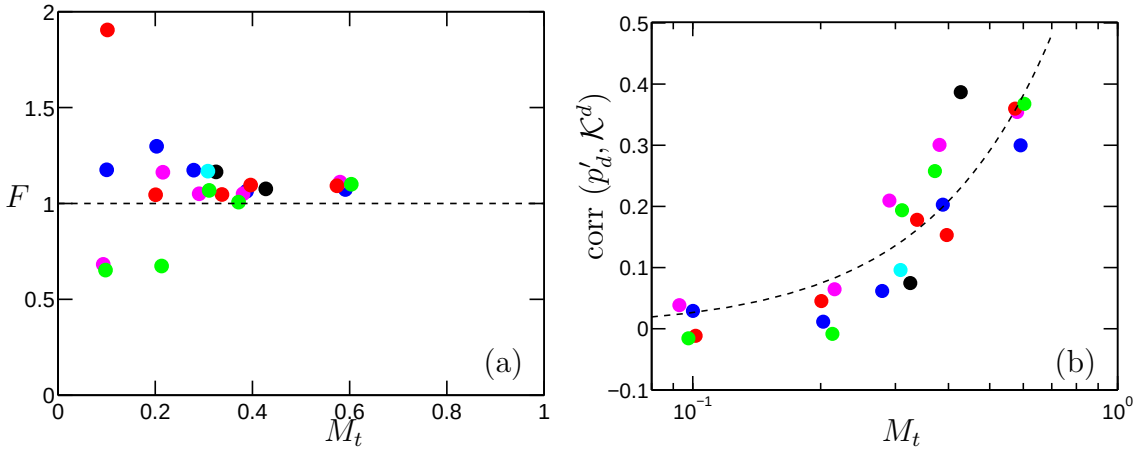

Figure III.5. (a) Variation of equipartition function F with χ, and (b) correlation between p'_d and $\mathcal{K}^d$ with M_t^d.

Reynolds number dependence, while beyond $M_t \approx 0.3$, F is much closer to one with weak R_λ influence. The scatter in data may be directly related to the scaling of normalized dilatational pressure ($p'_d/\langle p \rangle \approx M_t^2$). As detailed in Sec IV.A, while at high M_t the data conforms to this scaling, at low M_t there is considerable deviation. This seems to indicate the existence of a difference between decaying and forced turbulence. In decaying flows, during the acoustic transient period, dilatational pressure plays a crucial role in bringing the system towards equipartition. As we will show in Sec IV.A, the role of dilatational pressure in forced flows isn't dominant until a threshold M_t is reached. And hence F deviates from unity at low M_t. It is thus conceivable that the system may tend to equipartition at much lower M_t, if the dilatational mode is forced.

Miura & Kida (1995) observed F to be slightly in excess of unity ($F \approx 1.15$) in their simulations of forced compressible turbulence at $R_\lambda \approx 35$ and $M_t \approx 0.14$. In our simulations as well, F is slightly greater than one. A small difference may not

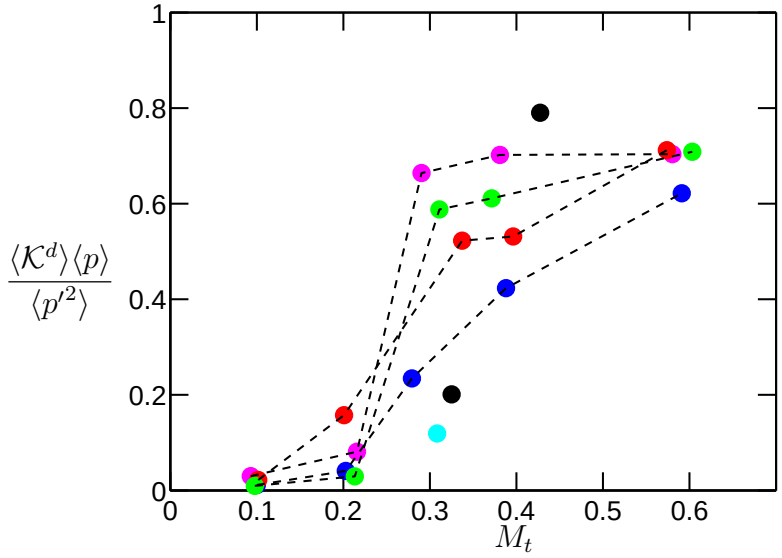

Figure III.6. Equipartition function, F, recast terms of total pressure and density. Colors for R_λ correspond to figure III.3.

be unexpected if one recalls the assumptions behind the theoretical results. First, the theory assumes isentropic fluctuations which is not strictly correct (Donzis & Jagannathan, 2013*a*). Second, the decomposition of the velocity field does not correspond to a strict Helmholtz decomposition like the one used here. While still not strictly equal to unity, the DNS data supports an approximate balance between the dilatational components of kinetic energy and potential energy.

Equipartition applied as an instantaneous equilibrium, would imply that regions of low dilatational motions would be correlated with high dilatational pressure and vice-versa. Thus, a more direct measure of local equilibrium is the correlation coefficient between $1/2\mathbf{u}_i^d\mathbf{u}_i^d$ and p'_d which is shown in figure III.5(b). At high M_t, the dilatational components of pressure and kinetic energy become well correlated, as shown in figure III.5(b) which may well be a precursor for equipartition. Since the correlation between p'_d and $1/2\mathbf{u}_i^d\mathbf{u}_i^d$ increases with M_t, we can expect equipartition

to be increasingly valid as M_t increases. This is consistent with observations in figure III.5(a). However, this will imply a stronger form of equipartition where locally and instantaneously dilatational pressure equilibrates with dilatational kinetic energy.

Since in real flows, the only realizable fluctuations of pressure is the total pressure and not its solenoidal or dilatational component, we recast the non-dimensional parameter, F, in terms of total pressure. Quantitatively, it has been argued (Sarkar *et al.*, 1991; Sagaut & Cambon, 2008) that this would lead to $F = \langle \mathcal{K}^d \rangle \gamma \langle p \rangle / \langle p'^2 \rangle$. In figure III.6, we show the ratio which would approach unity if equipartition is achieved. While lower and higher M_t cases are necessary to reach a more conclusive interpretation, the data may suggest an asymptotic state at very low M_t when the ratio is close to zero with a weak influence of Reynolds number effect. We note that this is in contrast with decaying sheared flows starting from purely solenoidal fields (Bertsch *et al.*, 2012). This may again be due to the differing role of dilatational pressure in both forced and decaying flows. Around $M_t \approx 0.3$, there is a sharp increase in F followed by a plateau at $M_t \approx 0.6$ with the value of F around 0.70. This qualitative transition in flow statistics at $M_t \approx 0.3$ was also observed in figure III.1(b). Interestingly, though F tends to one at high M_t when expressed in terms of total pressure, it doesn't approach unity.

III.C.1. Dilatational Dissipation

One of the results that could change due to equipartition is the scaling of dilatational dissipation. The model, $\langle \epsilon^d \rangle \sim M_t^2 \langle \epsilon^s \rangle$, by Sarkar *et al.* (1991) was based

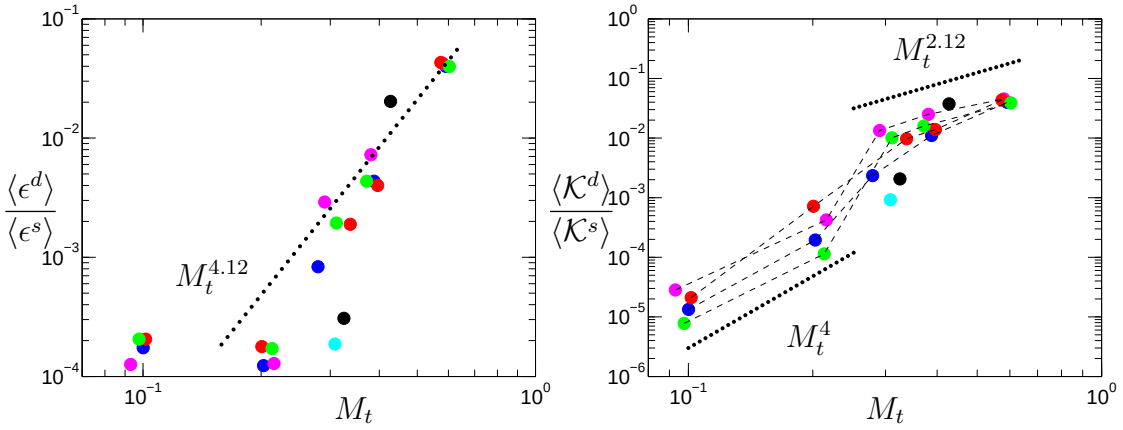

Figure III.7. Ratio of dilatational to solenoidal (a) dissipation (b) turbulent kinetic energy. Symbols for different Reynolds numbers as in figure III.2. The dotted lines corresponds to (a) $M_t^{4.12}$ (b) $M_t^{4.0}$ (bottom), $M_t^{2.12}$ (top) respectively.

on a low-Mach number approximation and assumed that *a*) equipartition of energy is valid, *b*) the ratio of solenoidal and dilatational Taylor scales is independent of Reynolds and Mach number and *c*) the normalized dilatational pressure scales as $p'_d/\langle p \rangle \approx M_t^2$. We will address each of these assumptions in this and subsequent sections. Based on the definition of Taylor scales and assuming that density is weakly correlated with velocity field, it can be shown that the ratio of solenoidal to dilatational Taylor scales varies as, $\lambda^s/\lambda^d \sim \sqrt{(\langle \mathcal{K}^s \rangle/\langle \mathcal{K}^d \rangle)\,(\langle \epsilon^d \rangle/\langle \epsilon^s \rangle)}$. It can be clearly seen that this would become independent of Reynolds and Mach number only if $\langle \mathcal{K}^d \rangle/\langle \mathcal{K}^s \rangle$ and $\langle \epsilon^d \rangle/\langle \epsilon^s \rangle$ scale similarly. As will be shown here, they scale differently and hence a correction factor has to be incorporated while modeling λ^s/λ^d. A suitable scaling at low and high Mach number is also suggested.

We first look at the ratio of solenoidal to dilatational dissipation in figure III.7. Though lower Mach number cases are necessary to conclude, it appears that there might be two different scaling ranges depending on M_t with the transition occurring

around $M_t \approx 0.2$. While the contribution of dilatational dissipation is negligibly small at low M_t, it increases sharply beyond $M_t \geq 0.2$, following a steep power law, $\langle \epsilon^d \rangle / \langle \epsilon^s \rangle \sim M_t^{4.12}$ when all the Reynolds numbers are included and $M_t^{4.47}$ for $R_\lambda \leq 200$. This steep power law indicates that the contribution of dilatational terms become more significant as M_t increases. And since dilatational dissipation is more intermittent than the solenoidal (Donzis & Jagannathan, 2013*b*), the overall dissipation would be more intermittent at higher Mach numbers. The Reynolds number dependence, for the range of Mach numbers considered, is weak.

The scaling of ratio of dilatational and solenoidal kinetic energy, $\langle \mathcal{K}^d \rangle / \langle \mathcal{K}^s \rangle$, have been proposed in the literature. Sarkar *et al.* (1991) suggested a M_t^2 dependence at low M_t based on asymptotic analysis, Fauchet & Bertoglio (1998) proposed M_t^4 and $M_t^2 \mathrm{Re_L}$ scaling using an EDQNM approximation with different decorrelation functions. The ratio is plotted in figure III.7(b) and has a strong Reynolds number dependence at low M_t. Similar to the scaling of ratio of dissipation, there could be different scaling relations at low and high M_t. A much steeper scaling, M_t^4, is observed in the low M_t regime and a $M_t^{2.2}$ dependence is observed for $M_t \geq 0.3$ with diminishing Reynolds number dependence. Since the ratios $\langle \epsilon^d \rangle / \langle \epsilon^s \rangle$ and $\langle \mathcal{K}^d \rangle / \langle \mathcal{K}^s \rangle$ both have an indiscernible dependence on R_λ for $M_t \geq 0.3$, the ratio of solenoidal and dilatational Taylor scales should be independent of R_λ at high M_t and have a R_λ dependence only in the low M_t regime. This would now suggest qualitatively that at high M_t, $\lambda^s / \lambda^d \sim \sqrt{M_t^{4.12} / M_t^{2.12}}$ and hence $\lambda^s / \lambda^d \sim M_t^{1.0}$. Figure III.8 shows the plot of ratio of solenoidal to dilatational Taylor scales from our database. Again, two qualitatively different regimes can be identified with a transition around

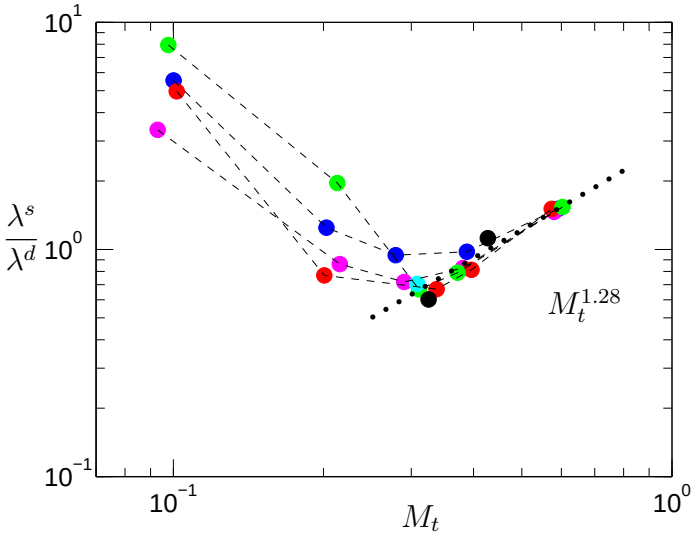

Figure III.8. Ratio of solenoidal and dilatational Taylor scales. Symbols for different Reynolds numbers as in figure III.1. The dotted lines represent $M_t^{1.28}$ line.

$M_t \approx 0.3$. For low Mach-numbers we see a strong Reynolds number dependence and a functional form different from $M_t^{1.0}$. As mentioned before, this is due to Reynolds number dependence seen at low M_t in the scaling of $\langle \mathcal{K}^d \rangle / \langle \mathcal{K}^s \rangle$. This dependence weakens beyond $M_t \approx 0.3$ eventually becoming almost independent of R_λ at $M_t \approx 0.6$. Best-fit curves for $M_t \geq 0.3$ shows a $M_t^{1.28}$ scaling which is in accord with the earlier prediction. Consistent with other statistics, this also undergoes a change around $M_t \approx 0.3$.

III.D. Summary

The classical scaling of length and velocity scales originally proposed for incompressible turbulence (Kolmogorov, 1941) is seen to have a very weak dependence on M_t. The normalized energy spectra for different R_λ and M_t appear to support the

Kolmogorov universality theory (Kolmogorov, 1941) for incompressible turbulence. However, the dilatational energy spectra showed significant dependence on R_λ at low M_t. For high M_t, a good collapse of curves at different R_λ is seen as well as an incipient inertial range. While a more rigorous analysis is required, it is possible that the dilatational mode has a cascade process similar to that of incompressible turbulence supporting a similar EDQNM based prediction (Bataille *et al.*, 1997). The equipartition of energy, which shows some scatter at low M_t, is seen to be valid at high M_t. As M_t is increased, the tendency to establish local equipartition between the dilatational kinetic energies and potential energies also increases due to the correlation between the dilatational modes of velocity and pressure. When the equipartition function, F, is expressed in terms of total pressure, we observe two different asymptotic regimes. While F is close to zero for low M_t, it tends to asymptote to about 0.70 at high M_t, indicating that the equipartition of energy tends to occur between the dilatational modes of velocity and pressure. The transition between these two regimes occurs around $M_t \approx 0.3$. We further investigated the scaling of dilatational dissipation and kinetic energies normalized by their respective solenoidal components, which also show two regimes with a transition around $M_t \approx 0.3$. The scaling at high M_t for the former and latter is shown to be of the form $\epsilon^d/\epsilon^s \approx M_t^{4.62}$ and $\mathcal{K}^d/\mathcal{K}^s \approx M_t^{2.2}$. Furthermore, the ratio of dilatational and solenoidal Taylor scales were shown to possess a similar transition at $M_t \approx 0.3$, beyond which it conforms to the scaling of the form $M_t^{1.21}$. Overall, the results seem to indicate that the effects of compressibility are particularly significant in some statistics beyond $M_t \approx 0.3$.

CHAPTER IV

ROLE OF THERMODYNAMIC AND DILATATIONAL FLUCTUATIONS IN STATIONARY COMPRESSIBLE TURBULENCE

IV.A. Pressure Statistics

In this chapter, we study the scaling of pressure and its components at a range of R_λ and M_t. Furthermore, we attempt to ascertain the plausible causes for the appearances of high-pressure regions at high M_t. This is done by systematically studying the statistics of pressure conditioned on enstrophy and dilatation, which represent the effects of solenoidal and dilatational motions respectively. While in incompressible turbulence, low pressure and high enstrophy regions are strongly correlated, we find that this correlation is weakened as M_t increases, indicating that regions of high-pressure may occur due to dilatational effects. As we show in this chapter, high-pressure regions and expansions tend to occur together.

IV.A.1. Solenoidal and Dilatational Pressure Scaling

Considering that equipartition, which is based on a balance between the potential energy due to dilatational pressure and dilatational kinetic energy, appears to depend on R_λ and M_t, it seems important to understand not only total pressure, but in particular the solenoidal and dilatational components as mentioned in Sec III.A. Though different decompositions are possible (Sarkar (1992) provides an alternative

definition), Eq. (3.4) is widely used in turbulence modeling. Since by definition the solenoidal pressure satisfies the incompressible pressure Poisson equation, we can expect the relation, $\sqrt{\langle {p'_s}^2 \rangle} \sim \langle \rho \rangle \langle u_i^s u_i^s \rangle$, to be uninfluenced by Reynolds and Mach number effects (Erlebacher *et al.* (1990)). Figure IV.1(a) shows that indeed $\sqrt{\langle {p'_s}^2 \rangle}$ scales as $\langle \rho \rangle \langle u_i^s u_i^s \rangle$ with a weak Mach number dependence. It has been observed in incompressible turbulence that this ratio is 0.91 (Donzis *et al.*, 2012). Though high R_λ cases are necessary to find the asymptotic constant, at $M_t \approx 0.1$ ($R_\lambda \approx 160$) we find the ratio around 0.88, close to the incompressible case. However, at the highest Reynolds number ($R_\lambda \approx 450$) available for $M_t \approx 0.3$, the asymptotic constant decreases to around 0.82.

One could extend the incompressible scaling, $\sqrt{\langle p^2 \rangle} \sim \langle \rho \rangle u^2$, and normalize by mean pressure and obtain $\sqrt{\langle p^2 \rangle}/\langle p \rangle \sim \langle \rho \rangle u^2 / \langle \rho \rangle R \langle T \rangle \sim u^2/c^2 \sim M_t^2$. Recent numerical simulations show that $\sqrt{\langle p^2 \rangle}/\langle p \rangle$ appear to grow slightly faster with M_t, as $M_t^{2.2}$, a minor deviation from the predicted M_t^2 scaling (Donzis & Jagannathan, 2013*a*). This departure can be ascertained by exploring the scaling of the individual components of pressure. When $\sqrt{\langle {p'_s}^2 \rangle}$ is scaled by the mean pressure, as shown in figure IV.1(b), we see excellent agreement with M_t^2 and almost no Reynolds number dependence. However, when the dilatational pressure is scaled similarly (in figure IV.1(c)), a steeper exponent is observed at low M_t (close to 4.0) while an emerging M_t^2 scaling is seen for $M_t \geq 0.3$. The high exponent at low M_t may explain the minor deviation seen in Donzis & Jagannathan (2013*a*).

In order to assess the relative contributions of the dilatational and solenoidal pressure, the ratio of their root-mean-square values is considered in figure IV.2(a).

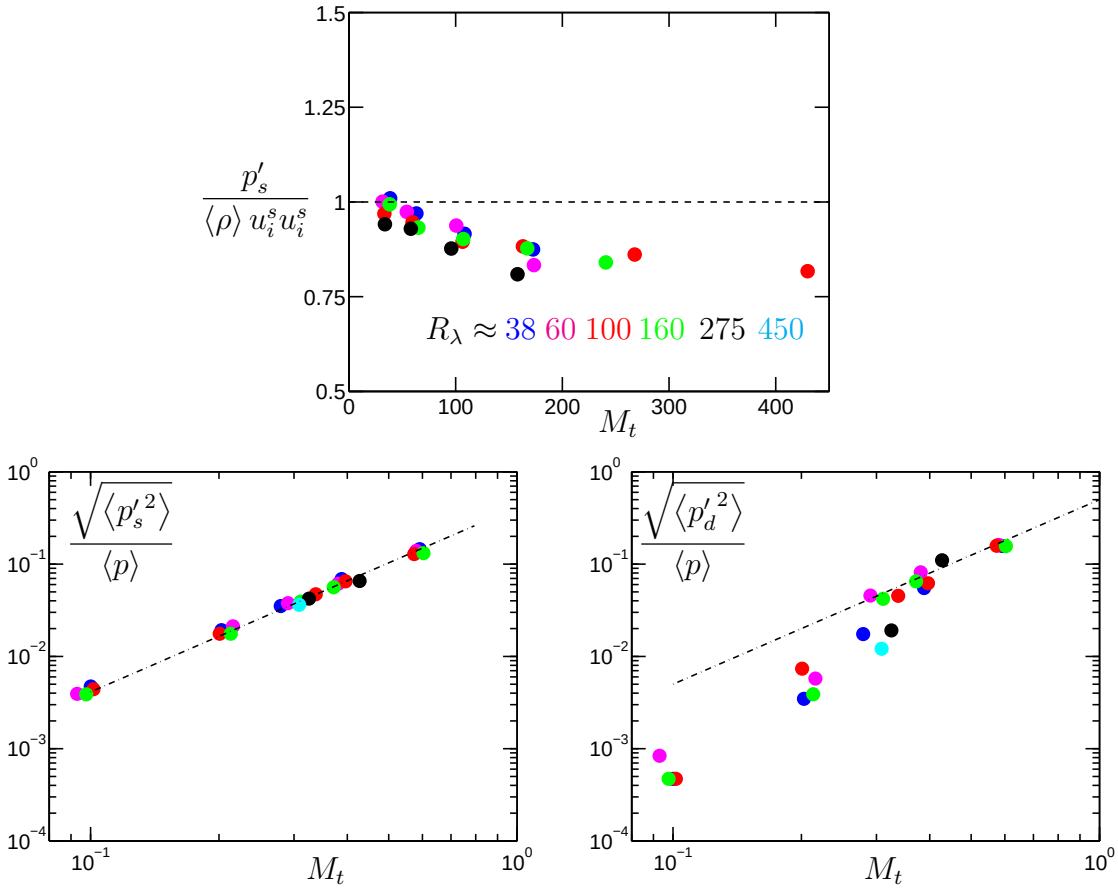

Figure IV.1. Scaling of solenoidal and dilatational pressure. Dashed lines indicate a slope of 2. Different colors for R_λ according to the following: $R_\lambda \approx 38$ (blue), 60 (magenta), 100 (red), 160 (green), 275 (black), 450 (cyan).

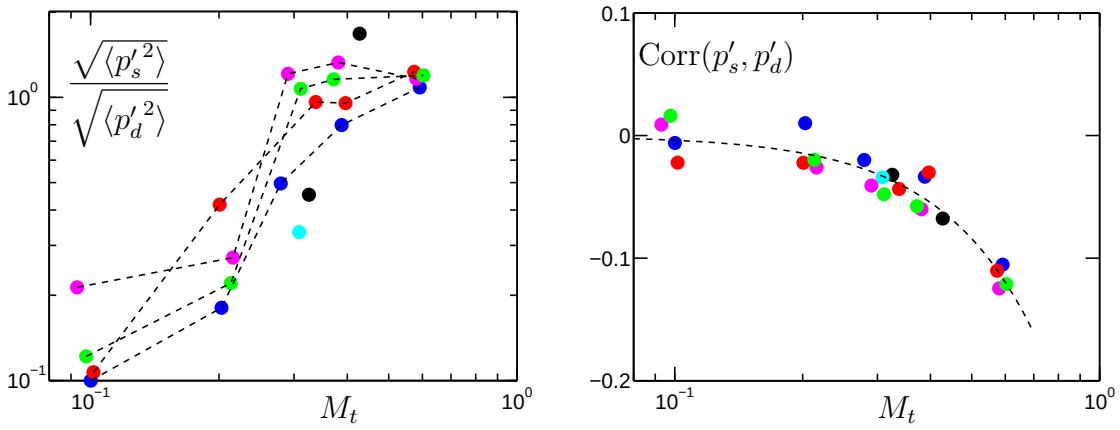

Figure IV.2. (a) Ratio of dilatation to solenoidal pressure fluctuations. (b) Correlation coefficient between solenoidal and dilatational pressure respectively ($C_p = -0.334 M_t^2$). Colors for different Reynolds numbers as in figure IV.1.

While at low M_t, $\sqrt{\langle p_d'^2 \rangle}$ is only about 10% of $\sqrt{\langle p_s'^2 \rangle}$, there is a sharp increase around $M_t \approx 0.3$ Beyond $M_t \approx 0.3$, the ratio remains close to 1.0, with a Reynolds number dependence weaker than at lower M_t. Here, we note again the qualitative change in behavior seen at $M_t \approx 0.3$. The appearance of strong fluctuations in dilatational pressure seems to have a sizeable effect on the overall behavior of turbulence.

While a linear analysis of the (inviscid) governing equation may suggest some independence between the components of pressure, it is expected that in real flows, solenoidal and dilatational pressure may in fact be correlated to a degree that would depend on the Reynolds as well as Mach numbers. The correlation coefficient is plotted in figure IV.2(b). While at low Mach numbers the solenoidal and dilatational pressure behave independently, at higher Mach numbers they become more negatively correlated. One can also see a decreasing dependence on Reynolds number

as M_t increases. If by lack of any theoretical guidance, one assumes a power law scaling in M_t, the data is seen to be consistent with $C_p = -0.334 M_t^2$. Also, since by construction, correlation coefficients can take values in the interval $[-1, 1]$, this expression is clearly inadequate for higher M_t.

IV.A.2. p.d.f. of Pressure

It is also of interest to study fluctuations that are not close to the mean. For this higher order moments or even the entire p.d.f. is useful. The skewness of pressure, $S_p = \langle p'^3 \rangle / \langle p'^2 \rangle^{3/2}$, which measures the asymmetry of the p.d.f., has been shown to change from negative to positive as M_t is increased (Donzis & Jagannathan, 2013*a*). The transition from negative to positive also occurs around $M_t \approx 0.3$, similar to other flow statistics presented in previous sections that show a qualitative change around $M_t \approx 0.3$. Negative and positive skewness physically represent an increased likelihood of low and high pressure regions in the flow respectively and indicates a qualitative difference in the role of pressure at low and high M_t. In figure IV.4(a) we show this phenomenon at $R_\lambda \approx 160$ for different M_t. Though this may be a result of pressure being a positive quantity (Blaisdell *et al.*, 1993) and therefore pressure fluctuations being bounded from the negative and not from the positive side ($p' > -\langle p \rangle$), it does not provide a clear physical mechanism for this change. One could explore the p.d.f. of solenoidal and dilatational pressure individually to further understand this behavior. The p.d.f. of p'_s (f_{ps}) shown in figure IV.4(b), has a negligible dependence on M_t and remains negatively skewed for the range of M_t investigated. Similar to incompressible turbulence, the positive fluctuations follow a Gaussian distribution

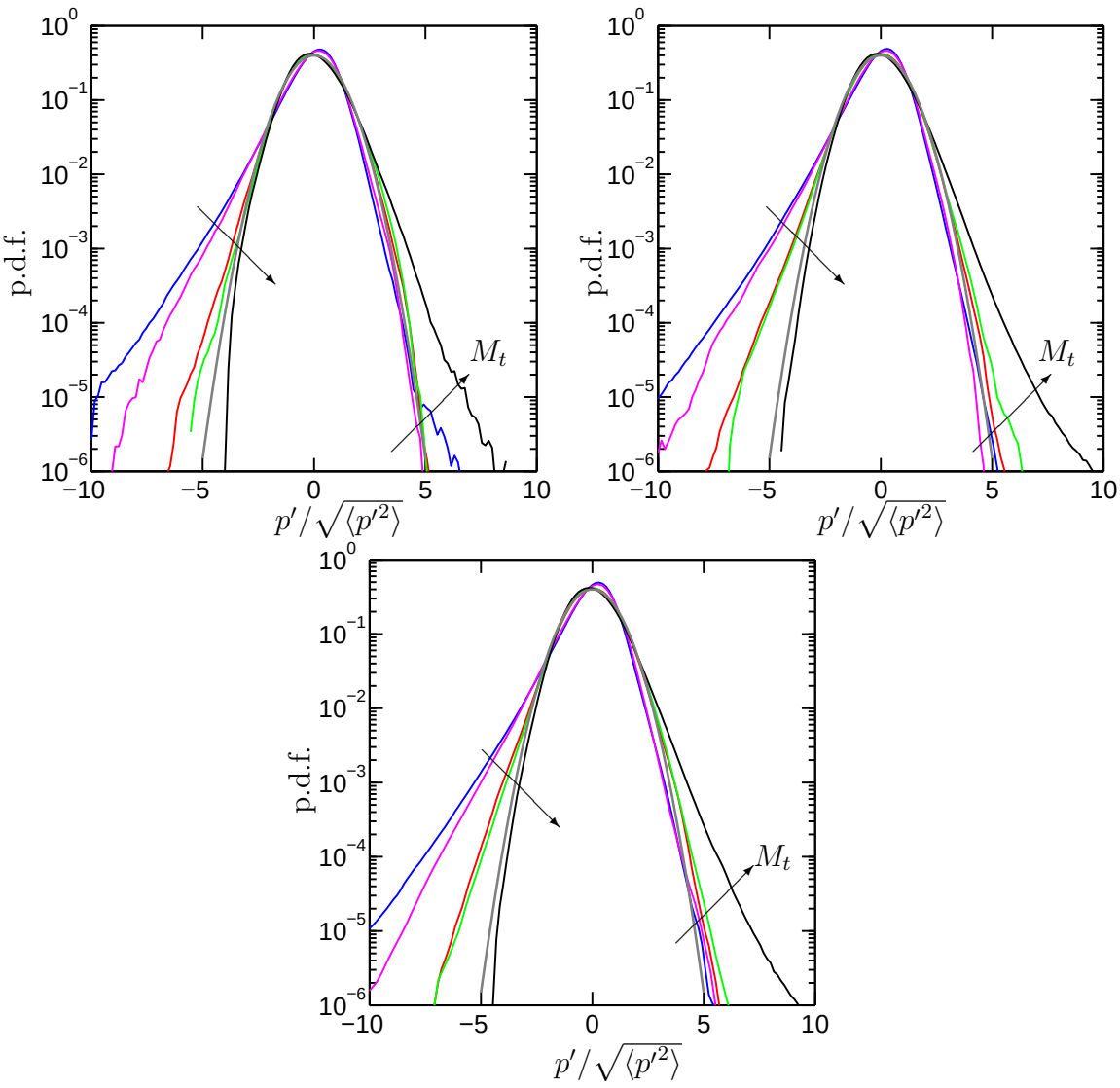

Figure IV.3. p.d.f. of pressure at different M_t for (a) $R_\lambda \approx 60$, (b) $R_\lambda \approx 100$ and (c) $R_\lambda \approx 160$. Arrows indicate the direction of increasing M_t. Lines in gray correspond to a Gaussian distribution. Colors for different M_t are according to the following: $M_t \approx 0.1$ (blue), 0.2 (magenta), 0.3 (red), 0.4 (green), 0.6 (black).

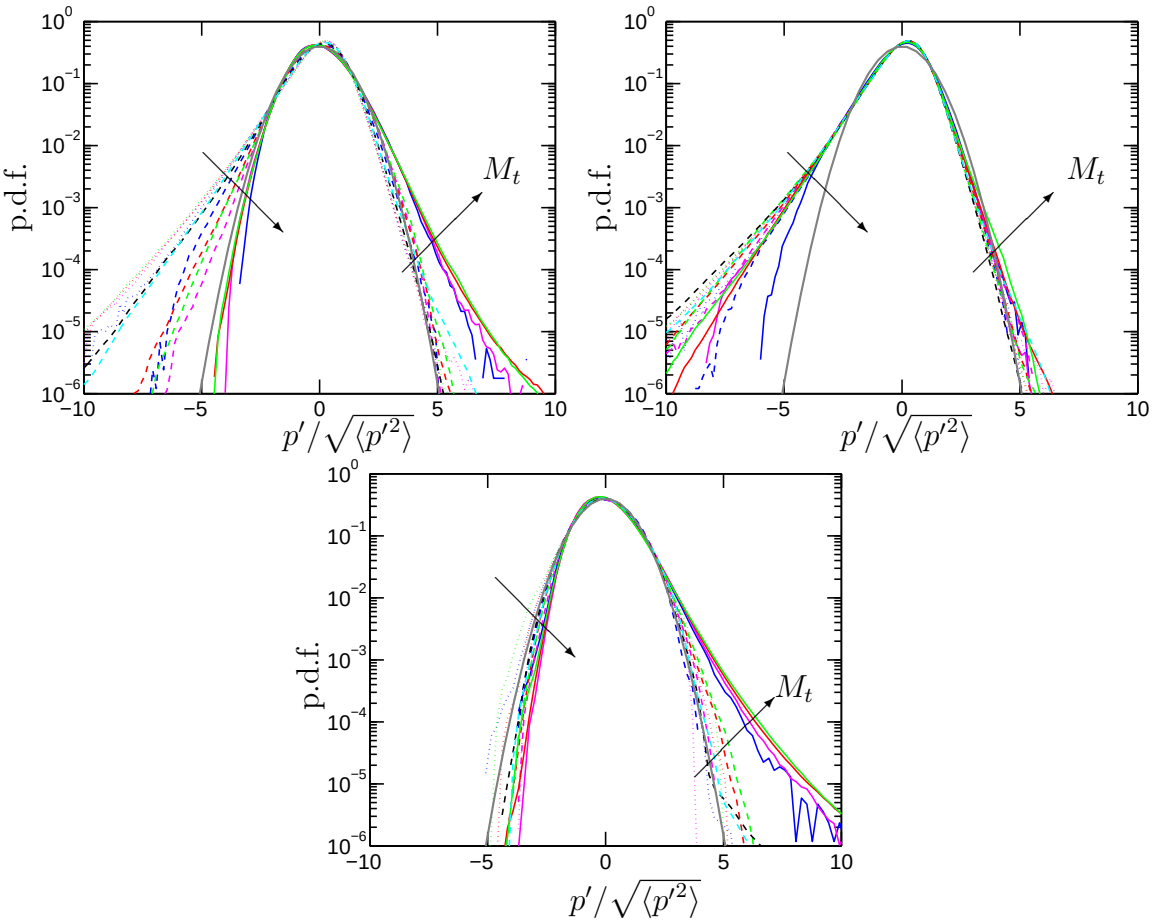

Figure IV.4. p.d.f. of (a) pressure and its (b) solenoidal and (c) dilatational components for different R_λ and M_t. Lines in gray correspond to a Gaussian distribution. Different line styles for M_t follow: $M_t \approx 0.1$ (dotted), 0.3 (dashed), 0.6 (solid). Arrows are in the direction of increasing M_t and colors for different R_λ according to figure IV.1.

(Pumir, 1994; Vedula & Yeung, 1999). Nevertheless, the p.d.f. of p'_d (f_{pd}), shown in figure IV.4(c), remains close to Gaussian for negative fluctuations, but becomes positively skewed beyond $M_t \approx 0.3$. Thus the positive skewness of pressure at high M_t appears to be a direct result of the large contributions of dilatational pressure. This conclusion is strengthened if we consider the following observations. First, since p'_d becomes anti-correlated with p'_s at high M_t (see figure IV.2(b)) and f_{ps} is skewed to the left, we can expect the tails of f_{pd} to be wider on the right. As long as this correlation is valid and p'_s remains skewed to the left, p'_d would continue to be skewed to the right. Second, in figure IV.2 (a), we already observed that as M_t is increased beyond 0.3, the dilatational pressure fluctuations tend to be of the same order as that of its solenoidal counterpart which means that strong positive fluctuations are due to dilatational effects. While this result applies to the entire domain, it seems natural to investigate the differences in regions of low and high dilatational motions. Though the dilatational effects seem very prominent, it is also important to account for the effects of solenoidal motions (if any). The individual effect of each type of motion has been commonly studied by computing statistical features of enstrophy and dilatation as conditioning variables of both hydrodynamic and thermodynamic fluctuations. This is the focus of the next sections.

IV.A.3. p.d.f. of Enstrophy

The Reynolds and Mach number dependence of p.d.f. of enstrophy is shown in figure IV.5 at $R_\lambda \approx 100$ and 160. While fluctuations close to the mean show very little dependence on M_t, stronger fluctuations show a significant monotonic

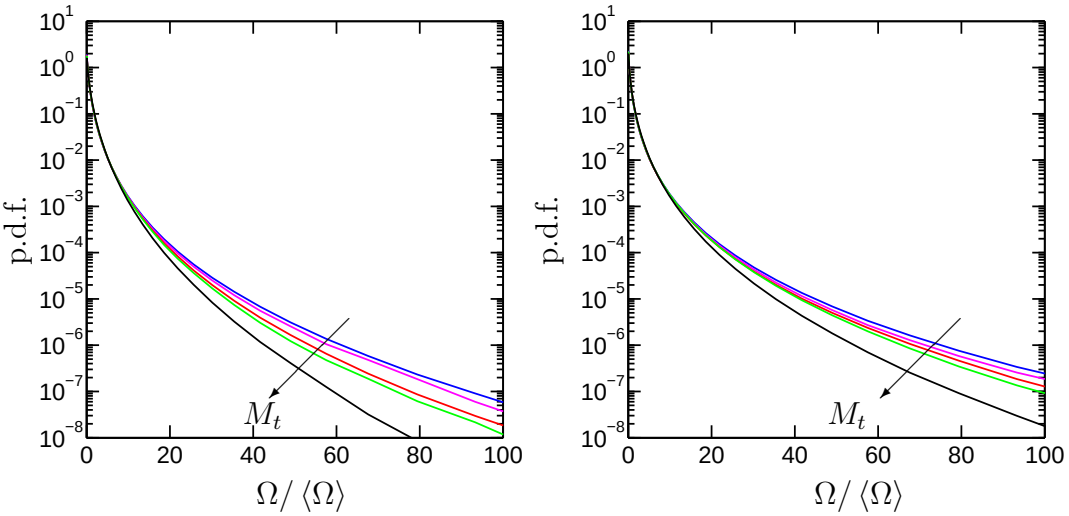

Figure IV.5. p.d.f of enstrophy at different M_t for (a) $R_\lambda \approx 100$ and (b) $R_\lambda \approx 160$. Arrows indicate the direction of increasing M_t.

dependence on M_t. The tails of the p.d.f. recede with increasing M_t regardless of the Reynolds number indicating that with increasing levels of compressibility, high-enstrophy regions become less prominent. Since high-pressure regions are more probable to occur at high M_t (due to the positive skewness of the f_p), and the tails of enstrophy become narrower with increasing M_t, it is possible that enstrophy and high-pressure regions may not be as well-correlated as low-pressure regions are. This can be directly tested by studying the conditional p.d.f. of pressure given enstrophy as shown in figure IV.6. At low M_t, consistent with our previous observations, the p.d.f. is seen to be negatively skewed. The skewness, however, tends to increase (in magnitude) with increasing enstrophy, showing that at low M_t, low-pressure and high-enstrophy regions tend to co-exist, similar to incompressible turbulence.

However, at high M_t, the p.d.f., which is skewed to the right, shows very little dependence on enstrophy for a wide range of values of the latter. For a range of fluctuations of enstrophy, the p.d.f.s collapse well with very minor differences occurring

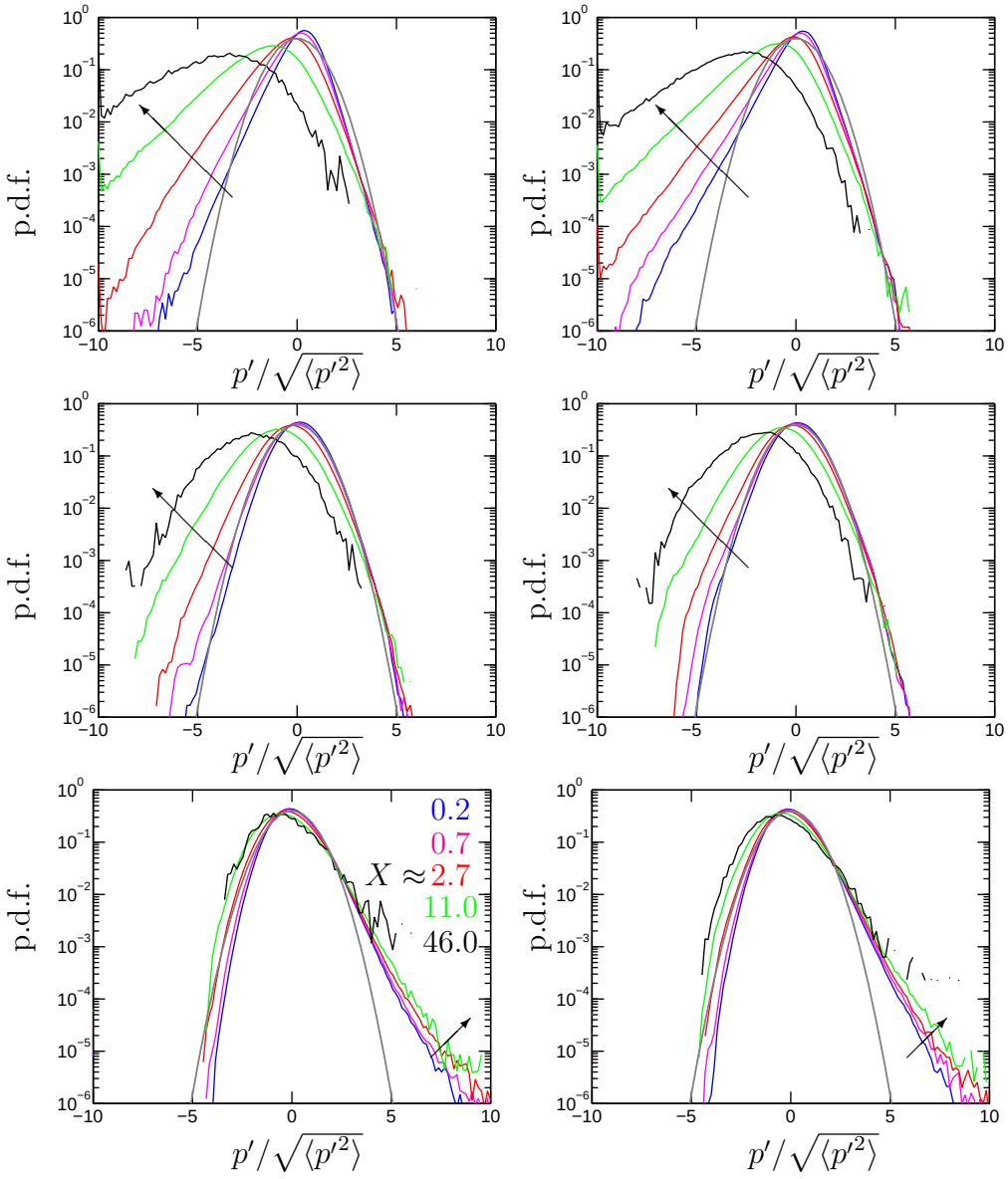

Figure IV.6. Conditional p.d.f. of pressure given enstrophy for different Reynolds and Mach numbers. The left and right panels are at $R_\lambda \approx 100, 160$. The rows from top to bottom are at $M_t \approx 0.1, 0.3, 0.6$ respectively. Arrows indicate increasing magnitude of X, where X is $\Omega/\langle\Omega\rangle$. Solid and dashed lines stand for negative and positive dilatation values.

near the tails. This shows that with increasing M_t, the correlation between pressure fluctuations and enstrophy tend to decrease. An implication of this result is that it may not be appropriate, for instance, to visualize voritices by identifying regions of low-pressure. The negative fluctuations stay close to a standard Gaussian distribution with weak dependence on the magnitude of the enstrophy. This indicates that at high M_t, the correlation between low-pressure region and high enstrophy too is weakened. This de-correlation between enstrophy and low/high pressure can be interpreted in light of the results in figure IV.2. At low M_t, the pressure fluctuations are mainly solenoidal, and thus we see low-pressure and high-enstrophy regions to be correlated, similar to incompressible turbulence. However, as M_t increases, increasing dilatational pressure fluctuations have a marked effect on the overall behavior of pressure. the correlation between pressure and enstrophy reduces.

This can be further explored by studying how the individual components of pressure change with enstrophy. The c.p.d.f. of solenoidal pressure given enstrophy is shown in figure IV.7. While the dependence on enstrophy is evident, there is only a weak variation with M_t. The c.p.d.f. remains negatively skewed for the range of M_t investigated, while the positive fluctuations appear to follow a standard Gaussian distribution. The tails of the p.d.f. are seen to become wider on the left with increasing enstrophy. Thus high-enstrophy and low solenoidal pressure regions appear to be strongly correlated. The correlation is seen to be only weakly dependent on M_t (compare for instance, green curves in the left panel) and R_λ (compare left and right panels). The positive fluctuations of solenoidal pressure, however, remain close to a Gaussian distribution. Thus, we believe that the occurrence of high-pressure regions

at high M_t, may not be primarily caused due to solenoidal effects.

The c.p.d.f. of dilatation pressure, on the other-hand, shows a dependence on M_t. While at low M_t, the positive and negative fluctuations remain close to a standard Gaussian distribution with a weak dependence on M_t, at high M_t, the tails become positively skewed and slightly wider with increasing enstrophy. Overall, the Reynolds number dependence appear to be weak. It seems that at high M_t, behavior of pressure appear to be similar to that of its dilatational component. It is thus natural to investigate the effect of dilatation on the statistics of pressure.

IV.A.4. p.d.f. of Dilatation

The behavior of dilatation is particularly relevant in understanding the effects of compressions and expansions in the flow. Though somewhat arbitrary, shocklets are commonly defined as regions with dilatation less than a threshold, $\theta < -3\left\langle \theta'^2 \right\rangle^{1/2}$ (Samtaney *et al.*, 2001) and have been suggested to have different effects on the flow. For instance, shocklets can increase the rate of dilatational dissipation which results in the conversion of turbulent kinetic energy to internal energy (Lee *et al.*, 1991). While considerable attention has been given to the role of shocklets, the effect of expansions has not been investigated in any detail. A strong local expansion, for instance, can result in a large value of pressure-dilatation correlation, which, depending on the pressure fluctuations, could bring about an instantaneous energy transfer between kinetic and internal energy. To represent the flow physics accurately, these physical mechanisms need to be incorporated into turbulence models for which a better understanding of pressure, dilatation and its correlation is required. We con-

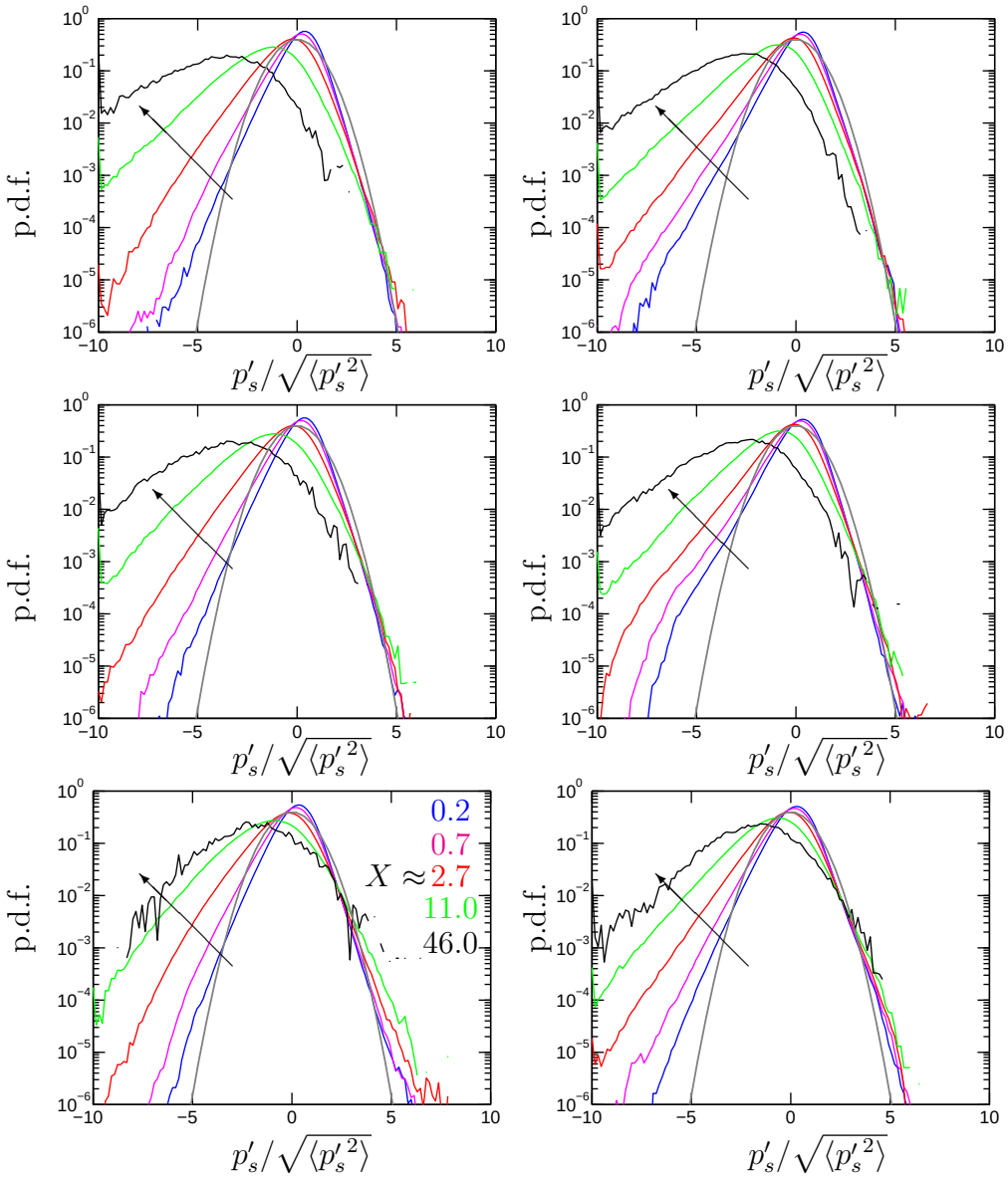

Figure IV.7. Conditional p.d.f. of solenoidal pressure given enstrophy for different Reynolds and Mach numbers. The left and right panels are at $R_\lambda \approx 100, 160$. The rows from top to bottom are at $M_t \approx 0.1, 0.3, 0.6$ respectively. Arrows indicate increasing magnitude of X, where X is $\Omega'/\langle\Omega\rangle$. Lines in gray correspond to a Gaussian distribution.

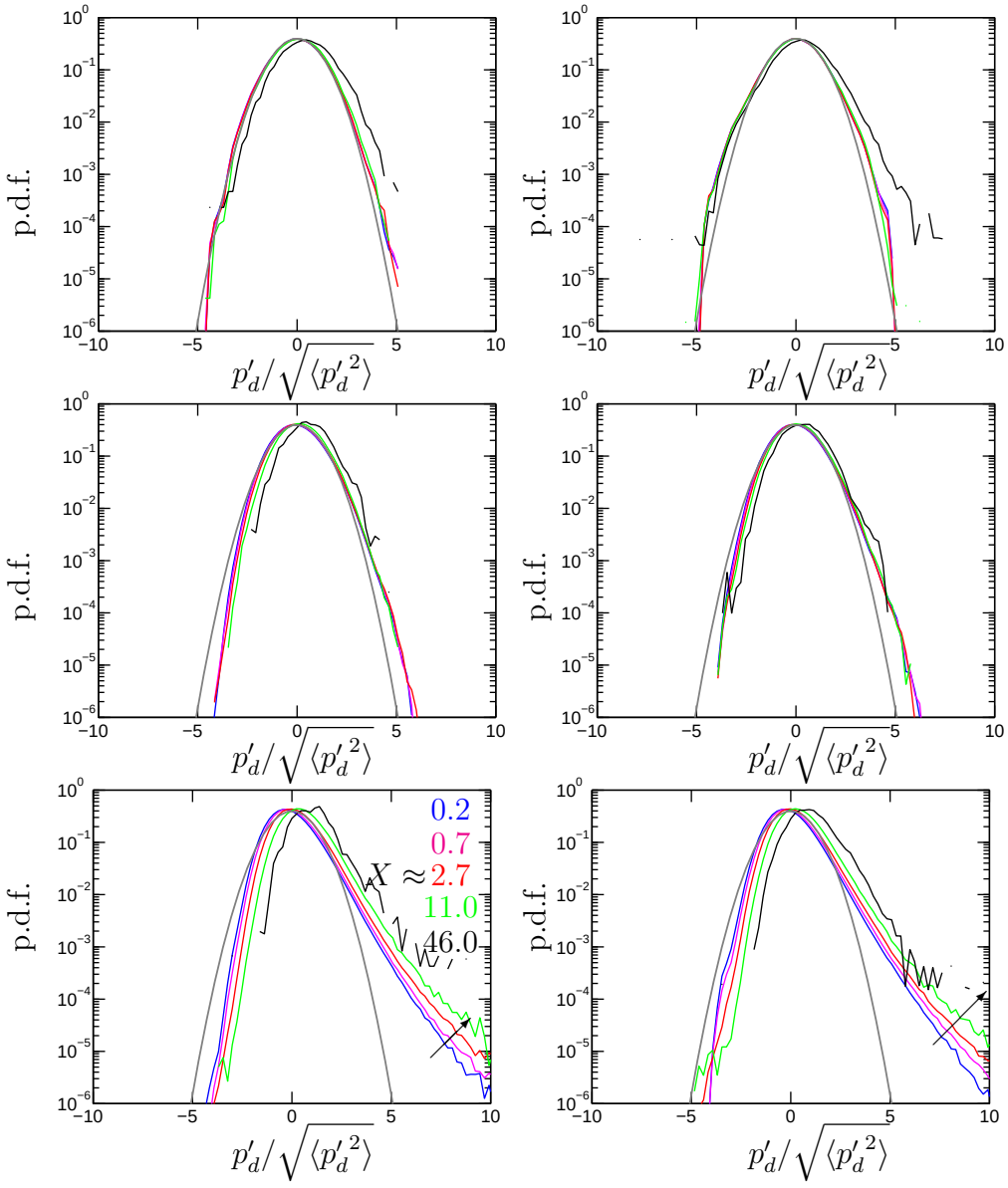

Figure IV.8. Conditional p.d.f. of dilatational pressure given enstrophy for different Reynolds and Mach numbers. The left and right panels are at $R_\lambda \approx 100, 160$. The rows from top to bottom are at $M_t \approx 0.1, 0.3, 0.6$ respectively. Arrows indicate increasing magnitude of X, where X is $\Omega/\langle\Omega\rangle$. Lines in gray correspond to a Gaussian distribution.

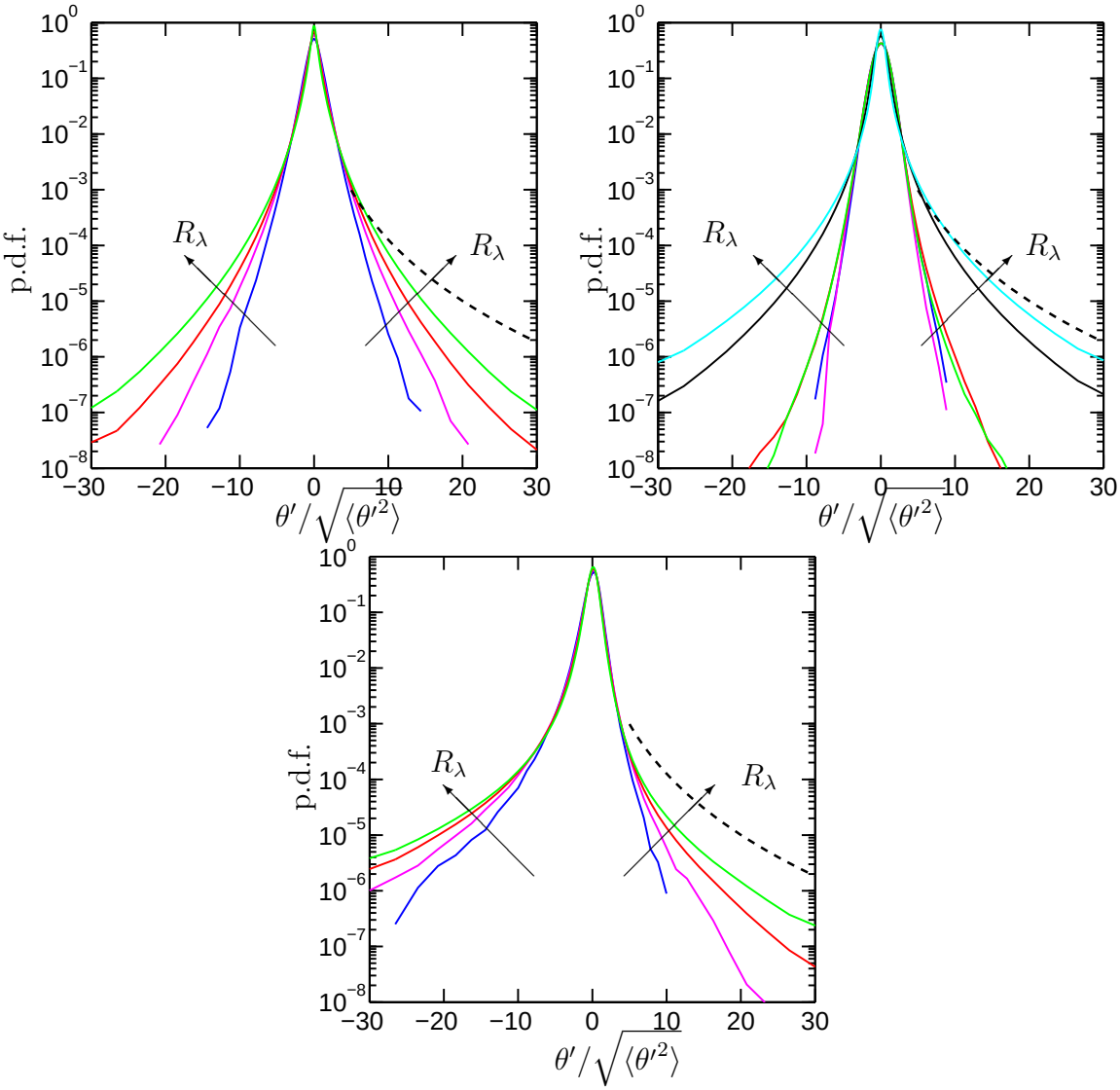

Figure IV.9. p.d.f. of dilatation at $M_t \approx$ (a) 0.1 (b) 0.3 (c) 0.6. Symbols for different Reynolds numbers as in figure III.2. Arrows are in the direction of increasing R_λ. Dashed lines are a standard log-normal distribution.

sider the Reynolds and Mach number variation of the p.d.f. of normalized dilatation $(\theta'/\langle\theta'^2\rangle^{1/2})$ for $M_t \approx 0.1, 0.3, 0.6$ in figure IV.9. At low M_t, the tails of the p.d.f. become wider with R_λ, but remains symmetric throughout, indicating that regions of large positive and negative dilatation are equally likely to appear intermittently. This R_λ effect is typical of all velocity gradients in incompressible turbulence (Donzis *et al.*, 2008*b*). While the symmetry is still maintained at $M_t \approx 0.3$ for all R_λ, the tails of the p.d.f., on the other hand, recede and tend to be close to Gaussian for a wide range of fluctuations for R_λ less than 175. The receding of the tails of the p.d.f. implies that large compressions or expansions are less likely to appear at $M_t \approx 0.3$ than at $M_t \approx 0.1$ for the same R_λ. It is conceivable that this decline in the appearance of large gradients in the flow is related to the change in several flow statistics at $M_t \approx 0.3$ that has been investigated so far. For higher R_λ, the tails grow wider but retain the symmetry. Eventually at $M_t \approx 0.6$, the p.d.f. becomes asymmetric with wider tails on the left, that grow with R_λ.

More quantitative information about the large fluctuations can be obtained by computing high order moments, in particular skewness and flatness factors, $F_\theta = \langle\theta'^4\rangle / \langle\theta'^2\rangle^2$, which quantifies the asymmetry and the wideness of the tails. The variation of skewness and flatness of dilatation with M_t is seen in figure IV.10(a) and (b). Beyond $M_t \approx 0.3$, the negative skewness increases (in magnitude) with M_t, a result also reported in the literature (Lee *et al.*, 1991; Pirozzoli & Grasso, 2004; Wang *et al.*, 2012). For decaying compressible turbulence with initial $R_\lambda \approx 60$ and $M_t \approx 0.6$, the skewness and flatness observed in Lee *et al.* (1991) when the flow becomes turbulent is approximately -1.75 and 12.5 respectively. Taking into account

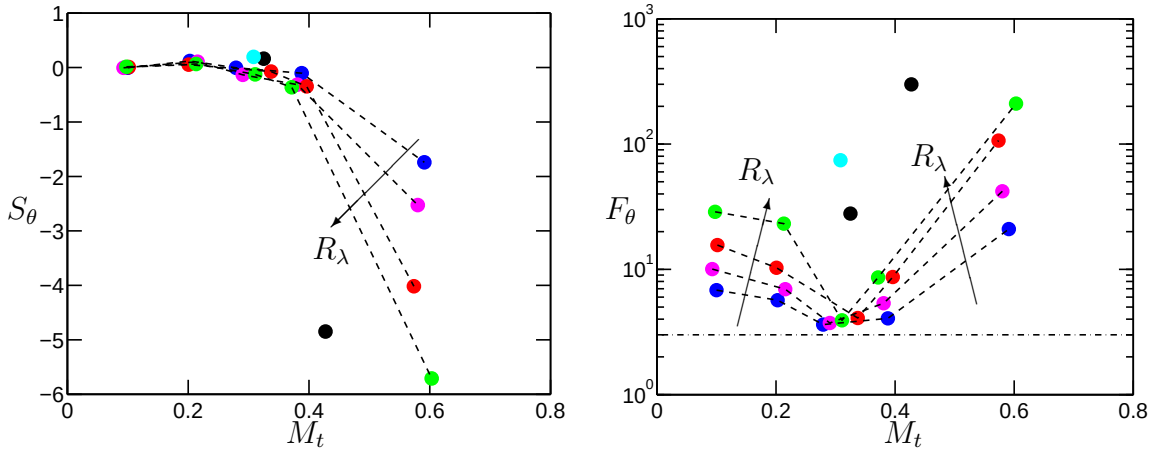

Figure IV.10. Skewness and Flatness of dilatation. Arrows are in the direction of increasing R_λ.

that the Reynolds and Mach number would decay before the flow becomes turbulent, the skewness value from our simulation of about -2.53 at $R_\lambda \approx 60$ and $M_t \approx 0.3$ is in good agreement. As M_t is decreased, the magnitude of both the skewness and flatness tends to decrease, which is also seen in their decaying simulation after the flow becomes turbulent. While the R_λ dependence of skewness is negligible at low M_t, there is a substantial change with M_t beyond $M_t \approx 0.4$. The flatness values, on the other hand, show a monotonic decrease with M_t until $M_t \approx 0.3 - 0.4$ when it reaches a value around 3.0 (Gaussian) for $R_\lambda < 275$, and then increase sharply.

A large flatness value, $F_\theta = \langle \theta'^4 \rangle \, / \, \langle \theta'^2 \rangle^2$, such as seen in figure IV.10, typically indicates that regions of large positive and negative dilatation appear intermittently in the flow. The percentage volume of their occurrence is given in Table IV.A.4. While regions of strong compressions ($\theta' / \langle \theta'^2 \rangle^{1/2} < -3$) and expansions ($\theta' / \langle \theta'^2 \rangle^{1/2} > 3$) are equally likely to occur at low M_t, both have an increased propensity to appear at higher Reynolds numbers. However, at high M_t, this Reynolds number dependence

R_λ	M_t	$(-\infty,-3]$	$[-3,-2)$	$[-2,-1)$	$[-1,0)$	$[0,1)$	$[1,2)$	$[2,3)$	$[3,\infty)$
38	0.1	0.64	2.04	9.90	37.04	37.87	9.96	1.98	0.56
60	0.1	0.82	1.95	8.63	38.05	39.36	8.51	1.88	0.79
100	0.1	0.90	1.67	7.05	40.45	40.32	7.04	1.67	0.91
160	0.1	0.96	1.46	5.71	42.05	41.63	5.73	1.47	0.97
38	0.3	0.27	2.37	12.18	35.11	34.79	13.23	1.76	0.29
60	0.3	0.23	2.34	13.14	33.53	35.43	13.19	2.02	0.13
100	0.3	0.38	2.22	12.29	34.38	35.95	12.62	1.90	0.25
38	0.6	0.97	2.21	9.23	33.73	42.12	10.37	1.13	0.24
60	0.6	1.00	1.71	7.92	35.93	43.07	8.92	1.17	0.29
100	0.6	0.99	1.38	6.27	36.20	47.55	6.62	0.74	0.25
170	0.6	0.87	1.37	6.71	36.83	46.09	7.08	0.80	0.26

Table IV.1. Percentage volume of dilatation in different bins.

weakens and compressions are about four times more likely to occur than expansions at any given Reynolds number. As we will see momentarily, they have different effects on the flow.

It is expected that dilatation, through the coupling of energy equations by the pressure-dilatation correlation, also affects the fluctuations of thermodynamic variables. Consider the Reynolds decomposition of an ideal gas

$$\frac{p'}{\langle\rho\rangle R \langle T\rangle} = \frac{\rho'}{\langle\rho\rangle} + \frac{T'}{\langle T\rangle} + \frac{\rho' T'}{\langle\rho\rangle \langle T\rangle} - \frac{\langle\rho' T'\rangle}{\langle\rho\rangle \langle T\rangle}, \tag{4.1}$$

which can be used to examine the relative contributions of each of these terms for different M_t at different levels of dilatation. The conditional expectation of each term given dilatation is shown in figure V.17. In part (a) of the figure we see that at $M_t \approx 0.1$, the conditional means are symmetric with respect to dilatation, supporting our earlier observation that at low M_t, the thermodynamic fluctuations tend to be the same regardless of whether the flow experiences compressions or expansions, contingent on the magnitude of dilatation remaining the same. It is also clear

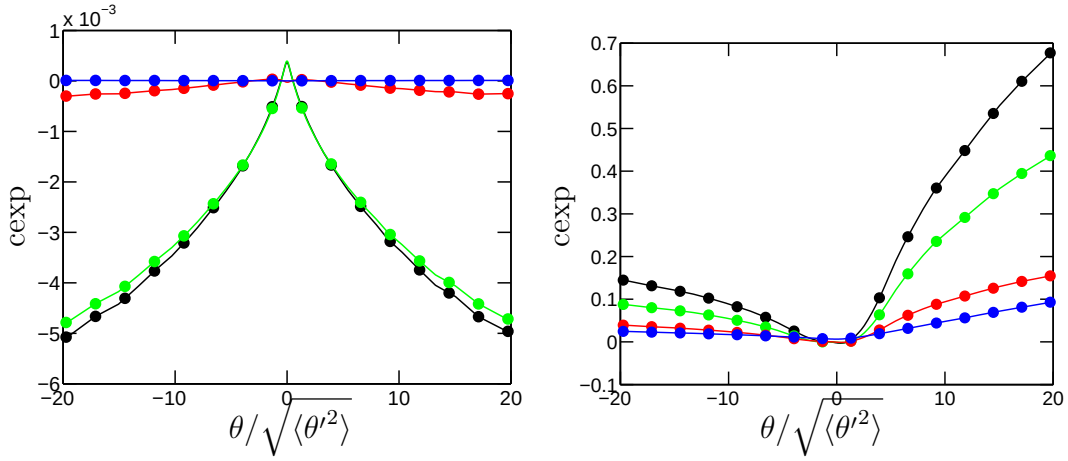

Figure IV.11. Conditional expectation $\langle X|\theta'/\sqrt{\langle\theta'^2\rangle}\rangle$ given dilatation with $X = p'/\langle\rho\rangle R\langle T\rangle$ (black), $X = \rho'/\langle\rho\rangle$ (green), $X = T'/\langle T\rangle$ (red), $X = \rho' T'/\langle\rho\rangle\langle T\rangle$ (blue) at $M_t \approx$ (a) 0.1 and, (b) 0.6 at $R_\lambda \approx 160$.

that the dominant contributor to pressure fluctuations is density while temperature and density-temperature correlation are negligibly small. At high M_t qualitatively different picture emerges. 1. The symmetry between positive and negative values of dilatation is no longer present indicating that expansions and compressions have different effects on the flow. 2. Second, it can be seen that strong expansions and large positive pressure fluctuations (high pressure) are more likely to appear together. From an intuitive point of view one can argue that high pressure regions act as precursors for strong expansions or vice-versa.

These expansions may result from an over-compressed region of fluid, as found for instance in a shocklet, which cannot sustain the compression beyond a threshold and begins to expand. However, the timescales associated with these two processes can be quite different with the compressions occuring at a smaller time scale than expansion. This may be a plausible reason for the high-pressure regions to be more correlated with expansions rather than compressions. A more insightful

analysis to identify the physical process behind the occurence of high-pressure regions and expansions can be obtained by investigating the conditional statistics of pressure (and subsequently dilatation) given the time rate of change of dilatation. The rate of dilatation, δ, gives a measure of how much the flow locally expands or contracts and has been used recently in Suman & Girimaji (2013) as a measure of compressibility. 3. Third, in regions of large expansions, temperature fluctuations and the density-temperature correlation are significantly higher than in corresponding regions of compressions. Therefore, it seems natural to include the effects of density-temperature correlation at high M_t. While not a very general and accurate approximation, it may still be possible to assume that density and temperature are isentropic, following which we have the relation (Donzis & Jagannathan, 2013*a*),

$$p/\langle p\rangle = (\rho/\langle\rho\rangle)^{\gamma} = (T/\langle T\rangle)^{\frac{\gamma}{\gamma-1}}. \tag{4.2}$$

By linearizing the above equation, the fluctuations of thermodynamic quantities can be related as, $p'/\langle p\rangle \approx \gamma\rho'/\langle\rho\rangle \approx (\gamma/\gamma-1)\,T'/\langle T\rangle$. Substituting these relations in Eq. (4.1), we get

$$\frac{p'}{\langle\rho\rangle\, R\,\langle T\rangle} \approx \gamma\frac{\rho'}{\langle\rho\rangle} + (\gamma-1)\left(\frac{\rho'}{\langle\rho\rangle}\right)^2, \tag{4.3}$$

where the quadratic term in density fluctuations is due to the density-temperature correlation. It is now possible to compare with DNS data if this approximation is valid by investigating the conditional expectation of pressure given density and is shown in figure IV.12 for $R_\lambda \approx 60$. For reference, the RHS of Eq. (4.2) is also included with and without the density-temperature correlation. While the fluctuations in density are very small for $M_t \approx 0.1$, it becomes significant at high M_t, and more specifically, the positive fluctuations are larger. As a result of which, the fluctuations

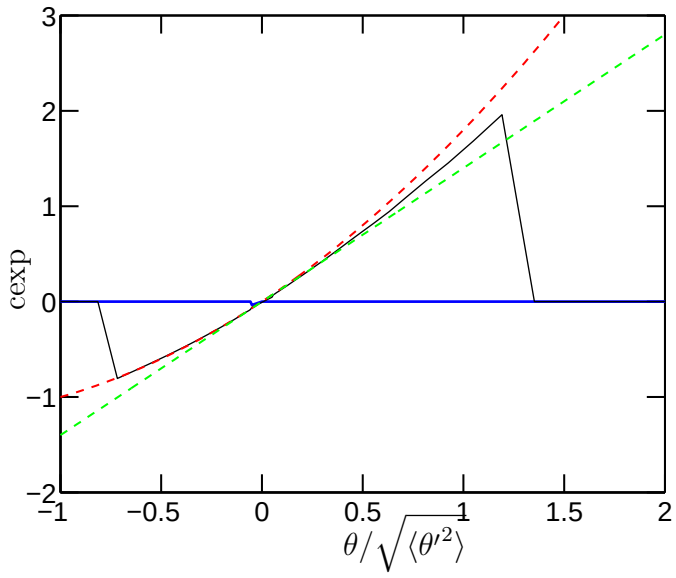

Figure IV.12. Conditional expectation of $\langle p\rangle/\langle\rho\rangle R\langle T\rangle$ given density at $R_\lambda \approx 60$ and $M_t \approx 0.1$ (blue) and 0.6 (black). The linearized isentropic assumption with and without density-temperature correlation are showed i red and green color respectively.

in pressure are positive and larger in magnitude. Since density fluctuations are normalized by their mean and cannot be less than -1.0, it seems that these large values of pressure, which cause the positive skewness at high M_t, are likely to be due to the density-temperature correlation which is the quadratic term in Eq. (4.3). For negative flucutations of density, the linearized isentropic assumption seems to be a very good approximation when the density-temperature correlation is included, while minor deviations are seen for large positive density fluctuations. 4. Finally, since compressions and expansions behave differently at high M_t, they may have profound effect on the flow, for instance, in energy exchanges, through the pressure-dilatation correlation.

IV.A.5. Correlation between Pressure and Dilatation

In addition to providing insight into the behavior of pressure at different values of dilatation, conditional statistics of pressure given dilatation provides information about the correlation between them, which represents a reversible exchange mechanism between kinetic and internal energy (eqns Eq. (3.1) and Eq. (3.2)). In decaying simulations, Lee *et al.* (1991) found the role of pressure-dilatation confined to the early acoustic transient time period. In many realistic applications however, systems are forced continuously and hence pressure-dilatation will continue to play a role in the energy dynamics. The conditional p.d.f. of pressure for different values of dilatation is shown in figure IV.13. At low Mach numbers ($M_t \approx 0.1$), the p.d.f. is insensitive to the sign of dilatation and Reynolds number. This means that the instantaneous value of pressure is insensitive to locally expanding or compressing fluid elements that have the same magnitude of dilatation. This has wide implications in the dynamics of energy transfer between the internal and kinetic energy modes. When the dilatation is large and negative, for example, pressure fluctuations are more likely to be negative than positive (see figure IV.13(a)). Therefore, the correlation between them, $p'\theta'$, would be positive and larger than each of them individually. When pressure-dilatation is positive, energy is transferred from internal energy to kinetic energy, an observation that can be readily inferred from eqns Eq. (3.1) and Eq. (3.2). A similar argument for expanding regions (large positive dilatation) indicates that the energy transfer is likely to be from kinetic to internal energy. For intense fluctuations, the magnitude of $p'\theta'$ would be very large and hence an instantaneous burst of energy would be transferred between kinetic and internal energy

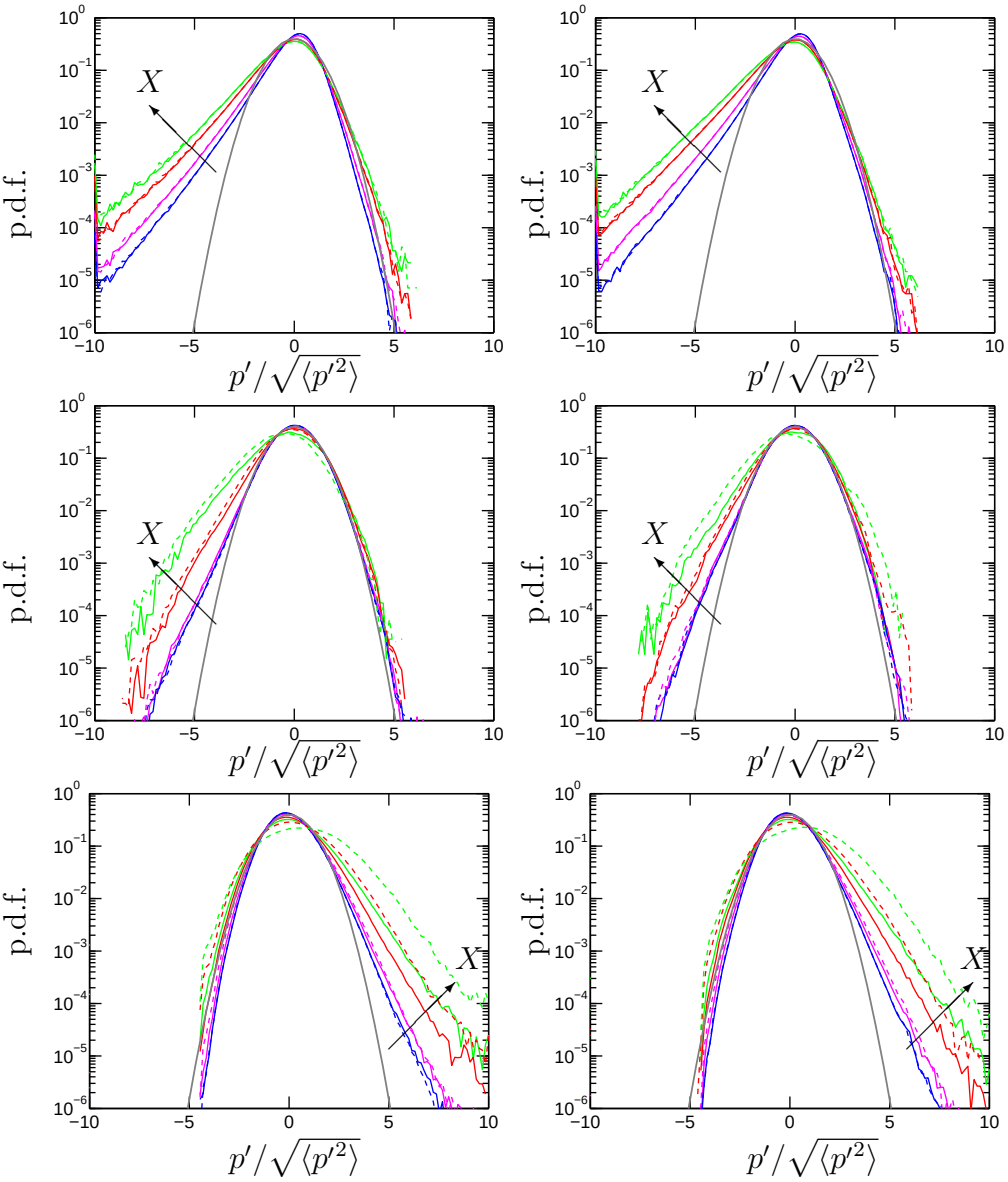

Figure IV.13. Conditional p.d.f. of pressure given dilatation for different Reynolds and Mach numbers. The left and right panels are at $R_\lambda \approx 100, 160$. The rows from top to bottom are at $M_t \approx 0.1, 0.3, 0.6$ respectively. Arrows indicate increasing magnitude of dilatation. Solid and dashed lines stand for negative and positive dilatation values. $X = \theta/\sqrt{\langle \theta'^2 \rangle}$.

modes. This is particularly intriguing because it has been suggested (Lee *et al.*, 1991) that shocklets convert kinetic energy to internal energy due to the enhanced dilatational dissipation. While a large dilatational dissipation is inevitable due to the high dilatation, its contribution, just like solenoidal dissipation, may be small compared to the instantaneous pressure-dilatation due to the pre-multiplication by viscosity for the former, which for high Reynolds flows is small. It should also be noted that dissipation facilitates only a uni-directional flow of energy (kinetic to internal) unlike $p'\theta'$ which has a bi-directional mode of energy exchange. Since the only other mechanism of energy addition is by external means (for instance, forcing terms in eqns Eq. (3.1) and Eq. (3.2)), the net energy transfer is dictated by pressure-dilatation or dissipation depending on their relative magnitudes. As mentioned before, for large positive dilatation, $p'\theta'$ is more likely to transfer energy from kinetic to internal mode, which is same as the direction of energy transfer through dissipation. Hence the net energy transfer would also be from kinetic to internal energy. It is also clear that the tails of the conditional p.d.f. become wider to the left with increasing magnitude of dilatation, generally indicating that large negative pressure fluctuations and large compressions may co-exist. Nevertheless, the positive pressure fluctuations stay closer to Gaussian and are only slightly affected by the value of dilatation.

As M_t increases ($M_t \approx 0.3$), the only change we find is the receding of the tails from the left that tends to approach Gaussian for small dilatation. But at high Mach numbers ($M_t \approx 0.6$), the tails of the p.d.f., as also seen in figure IV.4(a), become wider on the right. While the p.d.f. is uninfluenced by expansions or compressions for

Quantity	$p'\theta'$	ϵ	Net
$M_t \approx 0.1, C$	IE $\rightarrow$ KE	IE $\leftarrow$ KE	Varies
$M_t \approx 0.1, E$	IE $\leftarrow$ KE	IE $\leftarrow$ KE	IE $\leftarrow$ KE
$M_t \approx 0.6, C$	IE $\leftarrow$ KE	IE $\leftarrow$ KE	IE $\leftarrow$ KE
$M_t \approx 0.6, E$	IE $\rightarrow$ KE	IE $\leftarrow$ KE	Varies

Table IV.2. Summary of net energy exchanges for large compressions (C) or expansions (E)

small dilatations, substantial differences can be seen for large dilatations. Due to the change in the asymmetry of the p.d.f., the energy dynamics is also likely to change for $M_t \approx 0.6$. Applying the same analysis as before, but with pressure fluctuations more likely to be positive for large compressions, we can say that the net energy transfer is likely to be from kinetic to internal. For expansions, on the other hand, the net energy transfer will depend on the relative magnitudes of $p'\theta'$ and ϵ, as mentioned in Table IV.2 (row 4). It is to be noted that this picture of net energy transfer is expected to be true only for the type of forcing that has been investigated in this study, and under the assumption that the Reynolds number is high. Additionally, the instantaneous effect of transport terms have not been included. Though the net effect of transport terms is zero in homogeneous flows, they may still contribute to the instantaneous transfer of energy which is not accounted for in this study.

One could also argue that this energy transfer is mandated by the phenomenon of equipartition of energy. The instantaneous value of pressure-dilatation can be decomposed into a solenoidal and dilatational component based on pressure ($p'\theta' = p'_s\theta' + p'_d\theta'$). As $F \approx 1$ at high mach numbers, the dilatational components of pressure (and thus $p'_d\theta'$) and kinetic energy behave approximately as an harmonic oscillator tending the system to an equilibrium state regardless of their initial state

(Lee & Girimaji, 2013). While this may be true for the dilatational components, the solenoidal components are not restricted and could transfer energy in either direction. Thus, it would be more useful to analyze the total pressure-dilatation and not their individual counterparts as is done in this study.

The large dilatation could affect either or both the solenoidal and dilatational components of pressure, though one would expect the solenoidal component to be less affected. This can be ascertained by computing the conditional p.d.f. of the respective components of pressure given dilatation and is shown in figure IV.14 and figure IV.15 for different R_λ and M_t. The skewness of solenoidal pressure, which remains negative for the range of M_t investigated, increases in magnitude with the magnitude of the dilatation, indicating that large compressions or expansions are likely to be associated with large negative solenoidal pressure. The differences in solenoidal pressure for large compressions and expansions is evident only at high M_t, while at low M_t the p'_s is insensitive to the sign of dilatation. The positive fluctuations tend to be unaffected by the dilatation and M_t resembling a standard Gaussian distribution. The c.p.d.f. of dilatational pressure, on the other-hand, shows significant dependence on M_t. While the p.d.f. is Gaussian at low M_t, it becomes positively skewed at high M_t, with the skewness increasing with the magnitude of dilatation. The negative skewness, however, remains unaffected by the dilatation and resembles a standard Gaussian distribution.

While the likelihood of an occurrence of these intense events is smaller as compared to, for instance, fluctuations close to mean, their impact may be significant and has been the subject of intense research (Sreenivasan & Antonia, 1997; Donzis &

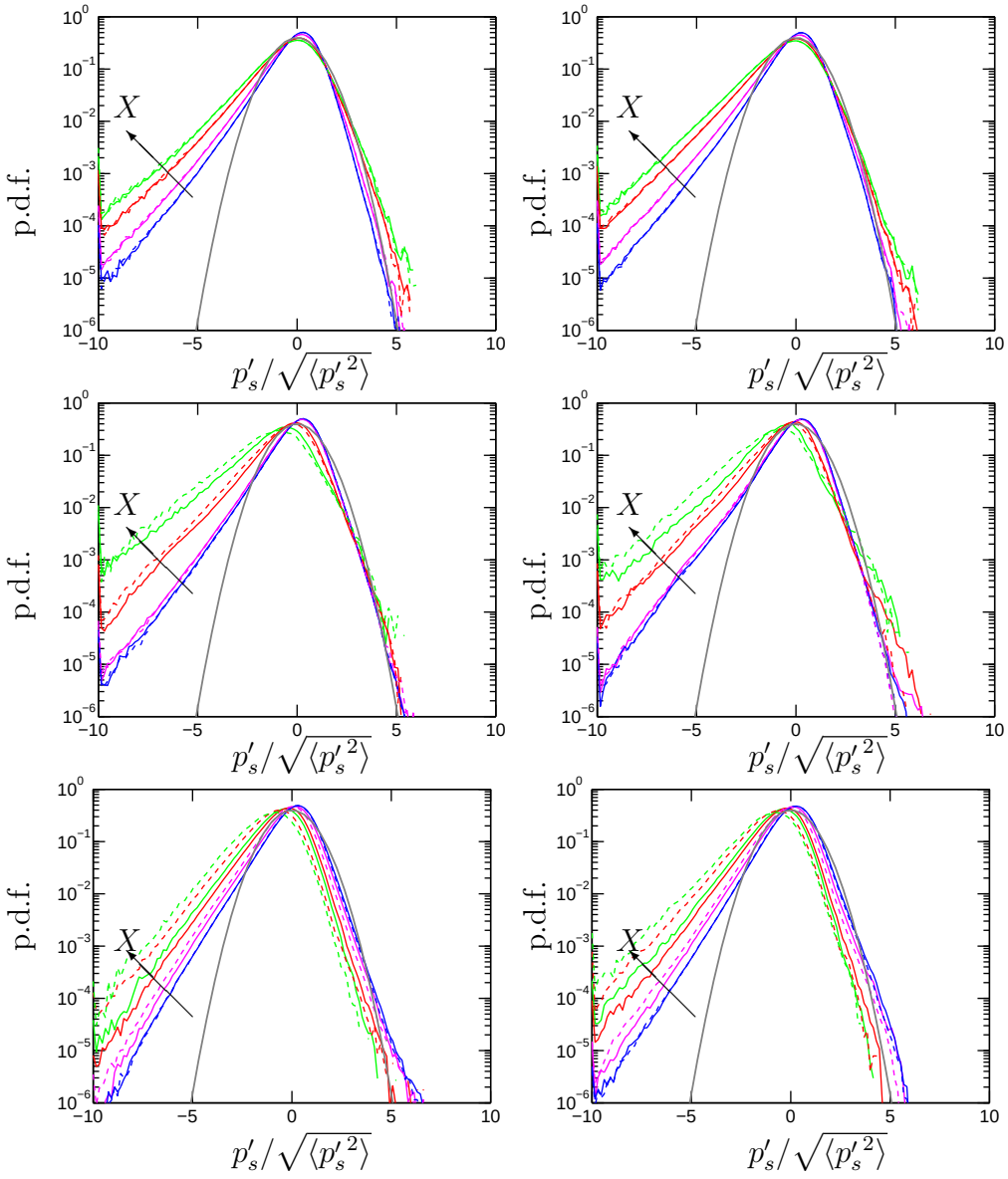

Figure IV.14. Conditional p.d.f. of solenoidal pressure given dilatation for different Reynolds and Mach numbers. The left and right panels are at $R_\lambda \approx 100, 160$. The rows from top to bottom are at $M_t \approx 0.1, 0.3, 0.6$ respectively. Arrows indicate increasing magnitude of dilatation. Solid and dashed lines stand for negative and positive dilatation values. $X = \theta/\sqrt{\langle \theta'^2 \rangle}$.

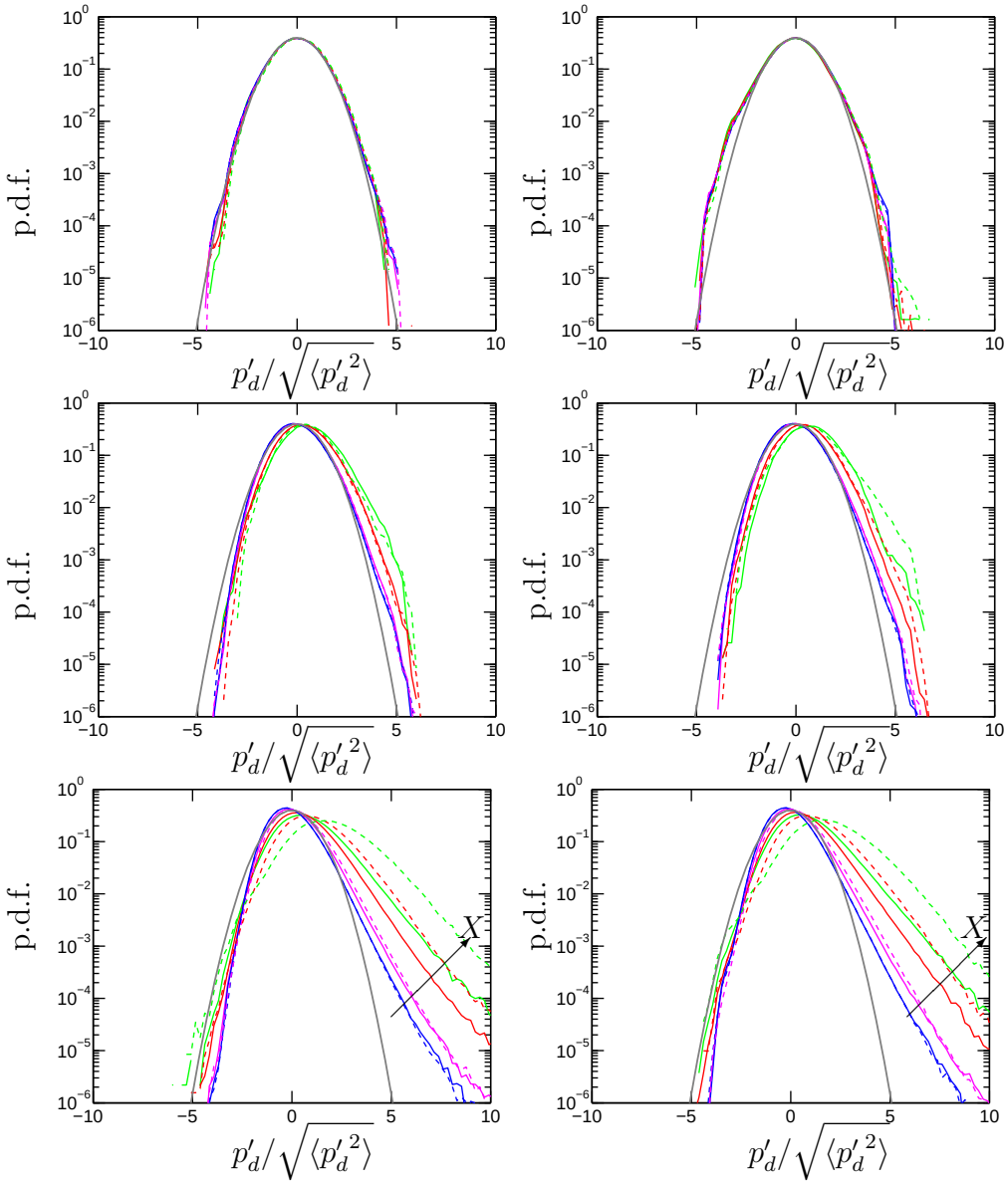

Figure IV.15. Conditional p.d.f. of dilatational pressure given dilatation for different Reynolds and Mach numbers. The left and right panels are at $R_\lambda \approx 100, 160$. The rows from top to bottom are at $M_t \approx 0.1, 0.3, 0.6$ respectively. Arrows indicate increasing magnitude of dilatation. Solid and dashed lines stand for negative and positive dilatation values. $X = \theta/\sqrt{\langle \theta'^2 \rangle}$.

R_λ	M_t	$(-\infty,-5]$	$[-5,-3)$	$[-3,-1)$	$[-1,0)$	$[0,1)$	$[1,3)$	$[3,5)$	$[5,\infty)$
108	0.1	0.00	0.00	0.03	0.46	0.46	0.03	0.00	0.00
106	0.3	0.05	0.04	0.11	0.30	0.31	0.11	0.04	0.04
96	0.6	0.15	0.06	0.12	0.17	0.17	0.12	0.06	0.15
173	0.1	0.01	0.01	0.04	0.45	0.45	0.04	0.01	0.01
163	0.3	0.09	0.05	0.12	0.24	0.24	0.12	0.05	0.09
158	0.6	0.19	0.06	0.11	0.14	0.14	0.11	0.06	0.19

Table IV.3. Ratio of $p'\theta'/\epsilon$ for different R_λ and M_t.

Sreenivasan, 2010*b*). In some of these regions, the magnitude of $p'\theta'$ may overwhelm the contribution of ϵ which is the opposite of the situation of fluctuations close to the mean where $p'\theta'$ is much smaller.

A quantitative way to test this argument is to investigate the ratio, $\alpha = p'\theta'/\epsilon$, and identify their relative magnitudes. A value of α greater (less) than 1.0 would indicate a net energy transfer from internal to kinetic modes (kinetic to internal). The regime where pressure-dilatation dominates the energy transfer can be identified as regions with $|\alpha| \geq 1$. We identify the percentage volume of occurrence of different value of α in eight different bins ranging from -5 to 5 and beyond, as shown in Table IV.3. This would enable us to quantify the fraction of volume of the flow where pressure-dilatation tends to dominate the energy transfer. At low M_t, regardless of the R_λ, α tends to be in the interval $[-1, 1]$ in more than 90% of the domain. Small values of α could be the result of very high dissipation or a negligible pressure-dilatation. As we show at the end of this section, we anticipate the result that the latter is true. This means that the energy transfer is primarily uni-directional for $M_t \approx 0.1$ and governed by dissipation for small dilatational motions. However, as M_t is increased to 0.3, for a large fraction of volume the energy transfer tends to be

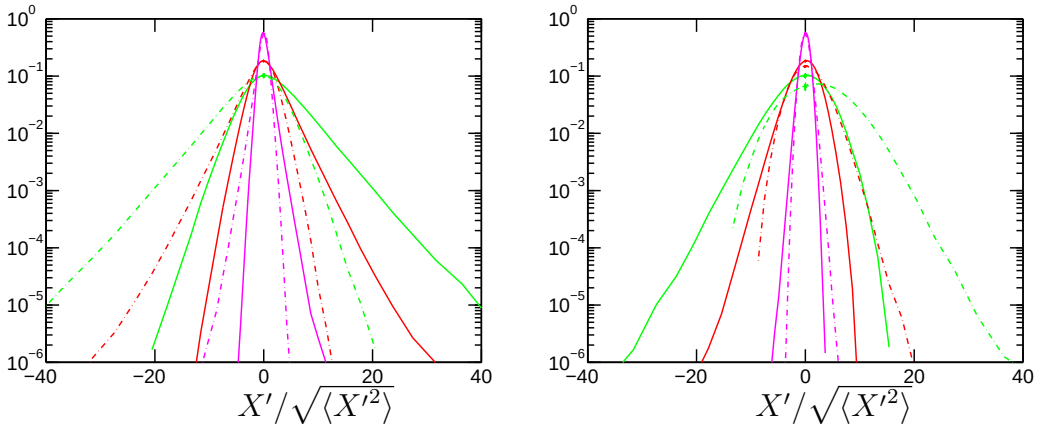

Figure IV.16. Conditional p.d.f. of pressure-dilatation given dilatation for $R_\lambda \approx 160$ and $M_t \approx$ (a) 0.1 and (b) 0.6. X is $p'\theta'$. Colors magenta, green and green are in increasing order of magnitude of dilatation. Solid and dash-dotted lines denote compressions and expansions respectively.

dominated by $p'\theta'$ (regions where $\alpha < -1$ or $\alpha > 1$), which in the case of $R_\lambda \approx 163$ and $M_t \approx 0.3$ is more than 50%. As M_t is further increased to 0.6, very large transfers dominated by pressure-dilatation are very frequent (see, for e.g. $R_\lambda \approx 158$ and $M_t \approx 0.6$ and bins where $\alpha < -5$ or $\alpha > 5$), which is not seen at low M_t. We find that with increasing M_t, the regions where $p'\theta'$ tend to play a dominant role in energy transfer, also increases. Intuitively one may be able to attribute this to regions with strong dilatation of the medium that occurs more frequently as M_t is increased (cf. Table IV.2). This is discussed at the end of this section.

We have also studied the p.d.f. of pressure-dilatation conditioned on dilatation in figure IV.16 to investigate if the above energy transfer process is valid. Knowing that f_p is skewed to the left at low M_t, we could expect the tails of the conditional p.d.f. of f_{pdil} to be wider on the right for compressions ($\theta' \ll 0$, $p' \ll 0$; therefore $p'\theta' \gg 0$) and on the left for expansions, which is also seen in figure IV.16(a). That the tails for the former and latter are similar in shape is, nothing but, a direct

consequence of insensitivity of pressure to the sign of dilatation that we observed in figure IV.13 and an equal likelihood of an occurrence of large compressions and expansions at low Mach numbers (see Table IV.A.4). Following a similar argument at $M_t \approx 0.6$ and recognizing that p' now has a higher probability to be positive when there is a strong dilatation, we can, for instance, say that in regions of strong compressions ($\theta' \ll 0$, $p' \gg 0$), $p'\theta'$ is likely to take a negative value and transfer energy from kinetic to internal energy. This is in agreement with figure IV.16(b) which also supports the argument for strong expansions where $p'\theta'$ is positive and energy transfer is from internal to kinetic energy. While the skewness of f_{pdil} for strong expansions and compressions are almost the same (compare, for instance, *solid* and *dashed* lines with squares) at low M_t, differences appear at high M_t. This is due to the prevalence of strong compressions to expansions by a ratio of about $4:1$ (refer Table IV.A.4).

The wide tails observed in figure IV.16 suggest that $p'\theta'$ is an intermittent quantity: large energy transfers due to pressure-dilatation correlation are typically localized space and occurs infrequently. This has also been noted by Lee *et al.* (1991). The tails tend to be qualitatively in accordance with a log-normal distribution. To consider the Reynolds number variation as well, we compute the p.d.f. (f_{pdil}) in figure IV.17, the tails of which become wider with Reynolds number at low M_t. At $M_t \approx 0.3$, they recede becoming narrower (for $R_\lambda < 275$), just like the p.d.f. of dilatation (refer figure IV.9). For higher M_t, the Reynolds number dependence of the p.d.f. weakens for a wide range of fluctuations (atleast up to 30 times that of the rms fluctuations). In this respect, it seems easier to model the PDF at high M_t

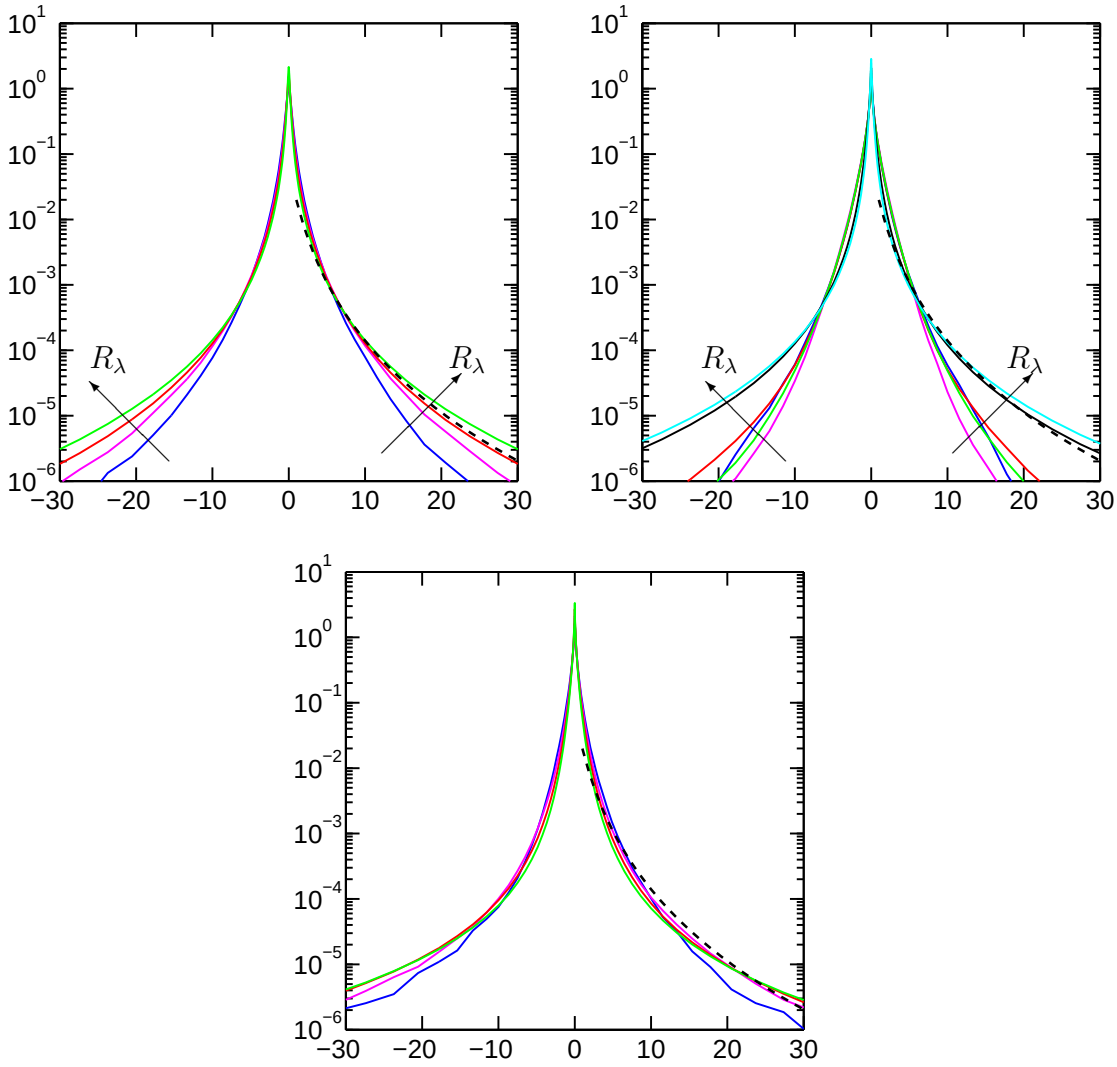

Figure IV.17. p.d.f. of pressure-dilatation normalized by rms at $M_t \approx$ (a) 0.1 (b) 0.3 (c) 0.6. Symbols for different Reynolds numbers Mach numbers as in figure III.2.

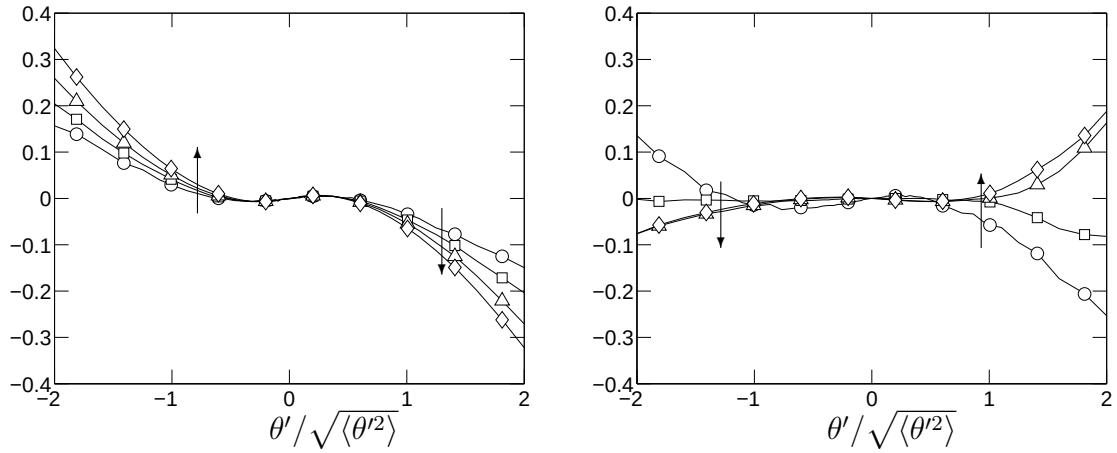

Figure IV.18. Conditional expectation of pressure-dilatation given dilatation for different R_λ at (a) $M_t \approx 0.1$, (b) $M_t \approx 0.6$. Arrows indicate the direction of increasing R_λ.

since Reynolds number effects appear to be the weakest.

As mentioned previously, in order to ascertain how the energy transfer is dominated at different levels of dilatation, we show the conditional expectation of pressure-dilatation for different dilatation levels in figure IV.18. When M_t is small and close to the incompressible limit, the expected value of $p'\theta'$ is seen to increase with R_λ on either side, with a change in sign occurring around zero dilatation. We also observe a narrow range of fluctuations ($-0.5 \ll \theta/\theta' \ll 0.5$) for which the expected value of pressure-dilatation is approximately zero. As M_t is increased to 0.6, in addition to the reduction in expected value of $p'\theta'$ for the same dilatation, there is an extended range of dilatation values ($-1.0 \ll \theta/\theta' \ll 1.0$) where the expected value of $p'\theta'$ is almost independent of R_λ and close to zero. This shows that for small dilatation fluctuations, up to $M_t \approx 0.6$, pressure-dilatation is very small and dissipation dominates the enegy transfer. A plausible reason for this is that at high M_t, pressure responds to changes in the flow slower than at low M_t and hence an increasing range

of fluctuations in dilatation is sustained without significant changes to pressure, and hence pressure-dilatation correlation.

IV.B. Summary

The near-perfect scaling of solenoidal pressure shows that the effect of M_t is insignificant for the wide range of R_λ and M_t investigated. However, there is a marked effect of M_t on dilatational pressure, whose fluctuations tend to be of the same order of magnitude as that of its solenoidal component around $M_t \approx 0.3$. The skewness of the p.d.f. of pressure, which remains negative at low M_t and positive at high M_t, indicates the prevalence of high-pressure regions at high M_t which is different from incompressible turbulence where low pressure regions are commonly observed (and thus the negative skewness of pressure at low M_t). Additionally, the positive fluctuations at low M_t and negative fluctuations at high M_t tend to follow a Gaussian distribution with a very dependence on M_t. By investigating the p.d.f. of the components of pressure, we found that the solenoidal pressure is practically unaffected by the effects of M_t, while the dilatational pressure tends to become positively skewed leading us to conclude that the increasing dominance of dilatational pressure causes the overall positive skewness of pressure. Conditional statistics of pressure given enstrophy revealed a striking difference between incompressible and compressible turbulence. While low pressure and high enstrophy regions are strongly correlated in incompressible turbulence, we find that this correlation is substantially weakened at high M_t, indicating that the primary physical phenomenon causing the high-pressure regions are mainly associated with dilatational motions. Statistics of

pressure conditioned on dilatation showed that regions of high pressure and strong expansions tend to co-exist, and specifically, in these regions, the dilatational pressure is high. In light of the change in skewness of pressure, the dynamics of energy transfer between the internal and kinetic energy modes were also described for strong compressions and expansions. We found that a strong compression at high M_t and an expansion at low M_t is very likely to transfer energy from the kinetic to internal mode. Furthermore, we found the correlation between pressure and dilatation, pressure-dilatation, follows a log-normal distribution for a wide range of fluctuations away from the mean.

CHAPTER V

EFFECTS OF DILATATIONAL FORCING IN COMPRESSIBLE TURBULENCE

In this chapter, we study the effect of different types of external forcing on some basic statistics in stationary compressible turbulence. Since external forcing could trigger either the solenoidal and/or dilatational mode of velocity, we study the effects of forcing both the modes on the scaling of thermodynamic quantities. In realistic situations, it is unclear in principle which modes are being excited, and is thus very important to understand the effect of each on the behavior of turbulence. Only a very limited number of studies with dilatational forcing are available in the literature (Kida & Orszag, 1990; Petersen & Livescu, 2010; Federrath *et al.*, 2009), and hence, our understanding of its behavior is, at best, limited. For example, it is still not known if the standard scaling laws that have been used for solenoidal forcing is applicable when the dilatational component of velocity is excited. For instance, Federrath *et al.* (2009) observed that the energy spectra for solenoidal and dilatational forcing are significantly different and found that the density fluctuations are much stronger when the dilatational mode is forced. This may indicate that a universal behavior, independent of the type of external forcing, in compressible behavior may be far more difficult to achieve.

For a large class of scientific and engineering problems, turbulent Mach number has been used as a measure of compressibility. However, the value of M_t tells very little about the dilatational content in the flow. For this purpose, we developed a

range of database with different levels of forcing for the solenoidal and dilatational mode respectively. This enables us to study the scaling of some basic statistics in compressible flows, and in the process, allows us to investigate if M_t can comprehensively account for the compressibility as well as serve as a possible universal scaling parameter. As we show in this chapter, there can be additional scaling parameters that can also quantify the dilatational content in the flow. Some of these parameters can successfully collapse data regardless of the forcing. While a more rigorous theoretical analysis and various other types of forcing is necessary to conclude, this may suggest that a universal scaling could be present in compressible flows.

While the fluctuations in temperature are very small when the solenoidal mode is forced, we observe that for dilatational forcing, the fluctuations in temperature tend to be significant. Since temperature and viscosity are directly related by the Sutherland's law ($\mu \approx T^{0.5}$), it is possible that the instantaneous variations in viscosity are considerably large, which may or may not permit us to use the assumption that was earlier used for solenoidal forcing, $\langle \mu X \rangle \approx \langle \mu \rangle \langle X \rangle$, for a quantity X. It is thus imperative that while decomposing the variable into solenoidal and dilatational, for instance, dissipation, one has to ensure that its correlation with viscosity is negligibly small.

Due to the definition of M_t as the ratio of fluctuations of velocity to that of the mean speed of sound, an *apriori* estimate of fluctuations or kinetic energy in the dilatational mode is not known. Furthermore, the flow characteristics could be completely different for the same M_t when different modes are excited. For instance, in Table V.1 for $N^3 = 64^3$, for both $s = 1$ and $s = 0.4$ (s represents the amount

of total energy that is used to excite the solenoidal mode and is defined later), we see a comparable Mach number (0.28 and 0.35), while the normalized temperature fluctuations are about two orders of magnitude different. This may ascertain that different parameters that can estimate compressibility levels are needed. While there are many other metrics to gauge the level of compressibility (for example, based on dilatation), a systematic study of how basic statistics scale with these parameters is still lacking. Our study aims to fill this void by proposing two different parameters and studying scaling of some fundamental quantities with these parameters. The two parameters are defined as the (i) ratio of dilatational to total kinetic energy, $\chi = \langle \mathcal{K}^d \rangle / \langle \mathcal{K} \rangle$ (ii) dilatational Mach number, $M_t^d = u^d / \langle c \rangle$, Both the parameters have a direct relevance to relative importance of dilatational content to that of solenoidal or total.

By using, $\langle \mathcal{K} \rangle = \langle \mathcal{K}^s \rangle + \langle \mathcal{K}^d \rangle$, we can express the fraction of kinetic energy that lies in the dilatational component by, $\chi = \langle \mathcal{K}^d \rangle / \left(\langle \mathcal{K}^s \rangle + \langle \mathcal{K}^d \rangle \right)$. While χ has been extensively used in decaying compressible flows (for e.g. see Sarkar *et al.* (1991)) as a measure of initial compressibility, investigations using it as a scaling parameter are scarce. By using a linearized theory, Sarkar *et al.* (1991) obtained the relation, $\chi \sim M_t^2$, for small M_t. As we show in figure V.5, this may not always be true when the dilatational mode is forced. For intermediate values of M_t, the scaling seems to be follow a steeper power law than M_t^2 while for very low M_t, χ seems to be much higher. One plausible reason is that the increase in Mach number is not commensurate with the increase in fraction of dilatational kinetic energy, which is much higher when the dilatational mode is excited (as seen in Table V.1). This

motivates us to explore how basic quantities scale with χ instead of M_t.

Another way of quantifying the fluctuations in dilatational mode is by computing the so-called dilatational Mach number, M_t^d. The definition of this quantity, is loosely based on the definition of *acoustic particle velocity*, which is given as (Howe, 2003),

$$\text{acoustic particle velocity} = \frac{\text{Acoustic pressure}}{\text{mean density x speed of sound}}.$$

Physically, the acoustic particle velocity is the velocity with which the fluid associated with a pressure wave moves back and forth (Howe, 2003). In our case, the acoustic pressure and velocity can be approximated as p'_d and u^d, which then leads to the following relation,

$$\sqrt{\langle u^{d2} \rangle} = \sqrt{\langle {p'_d}^2 \rangle} / \langle \rho \rangle \langle c \rangle . \tag{5.1}$$

If one envisages a $p \sim \rho u^2$ type of relation for the dilatational pressure and velocity, then we could divide both sides in the previous equation by $\langle c \rangle$ leading to, $\sqrt{\langle u^{d2} \rangle} / \langle c \rangle = \sqrt{\langle {p'_d}^2 \rangle} / \langle \rho \rangle \langle c \rangle^2$, which simplifies to $M_t^d = \sqrt{\langle {p'_d}^2 \rangle} / \langle \rho \rangle \langle c \rangle^2$. This can be expressed in terms of the mean temperature, $M_t^d = p'_d / \langle \rho \rangle \gamma R \langle T \rangle$. If one were to assume that the density-temperature correlation can be ignored, the relation simplifies to

$$M_t^d = \sqrt{\langle {p'_d}^2 \rangle} / \gamma \langle P \rangle . \tag{5.2}$$

Hence, M_t^d is a parameter that quantifies the fluctuations in dilatational pressure in the flow and a measure of the dilatational potential energy in the system. It is now possible to show that the approximation of u^d as acoustic particle velocity is consistent with the definition of equipartition function, F, that was discussed is

Ch IV. Squaring Eq. (5.1), and dividing by $\langle u^2 \rangle$, we get,

$$\frac{\left\langle u^{d^2} \right\rangle}{\langle u^2 \rangle} \approx \frac{\left\langle {p'_d}^2 \right\rangle}{\langle p \rangle^2} \frac{\langle p \rangle^2}{\langle u^2 \rangle} \frac{1}{\langle p \rangle^2 \langle c \rangle^2} \tag{5.3}$$

It is now possible to approximate the lhs of Eq. (5.3) to the fraction of dilatation kinetic energy, χ, and then using $\langle p \rangle \approx \langle \rho \rangle R \langle T \rangle$ we get,

$$\chi \approx \frac{\langle p_d^2 \rangle}{\langle p \rangle^2} \frac{\langle \rho \rangle^2 R^2 \langle T \rangle^2}{\langle u^2 \rangle} \frac{1}{\langle \rho \rangle^2 \langle c \rangle^2}. \tag{5.4}$$

Substituting the mean speed of sound, $\langle c \rangle = \gamma R \langle T \rangle$, we obtain,

$$\chi \approx \frac{\langle p_d^2 \rangle}{\langle p \rangle^2} \frac{\langle c \rangle^2}{\gamma^2 \langle u^2 \rangle} \tag{5.5}$$

which eventually leads to the expression for F,

$$F \approx \frac{\chi \gamma^2 M_t^2}{\langle p_d^2 \rangle / \langle p \rangle^2} \approx \frac{\chi M_t^2}{M_t^{d^2}} \tag{5.6}$$

It is important to note that, we have assumed that the acoustic velocity and pressure can be approximated as their respective dilatational components, which may or may not be true. As we will show later, this approximation seems to be valid for a wide range of conditions and for different types of forcing, suggesting that this may indeed serve as a universal scaling parameter. To test this, we have implemented a forcing scheme such that both the modes (solenoidal and dilatational) can be simultaneously forced and is discussed in the next section.

V.A. Dilatational Forcing

The forcing term in Eq. (2.2) is represented as,

$$\boldsymbol{f} = \sum_{|\boldsymbol{k}|<k_f} \left(s \hat{\boldsymbol{f}}_{\perp}(\boldsymbol{k}) + (1-s)\, \hat{\boldsymbol{f}}_{\parallel}(\boldsymbol{k}) \right) e^{-\iota \boldsymbol{k} \cdot \boldsymbol{x}}, \tag{5.7}$$

where $\hat{\boldsymbol{f}}_{\perp}(\boldsymbol{k}) = \boldsymbol{P} \cdot \hat{\boldsymbol{f}}(\boldsymbol{k})$ with $\boldsymbol{P} = \boldsymbol{I} - \boldsymbol{k}\boldsymbol{k}/k^2$, $\hat{\boldsymbol{f}}_{\parallel}(\boldsymbol{k}) = \boldsymbol{k}\boldsymbol{k}/k^2$, and k_f is the number of the forced wavenumbers as mentioned in Ch IV. Here, s is the fraction of energy that is given to the solenoidal mode. The actual input of energy is $\langle \mathbf{f} \cdot \mathbf{u} \rangle$. A purely solenoidal forcing, that was considered in Ch IV, would correspond to $s = 1$, while a purely dilatational forcing would have $s = 0$. A database of simulations at different s, and at different Reynolds and Mach numbers is developed to study the scaling and energy transfer between the internal and kinetic energy modes. The different parameters, R_λ, M_t and the contribution from normalized pressure (p^*), density (ρ^*), temperature (T^*) is included in Table V.1.

Due to the addition of this parameter (s), it is essential to understand how R_λ and M_t vary with s and is thus shown in figure V.1. All the quantities have a similar trend, decreasing until about $s = 0.3$, and showing a small increase for $s > 0.3$. The reduction in $\Delta x/\eta$ is evident due to the decrease in R_λ. However, there is no definitive trend like other forcing parameters (see, for instance, figure II.6) and hence one has to judiciously choose the parameters. In general, a lower $\Delta x/\eta$ is maintained for cases when both the modes are forced ($0 < s < 1$). This is because of the presence of intense compressions and expansions in the flow that needs to be resolved. Hence, the resulting Reynolds number is also considerably smaller than that of the solenoidally forced case.

V.B. Classical Scaling

We revisit some of the classical scaling mentioned in Sec III.B, for both solenoidal and dilatationally forced stationary compressible turbulence. The scaling of dissipa-

N^3	R_λ	M_t	s	χ	M_t^d	$\sqrt{\langle p^{*2}\rangle}$ $\times 100$	$\sqrt{\langle \rho^{*2}\rangle}$ $\times 100$	$\sqrt{\langle T^{*2}\rangle}$ $\times 100$
64^3	39	0.10	1.0	0.000	0.000	0.478	0.374	0.126
64^3	32	0.20	1.0	0.000	0.002	1.957	1.536	0.548
64^3	33	0.28	1.0	0.002	0.008	3.895	2.988	1.104
64^3	38	0.39	1.0	0.011	0.023	8.663	6.522	2.480
64^3	34	0.59	1.0	0.039	0.066	20.227	14.956	5.819
64^3	26	0.35	0.4	0.441	0.132	32.605	22.813	9.238
64^3	35	0.31	0.6	0.088	0.052	12.932	9.273	3.663
64^3	36	0.32	0.9	0.021	0.027	7.666	5.640	2.192
64^3	33	0.58	0.9	0.060	0.082	22.172	16.495	6.521
128^3	63	0.09	1.0	0.000	0.000	0.401	0.316	0.110
128^3	54	0.22	1.0	0.000	0.003	2.181	1.688	0.606
128^3	60	0.29	1.0	0.013	0.019	5.797	4.291	1.643
128^3	65	0.38	1.0	0.024	0.034	9.888	7.279	2.810
128^3	58	0.58	1.0	0.044	0.069	19.959	14.720	5.775
128^3	33	0.06	0.3	0.743	0.030	7.321	5.207	2.072
128^3	39	0.26	0.4	0.416	0.095	24.343	17.135	6.828
128^3	58	0.30	0.6	0.103	0.054	13.283	9.463	3.740
128^3	62	0.32	0.9	0.036	0.034	9.288	6.727	2.641
128^3	53	0.54	0.6	0.097	0.095	23.914	17.179	6.882
256^3	108	0.10	1.0	0.000	0.000	0.441	0.335	0.126
256^3	101	0.20	1.0	0.001	0.003	1.892	1.436	0.543
256^3	106	0.34	1.0	0.010	0.019	6.395	4.753	1.833
256^3	107	0.40	1.0	0.014	0.027	8.859	6.579	2.546
256^3	96	0.57	1.0	0.042	0.067	19.231	14.092	5.580
256^3	77	0.04	0.3	0.762	0.021	6.358	5.245	4.042
256^3	50	0.25	0.3	0.660	0.116	28.329	19.897	8.025
256^3	95	0.28	0.6	0.110	0.052	12.901	9.188	3.625
512^3	173	0.10	1.0	0.000	0.000	0.389	0.300	0.089
512^3	173	0.21	1.0	0.000	0.001	1.850	1.394	0.517
512^3	163	0.31	1.0	0.010	0.018	5.636	4.141	1.629
512^3	167	0.37	1.0	0.016	0.027	8.342	6.129	2.392
512^3	158	0.60	1.0	0.038	0.066	19.185	14.034	5.579
512^3	143	0.24	0.6	0.097	0.043	10.701	7.617	3.024
512^3	75	0.21	0.3	0.652	0.095	23.617	16.653	6.671
1024^3	268	0.33	1.0	0.002	0.008	4.585	3.428	1.351
1024^3	241	0.43	1.0	0.037	0.045	12.430	9.020	3.554
2048^3	430	0.31	1.0	0.001	0.005	3.781	2.812	1.096

Table V.1. Database of solenoidal and dilatational forced simulations

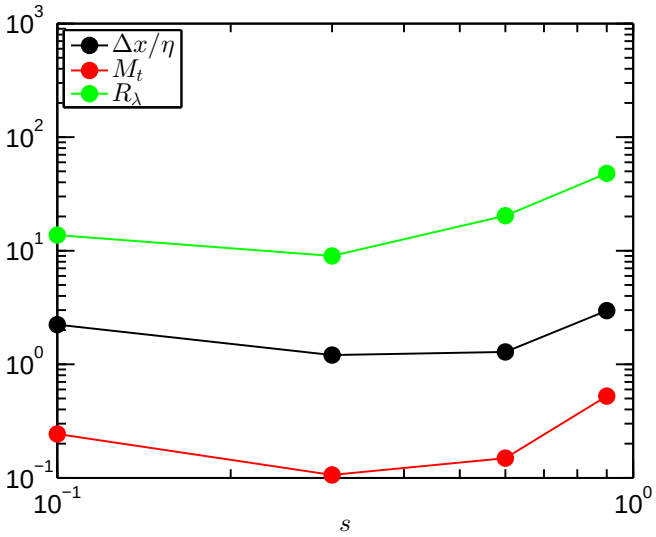

Figure V.1. Variation of R_λ, M_t, and $\Delta x/\eta$ with f_0

tive anomaly is shown in figure V.2. While higher Reynolds number simulations are necessary to state the asymptotic nature of $D = \langle\epsilon\rangle L/u^3$, the data appear to suggest that the deviation from the solenoidal case is minimal when the dilatational mode is forced. While the dissipative anomaly has been related to the dynamics of energy cascade in incompressible turbulence, one has to exercise caution in interpreting this result for compressible turbulence. This may or may not imply the picture of classical scaling, and further efforts are needed in this direction. There is a significant difference in the contribution from D_d when the dilatational mode is excited. For instance, in figure III.1(b) we see that the overall contribution from the D_d is only about 5% when the solenoidal mode is forced (for $M_t \approx 0.6$). But, exciting the dilatational mode enhances the dilatational kinetic energy, in which case, the contribution from D_d is dominant and can extend to about $60-90\%$ of D. This shows that the role of dilatational components are particularly prominent when the dilatational mode is excited and warrants a more thorough investigation. It is also interesting to

note that even when the contribution from D_d is so high, the overall behaviour of D tends to similar to that of incompressible turbulence. Since, D tends to asymptote to a constant regardless of the type of forcing, it is now natural to investigate how the characteristic length scales depend on the type of forcing and if they do exhibit some kind of universality. The scaling of non-dimensionalized Taylor micro-scales and integral length scale are shown in figure V.3. We see that there is considerable deviation in the integral length scale when the dilatational mode is forced and is slightly higher than when the solenoidal mode is forced. Thus, it seems that a Reynolds number dependence may appear when the dilatational mode is forced. For the same Reynolds number, the length scales are slightly larger than when the mode is forced. It is possible that since the dilatational mode is forced, the flow tends to exhibit wavy behavior which may introduce long-range spatial correlations leading to the increased integral length scales. However, if one were to study the scaling in the so-called inertial range, it may be appropriate to investigate the scaling of Taylor microscales, and is also shown in figure V.3(a) (cf. square symbols). The classical Kolmogorov scaling, as discussed in Ch III, for Taylor scales is given by $\lambda/\eta \sim R_\lambda^{1/2}$ and is indicated in the figure. We see that even when the dilatational mode is forced, the scaling of Taylor scales show very little dependence on M_t or the type of forcing. This result shows that the classical scaling laws proposed by Kolmogorov (Kolmogorov, 1941), tend to be valid even in compressible flows with significant dilatational content. Similarly, the scaling of the velocity scales is only weakly modified for the range of M_t and s investigated. However, high R_λ cases with dilatational forcing are necessary to unequivocally state the universality of these

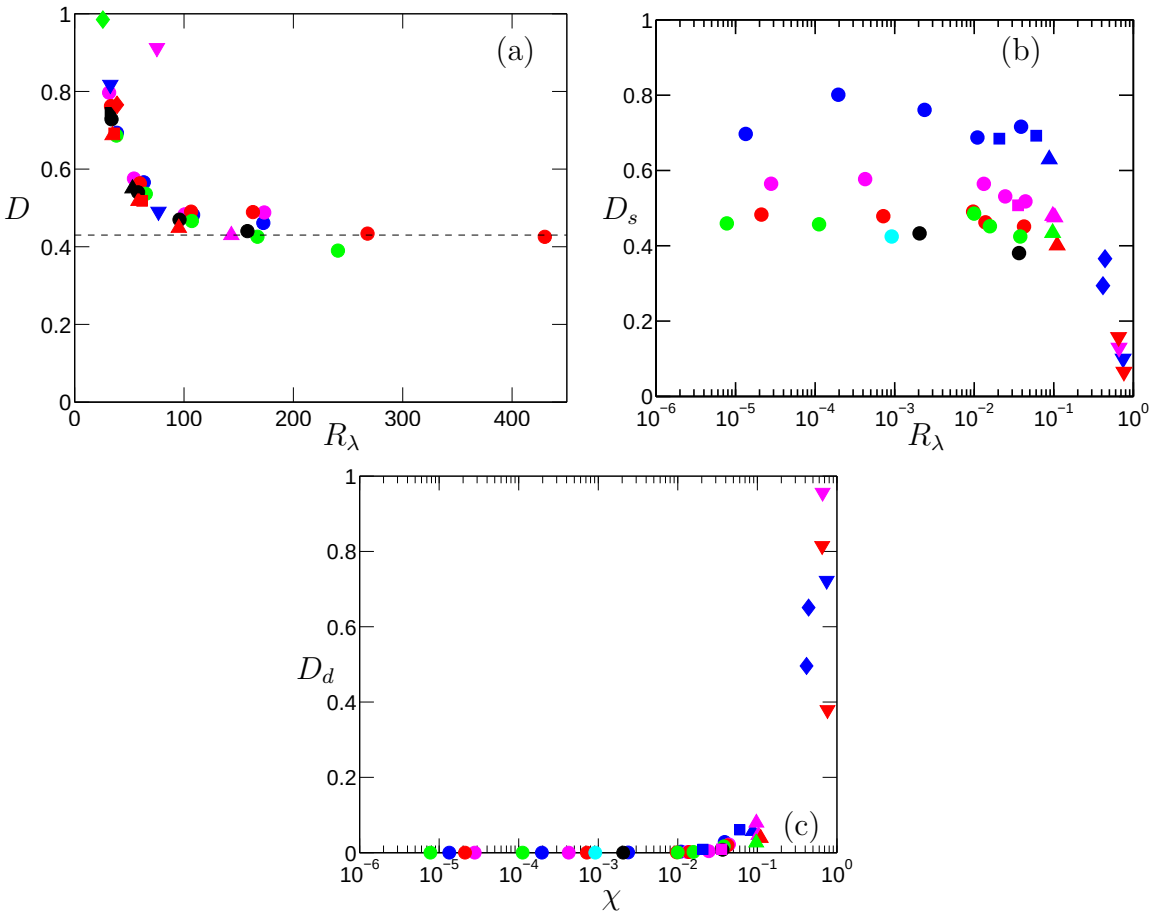

Figure V.2. (a) Normalized mean energy dissipation ratio (D) and its (b) solenoidal component (D_s), (c) dilatational component (D_d) at different R_λ, M_t and s. The dashed line in (a) represents $D = 0.43$. Symbols correspond to $s = 1.0\,(\bigcirc)$, $0.9\,(\square)$, $0.6\,(\triangle)$, $0.4\,(\Diamond)$, $0.3\,(\triangledown)$, and $0.0\,(\triangleleft)$. Colors correspond to $M_t \approx 0.1$ (blue), 0.2 (magenta), 0.3 (red), 0.4 (green) and 0.6 (black).

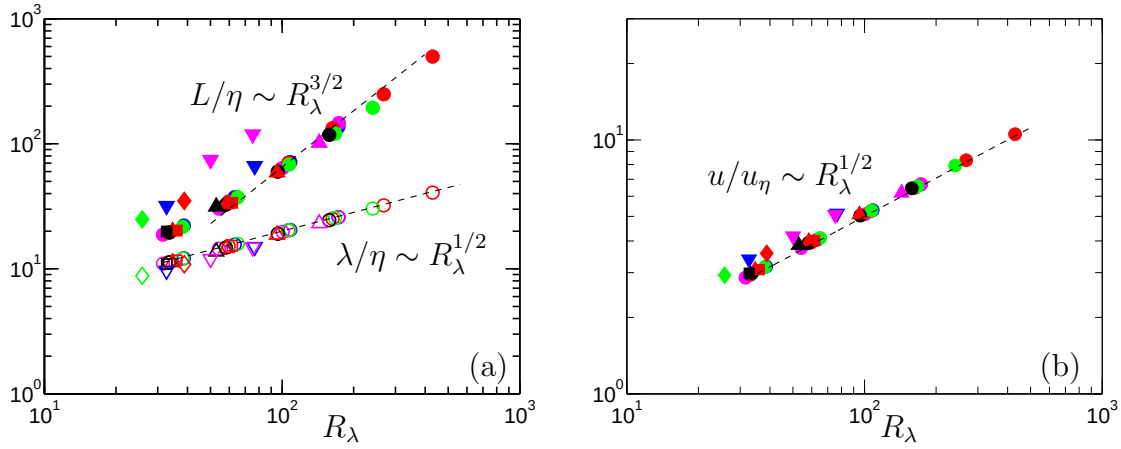

Figure V.3. Scaling of (a) Taylor micro scale, λ (open symbols) and integral length scale, L (solid symbols) and (b) Kolmogorov velocity scale (u_η). Dashed lines indicate classical Kolmogorov scaling for incompressible turbulence: $\lambda/\eta \sim R_\lambda^{1/2}$, $L/\eta \sim R_\lambda^{3/2}$, $u/u_\eta \sim R_\lambda^{1/2}$. Different colors stand for different M_t and symbols stand for s according to figure V.2.

scaling relations.

V.B.1. Equipartition of Energy

Though equipartition of energy was originally proposed for decaying compressible by Sarkar *et al.* (1991), we have shown for different R_λ and high M_t that the equipartition function F is close to one for a purely solenoidal forcing (see Sec III.C). However, this balance between the dilatational kinetic energy and potential energy may also depend on how the external forcing behaves. For instance, it is still largely unknown if this energy balances holds good when the dilatational mode is excited. We thus plot F in figure V.4, against χ for different s. We see that for large χ, which are usually a consequence of forcing the dilatational mode (refer Table V.1), F is very close to one. The larger deviations from $F = 1$ are when the fraction of dilatational kinetic energy is very small, which tends be very similar to incompressible flows when

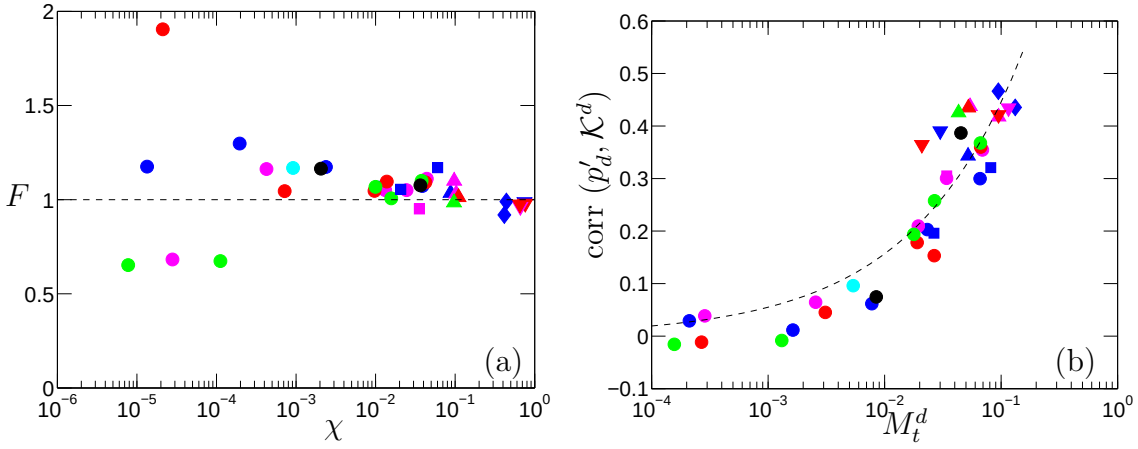

Figure V.4. (a) Variation of equipartition function F with χ, and (b) correlation between p'_d and $\mathcal{K}^d$ with M_t^d. The dashed lines in (a) denotes $F = 1$ and in (b) denotes a power-law best fit of $1.27 M_t^{d\,0.45}$. Symbols and colors for different s and M_t respectively are according to figure V.2.

the energy in dilatational pressure (or equivalently the potential energy) is negligibly small. It is thus possible that even in stationary compressible flows, regardless of the type of forcing, equipartition of energy may be valid. If equipartition is applied on an instantaneous basis, we would expect p'_d and $\mathcal{K}^d$ to be correlated. As shown in figure V.4(b), the correlation between them increases in magnitude as the dilatational Mach number increases, and if one were to use a power-law fit, $1.27 M_t^{d\,0.45}$ conforms with the data well. We see that at higher M_t^d, the correlation between them is much higher and so is the tendency for F to be close to one, implying that there could be both local and global equipartition.

A consequence of equipartition is the scaling $\chi \approx M_t^2$ which results due to ${p'_d}^2/\langle p \rangle^2 \approx M_t^2$ (Sarkar *et al.*, 1991). However, we see in figure V.5 that this may not always be true when the dilatational mode is forced, and χ seems to grow much faster than M_t when the forcing is not solenoidal. We observe that though the dilatational

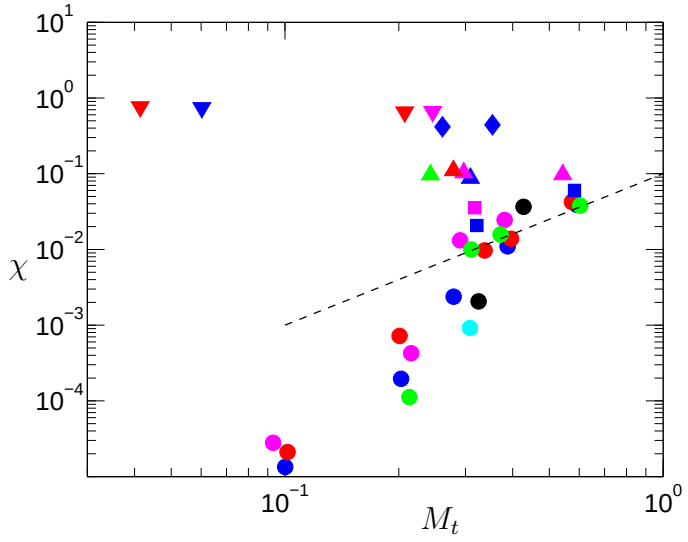

Figure V.5. Variation of χ with M_t for both solenoidal and dilatational forcing. The dashed lines represent a slope of 2. Symbols and colors for different s and M_t respectively are according to figure V.2.

kinetic energy is quite high, the resulting Mach number is small and hence M_t may not completely describe the dilatational content in the flow. Since the behavior of pressure is crucial in equipartition, we investigate the behavior and scaling of pressure for both solenoidal and dilatational forcing in the next section.

V.C. Statistics of Pressure

Since pressure is related to density and temperature by the equation of state ($p = \rho RT$), we could obtain the mean pressure by using the Reynolds decomposition as (Donzis & Jagannathan, 2013*a*),

$$\langle p \rangle = R\left[\langle \rho \rangle \langle T \rangle + \langle \rho' T' \rangle\right]. \tag{5.8}$$

As we found earlier in Ch IV, the density-temperature correlation tends to be important only at high M_t, and hence mean pressure could be appropriated as,

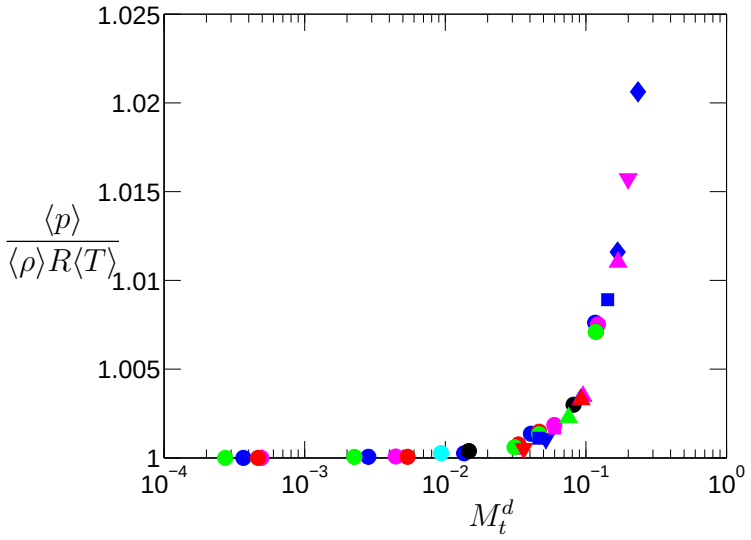

Figure V.6. Variation of mean pressure normalized by mean density and temperature versus M_t^d. Symbols and colors for different s and M_t respectively are according to figure V.2.

$\langle p \rangle = R\langle \rho \rangle \langle T \rangle$. However, when the dilatational mode is forced, we could have strong fluctuations in temperature, and thus it is important to quantify the deviation from this approximation regardless of the type of forcing. For this purpose, we plot in figure V.6 the non-dimensionalized mean pressure versus M_t^d from our database. While the contribution from density- temperature correlation is negligibly small at low M_t^d, we observe a steep rise beyond $M_t^d \approx 0.03$. For small M_t^d, this plot is consistent with our earlier observations and the correlation tends to be very small (see Ch IV) regardless of the type of forcing. Even though the deviation seems small for the range of M_t^d investigated it is important to note that the qualitative manner of variation is similar for both the types of forcing considered. This may indicate that M_t^d as a possible universal scaling parameter. While it is essential to quantify departures from the mean, it is also of importance to analyze how the fluctuations of pressure behave and scale depending on the type of forcing, which is done next.

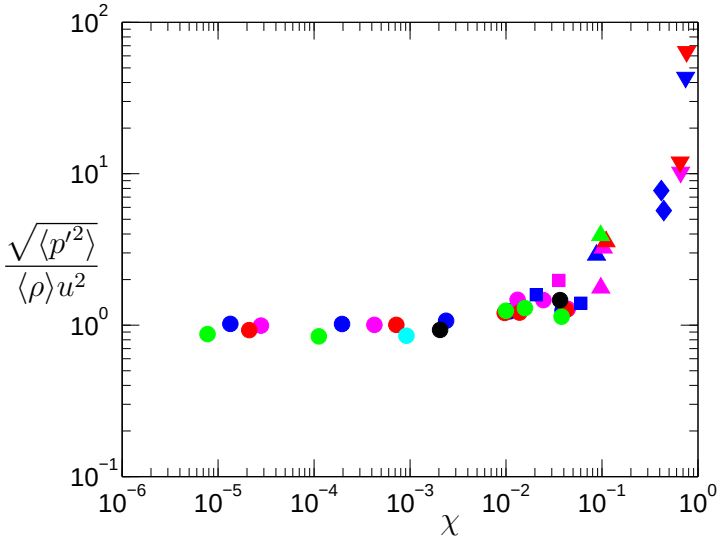

Figure V.7. Scaling of $\sqrt{\langle p'^2 \rangle}/\langle \rho \rangle u^2$ versus χ. Symbols and colors for different s and M_t respectively are according to figure V.2.

Since we are investigating a range of M_t^d and χ, it may be of importance to study the threshold below which pressure tends to obey according to incompressible scaling laws. For instance, it has been found in incompressible turbulence that $p \approx \langle \rho \rangle u^2$ (Donzis *et al.*, 2012). We plot the r.m.s of pressure fluctuations normalized by $\langle \rho \rangle u^2$ in figure V.7. When the solenoidal mode is forced and M_t is really small, we see that the fraction of kinetic energy that lies in the dilatational component (χ) is very small. However, for purely solenoidal forcing at higher M_t, or when the dilatational mode is forced, there are deviations from the proposed scaling. Specifically, for dilatationally forced cases, we see that this scaling may be completely off for a wide range of χ. It seems that $\chi \approx 0.01$ is a threshold below which this scaling relation remains valid. While more simulations of solenoidal forcing cases at high M_t (and thus high χ) are necessary it is conceivable that two different scaling regimes may exist for solenoidal and dilatational forcing, with the former having only minor departures

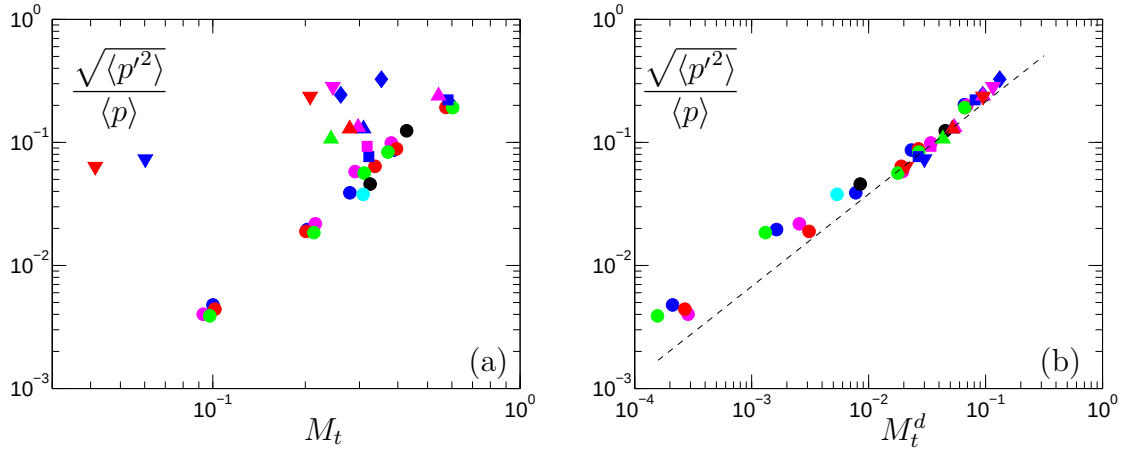

Figure V.8. Scaling of $\sqrt{\langle p'^2 \rangle}/\langle p \rangle$ versus (a) M_t (b) M_t^d (dashed lines indicate a slope of 0.75. Symbols and colors for different s and M_t respectively are according to figure V.2.

from the proposed scaling (cf. circles in figure V.7), and the latter show significant departures.

Similarly, the overall pressure fluctuations could be normalized by the mean pressure which could be shown to scale as M_t^2 (Donzis & Jagannathan, 2013a). However, minor departures were found and the scaling exponent was also to 2.2 for solenoidal forcing (Donzis & Jagannathan, 2013a). It is still not known if this relation is valid when the dilatational mode is forced or if other parameters control the process. We thus plot the normalized pressure fluctuations versus both M_t and M_t^d in figure V.8 to study their scaling relations. While the scaling with M_t for solenoidal forcing goes as a power law, there is significant deviation when the dilatational mode is forced. This may possibly indicate that scaling parameters other than M_t are required for this particular relation. However, we see a very good collapse of all the data, especially at high M_t^d, when we consider M_t^d as the scaling parameter. Assuming a qualitative power-law behavior for this, we see that $M_t^{d^{0.75}}$ fits the data

very well. While a more rigorous analysis is required, this further reports the claim that M_t^d could serve as universal scaling parameter for compressible flows.

Irrespective of the type of external forcing, pressure could be decomposed into solenoidal and dilatational components as mentioned in Ch III. Here, we study the scaling of the individual components of pressure. Additionally, studying the scaling relations can help identify departures from the proposed scalings, and also help in classifying the regimes under which the approximations are valid. One such approximation that was made earlier in this chapter is in the parameter M_t^d. In figure V.9, we show r.m.s. fluctuations of solenoidal and dilatational pressure normalized by mean pressure versus M_t^d in for both types of forcing. While for solenoidal forcing, $\sqrt{\langle {p'_s}^2 \rangle}$ scales with M_t^d as a power-law, the dilatationally forced cases do not conform to the scaling. This suggests that solenoidal pressure retains some dependency on the nature of forcing. However, we find that p'_d scales very well with M_t^d with a slope of 1, which is in excellent agreement with our predicted scaling earlier in this section (see e.g. Eq. (5.2)). This may possibly indicate that acoustic pressure and velocity can be well represented by their respective dilatational components. Furthermore, this may indicate that the parameter M_t^d could serve as a universal scaling parameter in compressible flows, regardless of the nature of forcing.

We also ascertained the scaling of $\sqrt{\langle {p'_s}^2 \rangle}$ from an incompressible type relation, $p'_s \sim \rho {u^s}^2$ in Sec IV.A. The results when the dilatational mode is forced are shown in figure V.10. The overall scaling seems to be only slightly dependent on R_λ, and shows an excellent collapse with very little effect of the type of forcing. This is particularly useful in turbulence modeling, since this shows that the solenoidal pressure can be

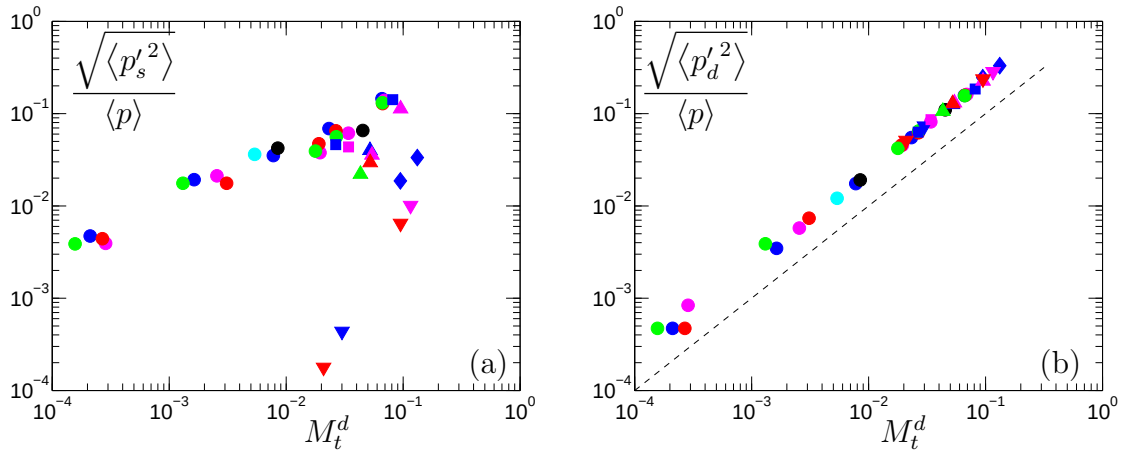

Figure V.9. Scaling of solenoidal and dilatational pressure fluctuations normalized by the mean pressure. Dashed line in (b) indicates a slope of 1. Symbols and colors for different s and M_t respectively are according to figure V.2.

modeled using the standard incompressible scaling laws and only the dilatational pressure requires special treatment. For the latter, we found that M_t^d serves as a good universal scaling parameter. However, $\sqrt{\langle p_s'^2 \rangle}$ and $\sqrt{\langle p_d'^2 \rangle}$ are correlated to a reasonable degree, as we have seen in figure IV.2, which increases with M_t. In figure V.11, we replot the data along with the dilatational cases using M_t^d as a scaling parameter. We see that the correlation is fairly unaffected by the type of forcing as long as the M_t^d remains approximately same. If one assumes a power law in M_t^d for this correlation, we find that $-0.98 M_t^{d\,0.81}$ is consistent with the data. This indicates that at higher M_t^d, the correlation between the respective components of pressure tend to be more and more negative. Thus if the solenoidal pressure remains skewed to the left, we could expect dilatational pressure to become skewed to the right with increasing M_t^d. In order to find the relative importance of solenoidal and dilatational pressure, we plot the ratio of their respective r.m.s values in figure V.12.

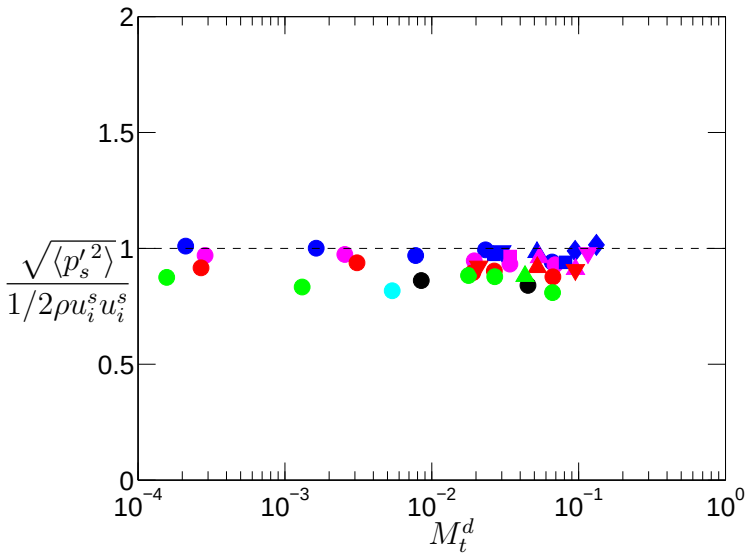

Figure V.10. Scaling of normalized solenoidal pressure, $\sqrt{\langle p_s'^2 \rangle}/\langle 1/2\rho u_i^s u_i^s \rangle$, with M_t^d. Symbols and colors for different s and M_t respectively are according to figure V.2.

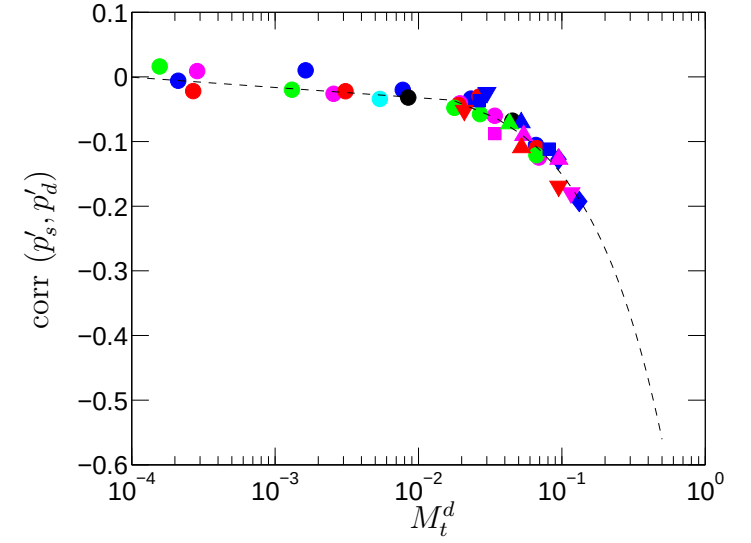

Figure V.11. Correlation between (a) solenoidal and dilatational pressure. Dashed line represents the best-fit power law, -0.98 $M_t^{d^{0.81}}$. Symbols and colors for different s and M_t respectively are according to figure V.2.

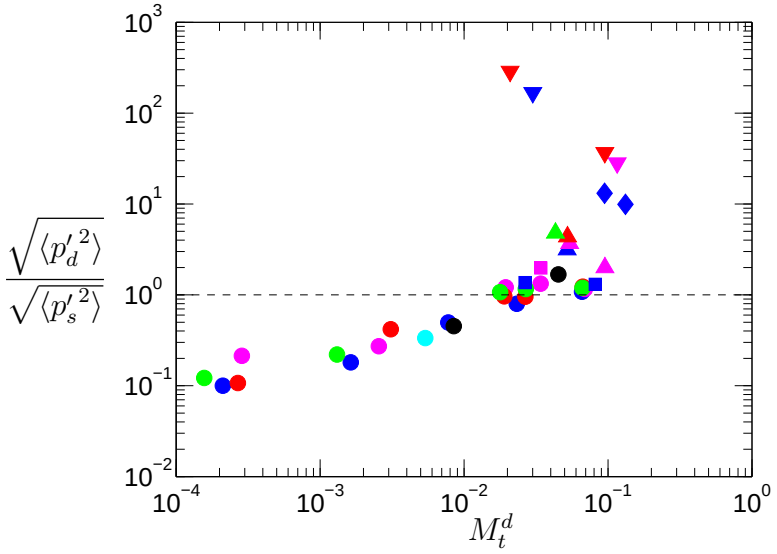

Figure V.12. Ratio of r.m.s of p'_d and p'_s versus M_t^d. Dashed line indicates when the ratio is one. Symbols and colors for different s and M_t respectively are according to figure V.2.

For very low M_t^d, the ratio of p'_d and p'_s is much lesser than one, indicating that the overall contribution of dilatational pressure is small ($< 10\%$). However, beyond a threshold of $M_t^d \approx 0.01$, we find that the ratio tends to increase steeply for both solenoidal and dilatational forcing. This is consistent with figure IV.2 where we observed that beyond $M_t \approx 0.3$, the ratio is greater than one. It is possible that both these thresholds may correspond to each other with the latter tending to be more universal and independent of the type of scaling. Beyond $M_t^d \approx 0.03$, p'_d tends to overwhelm the contribution of the solenoidal pressure by a large magnitude. For example, at $M_t^d \approx 0.1$, p'_d is about an order of magnitude more than that of p'_s.

V.C.1. p.d.f. of Pressure

A more comprehensive information of the behavior of fluctuations of pressure is obtained by studying its p.d.f. , which as we found in Ch IV remains negatively

skewed at low M_t, and becomes positively skewed at high M_t. However, since we found that the magnitude of dilatational pressure is much higher when the dilatational mode is forced, it may also have an effect on the overall behavior of pressure. The p.d.f. of normalized pressure and its solenoidal and dilatational components are shown in figure V.13. While $M_t \approx 0.3$ is found to be the transition regime for the change in skewness of pressure when a purely solenoidal forcing is enforced (see figure IV.4 in Ch IV), we find that this transition happens a much smaller M_t, when the dilatational mode is forced, but at a higher χ. It is also interesting to note that solenoidal pressure remains negatively skewed regardless of the type of forcing, and the dilatational pressure, whose r.m.s is much higher than its solenoidal counterpart for dilatational forcing, tends to be positively skewed. This is in accordance with our previous results where we found that the much higher contribution from dilatational pressure, affects the overall characteristics of pressure. It is now conceivable that the transition regime we observed at $M_t \approx 0.3$ can be expressed in terms of χ, which would then be independent of the type of forcing. If such a range exists, then it would provide strong evidence for the existence of some form of universality in compressible turbulence. As a first step, we study it by quantifying the skewness of p.d.f. of pressure.

The skewness of pressure is plotted in figure V.14 versus both M_t and χ and for different types of forcing. Similar to figure V.8, there is considerable scatter in the skewness, S_p, when the dilatational mode is forced. A plausible reason for this, is that even though the dilatational kinetic energy is large the resulting M_t is much smaller when the dilatational mode is excited. The scaling of S_p against

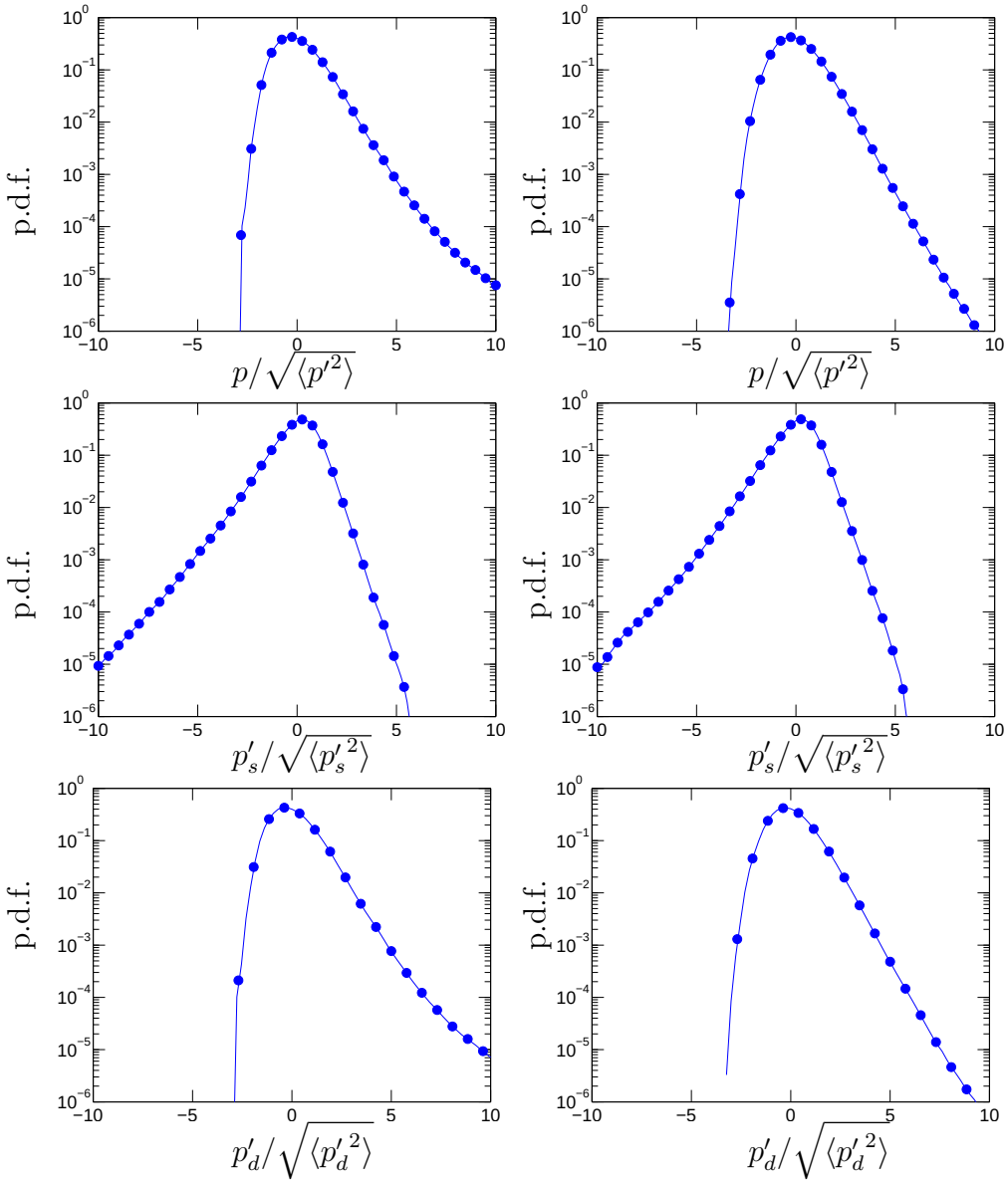

Figure V.13. p.d.f. of (a) $p/\sqrt{\langle p'^2\rangle}$ (b) $p'_s/\sqrt{\langle p'^2_s\rangle}$ (c) $p'_d/\sqrt{\langle p'^2_d\rangle}$ with dilatational forcing for $M_t \approx 0.2$ - Left panel: $s = 0.6$, $R_\lambda \approx 143$, $\chi \approx 0.01$ and, Right panel: $s = 0.3$, $R_\lambda \approx 75$, $\chi \approx 0.65$

χ shown in figure V.14 is seen to provide an excellent collapse of all the cases in our database. Qualitatively we can identify two different regimes, one when χ and S_p is very small similar to that of a low M_t compressible flow/incompressible flow, and a transition regime around $\chi \approx 0.01$ and until $\chi \approx 0.7$, where we see a log-linear variation of skewness with χ ($S_p \sim \log \chi$). When χ is small, it is expected that compressible turbulence possess characteristics similar to that its incompressible counterpart (Donzis & Jagannathan, 2013*a*). We see that for small χ, the skewness is negative and close to -1, which is very similar to that is observed in incompressible turbulence (see e.g. Pumir (1994)). It is also interesting to note that the high M_t cases with solenoidal forcing are seen to produce $\chi > 0.01$ which collapses with dilatationally forced cases at different M_t. The transition at $\chi \approx 0.01$ may be more general and independent of type of forcing. The most important observation, however, is the seemingly universal behavior of the skewness of pressure regardless of the type of forcing. Furthermore, we see that both χ and M_t^d can serve as scaling parameters for both the types of forcing.

In figure V.15, we show the skewness of solenoidal and dilatation pressure respectively. We see that, for the range of M_t^d investigated, the skewness of solenoidal pressure remains fairly unaffected indicating that this decomposition of pressure may be appropriate to delineate the incompressible and compressible components separately. Similar to what we observed in figure V.13, the skewness of pressure at large M_t^d tends to be dominated by dilatational pressure. Thus, regardless of the type of mode of external excitement, we observe a strong presence of high-pressure regions in flows with strong dilatational content. Since, we earlier found that high-pressure

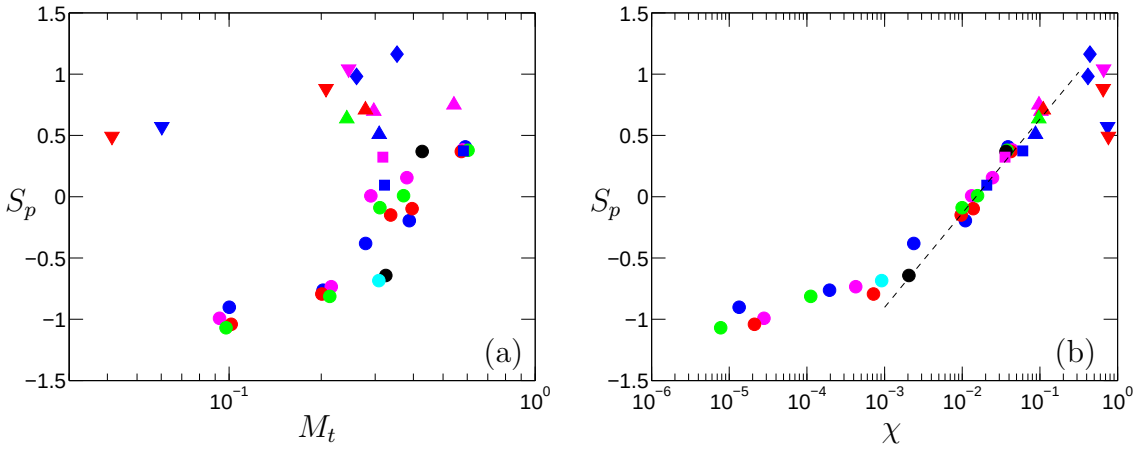

Figure V.14. Skewness of pressure versus (a) M_t (b) χ. The dashed line in (b) is $(\log\chi)/3+1.4$. Symbols and colors for different s and M_t respectively are according to figure V.2.

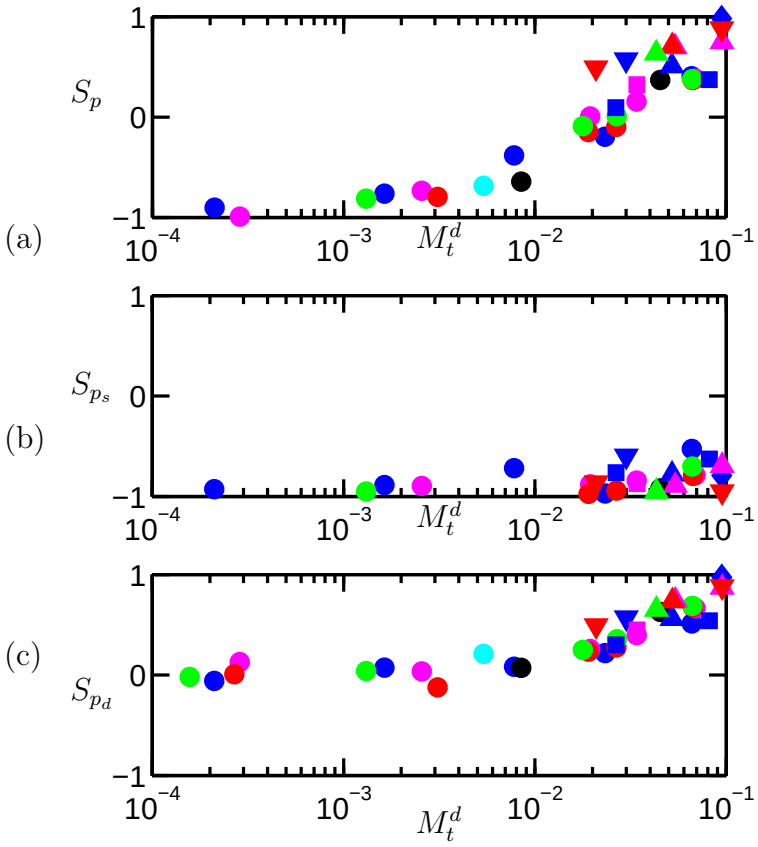

Figure V.15. Skewness of (a) pressure, (b) solenoidal pressure, and (c) dilatational pressure versus M_t^d for different types of forcing. Symbols and colors for different s and M_t respectively are according to figure V.2.

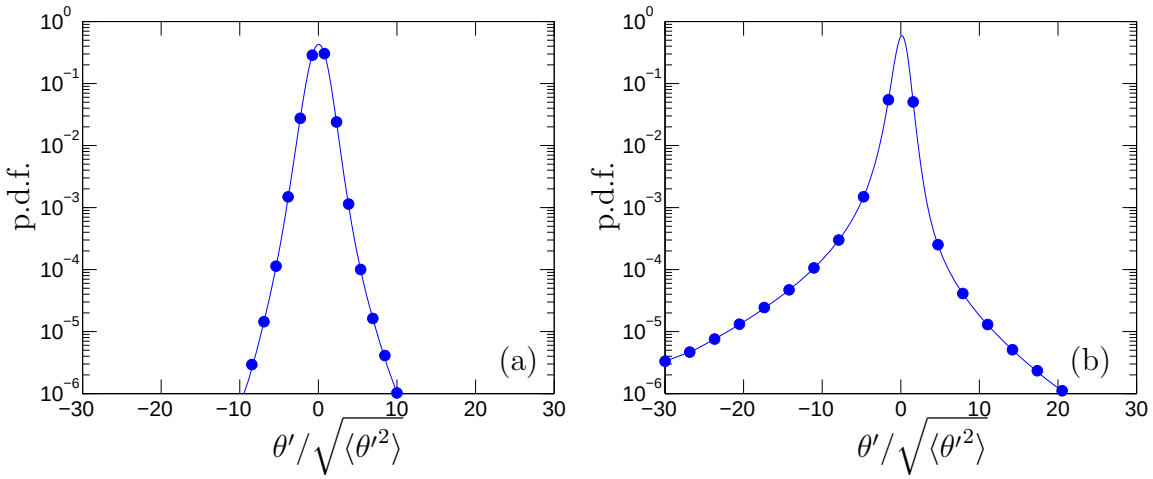

Figure V.16. p.d.f. of dilatation- Left panel: $s = 1.0$, $R_\lambda \approx 100$, $\chi \approx 0.01$ **and, Right panel:** $s = 0.3$, $R_\lambda \approx 75$, $\chi \approx 0.65$

tend to be correlated with expansions, we study if this is still true for different types of forcing.

V.C.2. p.d.f. of Dilatation

In Sec IV.A.4, we found that for a purely solenoidal forcing, the p.d.f. of dilatation is symmetric at low M_t, and at high M_t, the p.d.f. becomes negatively skewed. However, when the dilatational mode is excited we see that this symmetry at low M_t is affected, and the p.d.f. tends to be negatively skewed. In figure V.16, we show the p.d.f. of dilatation for different χ, where the negative skewness is evident only for $\chi > 0.01$, similar to that observed in figure V.15. For smaller χ, the p.d.f. still maintains the symmetry and hence a skewness close to zero. Again, $\chi \approx 0.01$ may be a similar threshold as $M_t \approx 0.3$, but possibly far more universal. The negative skewness indicates the presence of the so-called shocklets or regions of intense compressions which could significantly affect the dynamics of energy transfer, specifi-

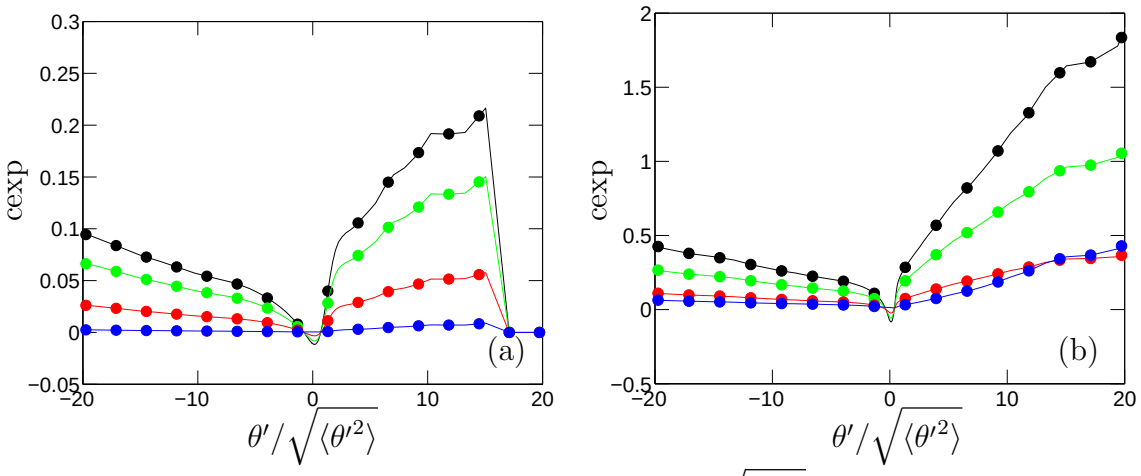

Figure V.17. Conditional expectation $\langle X|\theta'/\sqrt{\langle\theta'^2\rangle}\rangle$ given dilatation with $X = p'/\langle\rho\rangle R\langle T\rangle$ (black), $X = \rho'/\langle\rho\rangle$ (green), $X = T'/\langle T\rangle$ (red), $X = \rho'T'/\langle\rho\rangle\langle T\rangle$ (blue). The parameters on the left plot: $M_t \approx 0.04$, $M_t^d \approx 0.02$, $\chi \approx 0.76$ and right plot: $M_t \approx 0.25$, $M_t^d \approx 0.11$, $\chi \approx 0.66$. s is set to 0.3 for both the cases.

cally through the pressure-dilatation term, which could be either positive or negative. These shocklets and expansions can thus affect the flow statistics.

We are particularly interested in relative contributions of fluctuations of density, temperature and their correlation from Eq. (4.1). We earlier noted that for solenoidal forcing, at high M_t expansions and high-pressure regions tend to co-exist. However, when the dilatational mode is excited, high-pressure regions and expansions seem to co-exist even at a lower M_t as seen in figure V.17(a) where $M_t \approx 0.04$. Though the M_t is small, the dilatational kinetic energy ($\mathcal{K}^d$), which we believe may well-describe this transition regardless of the type of external forcing, is high ($\chi \approx 0.762$). Since the M_t^d is very low for figure V.17(a), we see that the contribution of density-temperature correlation is practically insignificant, however for figure V.17(b) where M_t^d is higher than the threshold of $M_t^d \approx 0.03$ that we observed in figure V.12, its contribution is almost same as that of temperature fluctuations.

V.D. Summary and Discussion

In this chapter, we studied the effect of forcing the dilatational modes of velocity with an emphasis on scaling of thermodynamic quantities. In order to quantify the dilatational content in the flow, we proposed two parameters, the dilatational Mach number (M_t^d) and the fraction of kinetic energy (χ) which are related to M_t by the relation $\chi M_t^2 \approx M_t^d$, if one assumes correlation of density and velocity to be weak. For M_t^d, we showed that it is directly proportional to the dilatational pressure fluctuations if one assumes the acoustic particle velocity and acoustic pressure to be same as the dilatational velocity and pressure. Thus M_t^d represents the amount of dilatational potential energy in the flow, while χ, by definition, quantities the amount of dilatational kinetic energy. While classical scaling of length and velocity scales and dissipative anomaly showed minimal dependence on the type of forcing and thus maintained a possible universal behavior, scaling of thermodynamic quantities showed significant difference when scaled with M_t. The r.m.s fluctuations of pressure, density and temperature is seen to qualitatively scale as ${M_t^d}^{3/4}$ regardless of the type of forcing, indicating that M_t^d could possibly serve as a universal scaling parameter. In addition to the correlation of solenoidal and dilatational pressure which varies as $-0.98{M_t^d}^{0.81}$, we studied the relative magnitude of their fluctuations and found that beyond $M_t^d \approx 0.03$, the magnitude of the latter overwhelms that of the former. The p.d.f. of pressure, which tends to be positively skewed for $M_t \approx 0.3$ for solenoidal forcing, becomes positively skewed beyond $\chi \approx 0.01$ irrespective of the type of the forcing which can be attributed to the dilatational pressure which also becomes positively skewed beyond $\chi \approx 0.01$. The thresholds $M_t \approx 0.3$, $M_t^d \approx 0.03$ and

$\chi \approx 0.01$ for the effects of compressiblity to affect the statistics, are seen to be in good agreement with the approximate relation $\chi M_t^2 \approx M_t^d$, and we see that the latter two relations tend to be more universal than $M_t \approx 0.3$. The skewness of pressure, S_p, is also seen to scale with χ and possess two scaling regimes with the transition occurring around $\chi \approx 0.01$, beyond which we see a possible universal behavior where S_p varies as $\log \chi$. This leads us to believe that regardless of the type of forcing, there is a minimum χ (or M_t^d, M_t) beyond which effects of compressibility affect the statistics profoundly.

CHAPTER VI

CONCLUSIONS AND FUTURE WORK

VI.A. Conclusion

In this work, we studied the Reynolds and Mach number scaling of stationary isotropic compressible turbulence using massively parallel Direct Numerical Simulations (DNS). This was accomplished by developing a highly scalable code that solves the three dimensional compressible Navier-Stokes equations. The code, which is capable of simulating flows with periodic and non-periodic boundaries, also supports sixth and tenth order accurate compact finite difference schemes on both uniform and non-uniform grids. Additionally, the domain decomposition can be one, two or three dimensional. The code has shown sustained scaling for two-dimensional domain decomposition up-to $262,144$ cores on several supercomputing architectures. Multiple levels of parallelism based on distributed message passing interface (MPI) and shared-memory paradigms (OpenMP) decreased the time spent in communication by up-to 40% at large core counts. A simple performance model that predicts the optimal processor grid configuration was also proposed.

The code has been used to generate a large database of homogeneous isotropic turbulence in a stationary state created by forcing the largest scales in the flow at world-record resolutions of 2048^3. A large-scale stochastic forcing scheme that is capable of forcing both the solenoidal and dilatational modes has been developed to attain a statistically stationary state by keeping the mean internal energy constant.

The database, which comprises data at a range of Reynolds number (R_λ) of 38 to 450 and turbulent Mach number (M_t) from 0.1 to 0.6, is used to investigate the effect of compressibility on classical scaling relations, to identify the role of thermodynamic fluctuations, and to investigate the energy exchanges between the internal and kinetic modes of energy for different types of forcing (solenoidal and dilatational).

For solenoidal forcing, the effect of compressibility on low order quantities like length and velocity scales, and energy spectra is seen to be weak. However, quantities such as mean dilatational dissipation rate and Taylor scales exhibit a power-law dependence on M_t when normalized by their corresponding solenoidal counterparts. The Reynolds number dependence is however seen to be weak. At high M_t, there is an equipartition of energy between the dilatational kinetic and potential energies (due to pressure). This is, however, not the case at low M_t in contrast to the theoretical predictions based on linear assumptions. The probability distribution function (p.d.f.) of pressure is negatively skewed at low M_t consistent with incompressible turbulence, but becomes positively skewed at high M_t, indicating that regions of low and high pressure are more probable at low and high M_t respectively. The individual effect of solenoidal and dilatational motions were investigated to understand this behavior. The tails of the p.d.f. of enstrophy, a quantity that can be attributed to the solenoidal velocity field based on the Helmholtz decomposition, become narrower with increasing M_t suggesting that regions of high-enstrophy become less probable with increasing compressibility. At low M_t, the pressure fluctuations are predominantly solenoidal, and we thus see low-pressure and high-enstrophy regions to be correlated, similar to incompressible turbulence. However, at high M_t, this correla-

tion decreases significantly. We have found that this change in skewness, and the de-correlation between enstrophy and dilatation, is due to the dilatational pressure fluctuations which reaches the same order of magnitude as that of its solenoidal counterpart at high M_t. Strong local expansions at high M_t are also associated with regions of high-pressure, where the density-temperature correlation is significant. At low M_t, both local compressions and expansions appear in regions of low pressure with negligible contribution from the density-temperature correlation. This change in skewness of pressure also affects the overall energy exchanges in the flow affecting the global dynamics. While the net energy transfer for a strong compression at low M_t could be internal to kinetic or vice-versa, at high M_t, this is more likely to be from kinetic to internal energy since both pressure-dilatational and dissipation tend to transfer energy in that direction.

When the dilatational mode is forced, the attainable Reynolds number is seen to be significantly lower than its solenoidal counterpart. The asymptotic state of the normalized energy dissipation rate, $D = \langle\epsilon\rangle L/u^3$, seems to be consistent with the solenoidally forced cases. The contribution of the dilatational component of dissipation, D_d is seen to be significantly higher than its solenoidal counterpart, D_s, such that their sum is close to D. The scaling of length scales on the other hand are affected by the type of forcing. The integral length scales seem to show minor dependence on the type of forcing while only a weak dependence is seen for the Taylor microscales and the scaling of velocity scales.

Two scaling parameters, χ and M_t^d, that denote the fraction of dilatational kinetic energy and the potential energy (due to dilatational pressure), were proposed

to scale some basic statistics regardless of the mode of forcing. The latter is based on the assumption that the acoustic pressure and particle velocity can be approximated by the dilatational pressure and velocity respectively. The DNS data supports this assumption for the range of R_λ and M_t investigated. As a result of this assumption, the equipartition of energy is seen to be naturally valid, which is also supported by the data.

The scaling of r.m.s. fluctuations of thermodynamic variables normalized by their mean is seen to qualitatively vary as $M_t^{d\,3/4}$ for both solenoidal and dilatational forcing. The solenoidal pressure is seen to be only weakly dependent on R_λ, M_t and the mode of forcing, while the dilatational pressure and its correlation with the solenoidal counterpart is seen to vary as M_t^d and $-0.98M_t^{d\,0.81}$ regardless of the type of forcing. The p.d.f. of pressure, which was observed to be positively skewed beyond $M_t \approx 0.3$, can become so at a smaller M_t when the dilatational mode is forced. This transition happens around $\chi \approx 0.01$ (which corresponds to $M_t^d \approx 0.03$) which may be universal regardless of the type of forcing. Beyond this threshold, we found that the skewness of pressure varies as $\log \chi$ with very little dependence on the nature of forcing, indicating a possible universal behavior. This positive skewness of pressure beyond a threshold is also seen to change the way energy is exchanged between internal and kinetic energies. We have also shown that the current decomposition of pressure into a solenoidal and dilatational component is useful in delineating the effects of compressibility where the solenoidal component is less affected by forcing, R_λ or M_t, while the dilatational component is seen to be dependent on M_t^d and thus including the effect of compressibility.

VI.B. Future Research Directions

In this section, we discuss some possible research directions that can be continued from the current work. We divide this section into computational and physics of compressible turbulence.

VI.B.1. Computational

- As mentioned before, the code has shown good strong scaling up-to 262,144 processors. However, at large core counts, the time spent in communication is more than 50%. This can be hidden by overlapping computations and communications such that while the communication is in progress, the part of the code that do not require the variables that are being communicated can begin to compute on other variables.

- While using multiple levels of parallelism has shown to decrease the communication time, the maximum number of threads that could potentially improve performance is only two. This could be optimized, for instance, by maintaining a higher load acorss each thread, such that the scalability is also improved on-core, and may be more beneficial in newer architechtures such as Intel Xeon-Phi that have performance benefits for hybrid codes.

- Due to the recent proliferation of GPUs in supercomputers and their purported performance improvements in some cases, it may also be useful to add capabilities to the code such that a hybrid GPU-MPI based parallelism is possible.

VI.B.2. Physics of Compressible Turbulence

- The fundamental understanding of energy cascade process that is well established in incompressible turbulence is still lacking in compressible flows. The massive amount of high resolution DNS data that is available at high R_λ and M_t from this work can be used in this respect to improve the understanding of how the energy cascade occurs, for instance, when the dilatational mode is excited. Bataille *et al.* (1997) proposed that the dilatational mode cascades separately at high M_t. While our energy spectra support this claim, further efforts are needed in this direction to conclusively establish if there is a energy cascade process for the dilatational mode.

- While it is commonly believed that a universal scaling in compressible flows is much harder to achieve than incompressible turbulence, our DNS data seems to indicate the possibility of an existence of such a state. Hence, it would be very useful to understand from a theoretical perspective, as to what drives the system towards a universal state. We proposed two scaling parameters χ and M_t^d that independently scale thermodynamic quantities. It may also be of interest to perform a low-parameter expansion of the Navier-Stokes equations for these two parameters to understand if two different regimes where compressibility effects are small and significantly can be identified. If such a regime can be found, the threshold for the transition that we observed can be ascertained.

- Though some of the scaling relations seem independent of the mode of forcing, it is necessary to ascertain that this is also independent of the way energy

is added at the large scales. For instance, in the present work, a stochastic forcing is implemented to independently force the solenoidal and dilatation components. It would be important to understand, how the scaling relations are affected by the type of forcing, if forced deterministically or by maintaining a fixed energy spectra similar to incompressible turbulence or a linear forcing (Rosales & Meneveau, 2005).

- The energy interaction between internal and kinetic energy is still not well-explored in compressible turbulence. While we have shown that dilatation of the fluid and the fraction of dilatational kinetic energy are important in determining the likelihood of direction of energy transfer, a more theoretical approach is necessary to understand how this process happens.

- A prominent difference between incompressible and compressible flows at high M_t seems to be the presence of high-pressure regions and a weakening correlation between pressure and enstrophy in the latter. While we have identified that expansions and high-pressure regions tend to co-exist, the exact physical processes behind would be beneficial to the general understanding of the compressible flows.

REFERENCES

Bataille, F., Zhou, Y. & Bertoglio, J. P. 1997 Energy transfer and triadic interactions in compressible turbulence. *Tech. Rep.*. Defense Technical Information Center Document.

Bertoglio, J. P., Bataille, F. & Marion, J. D. 2001 Two-point closures for weakly compressible turbulence. *Phys. Fluids* **13**, 290.

Bertsch, R. L., Suman, S. & Girimaji, S. S. 2012 Rapid distortion analysis of high mach number homogeneous shear flows: Characterization of flow-thermodynamics interaction regimes. *Phys. Fluids* **24** (12), 125106.

Blaisdell, G. A., Mansour, N. N. & Reynolds, W. C. 1993 Compressibility effects on the growth and structure of homogeneous turbulent shear flow. *J. Fluid Mech.* **256** (1), 443–485.

Blaisdell, G. A., Spyropoulos, E. T. & Qin, J. H. 1996 The effect of the formulation of nonlinear terms on aliasing errors in spectral methods. *Appl. Num. Math.* **21** (3), 207–219.

Blaisdell, G. A. & Zeman, O. 1992 Investigation of the dilatational dissipation in compressible homogeneous shear flow. In *Studying Turbulence Using Numerical Simulation Databases* (ed. D. Spinks), pp. 231–245.

Canuto, C., Hussaini, M. Y., Quarteroni, A. & Zang, T. A. 1988 *Spectral Methods in Fluid Dynamics*. Springer Berlin Heidelberg.

Cao, N. Z., Chen, S. Y. & Doolen, G. D. 1999 Statistics and structures of pressure in isotropic turbulence. *Phys. Fluids* **11**, 2235–2250.

Chu, B. T. & Kovásznay, L. S. G. 1958 Non-linear interactions in a viscous heat-conducting compressible gas. *J. Fluid Mech.* **3** (05), 494–514.

Cook, A.W., Cabot, W.H., Williams, P.L., Miller, B.J., De Supinski, B.R., Yates, R.K. & Welcome, M.L. 2005 Tera-scalable algorithms for variable-density elliptic hydrodynamics with spectral accuracy. In *Supercomputing, 2005. Proceedings of the ACM/IEEE SC 2005 Conference*, pp. 60–60. Seattle, WA.

Dastgeer, S. & Zank, G. P. 2005 Turbulence in nearly incompressible fluids: density spectrum, flows, correlations and implication to the interstellar medium. *Nonlinear Processes in Geophysics* **12**, 139–148.

Donzis, D. A. & Jagannathan, S 2013*a* Fluctuations of thermodynamic variables in stationary compressible turbulence. *J. Fluid Mech.* **733**, 221–244.

Donzis, D. A. & Jagannathan, S 2013*b* On the relation between small-scale intermittency and shocks in turbulent flows. *Procedia IUTAM* **9**, 3–15.

Donzis, D. A. & Sreenivasan, K. R. 2010*a* The bottleneck effect and the Kolmogorov constant in isotropic turbulence. *J. Fluid Mech.* **657**, 171–188.

Donzis, D. A. & Sreenivasan, K. R. 2010*b* Short-term forecasts and scaling of intense events in turbulence. *J. Fluid Mech.* **647**, 13–26.

Donzis, D. A., Sreenivasan, K. R. & Yeung, P. K. 2005 Scalar dissipation rate and dissipative anomaly in isotropic turbulence. *J. Fluid Mech.* **532**, 199–216.

Donzis, D. A., Sreenivasan, K. R. & Yeung, P. K. 2012 Some results on the Reynolds number scaling of pressure statistics in isotropic turbulence. *Physica D* **241**, 164 – 168.

Donzis, D. A. & Yeung, P. K. 2010 Resolution effects and scaling in numerical simulations of passive scalar mixing in turbulence. *Physica D* **239**, 1278–1287.

Donzis, D. A., Yeung, P. K. & Pekurovsky, D. 2008*a* Turbulence simulations on $O(10^4)$ processors. In *TeraGrid 2008 Conference*. Las Vegas, NV.

Donzis, D. A., Yeung, P. K. & Sreenivasan, K. R. 2008*b* Dissipation and enstrophy in isotropic turbulence: scaling and resolution effects in direct numerical simulations. *Phys. Fluids* **20**, 045108.

Ducros, F., Laporte, F., Soulres, T., Guinot, V., Moinat, P. & Caruelle, B. 2000 High-order fluxes for conservative skew-symmetric-like schemes in structured meshes: Application to compressible flows. *J. Comp. Phys.* **161** (1), 114–139.

Erlebacher, G., Hussaini, M. Y., Kreiss, H. O. & Sarkar, S. 1990 The analysis and simulation of compressible turbulence. *Theoret. Comput. Fluid Dynamics* **2** (2), 73–95.

Eswaran, V. & Pope, S. B. 1988 An examination of forcing in direct numerical simulations of turbulence. *Comput. Fluids* **16**, 257–278.

Fauchet, G. & Bertoglio, J.P. 1998 An analytical expression for the spectrum of compressible turbulence in the low mach number limit. In *Advances in Turbulence VII* (ed. Uriel Frisch), *Fluid Mechanics and Its Applications*, vol. 46, pp. 317–320. Springer Netherlands.

Federrath, C., Klessen, R. S. & Schmidt, W. 2009 The fractal density structure in supersonic isothermal turbulence: solenoidal versus compressive energy injection. *Astrophys. J.* **692**, 364–374.

Fornberg, B. 1998 Calculation of weights in finite difference formulas. *SIAM Rev.* **40** (3), 685–691.

Gamet, L., Ducros, F., Nicoud, F. & Poinsot, T. 1999 Compact finite difference schemes on non-uniform meshes. Application to direct numerical simulations of compressible flows. *Int. J. Numer. Meth. Fluids* **29** (2), 159–191.

Holzer, M. & Siggia, E. 1993 Skewed, exponential pressure distributions from gaussian velocities. *Physics of Fluids A: Fluid Dynamics* **5** (10), 2525–2532.

Howe, M. S. 2003 *Theory of Vortex Sound*. Cambridge University Press Cambridge.

Ishihara, T., Gotoh, T. & Kaneda, Y. 2009 Study of high-Reynolds number isotropic turbulence by direct numerical simulation. *Annu. Rev. Fluid Mech.* **41**, 165–180.

Jagannathan, S. & Donzis, D. A. 2012 Massively parallel direct numerical simulations of forced compressible turbulence: a hybrid MPI/OpenMP approach. In *XSEDE 2012 Conference*. Chicago, IL.

Kaneda, Y., Ishihara, T., Yokokawa, M., Itakura, K. & Uno, A. 2003 Energy dissipation rate and energy spectrum in high resolution direct numerical simulations of turbulence in a periodic box. *Phys. Fluids* **15** (2), L21–L24.

Kida, S. & Orszag, S. A. 1990 Energy and spectral dynamics in forced compressible turbulence. *J. Sci. Comp.* **5**, 85–125.

Kolmogorov, A. N. 1941 Local structure of turbulence in an incompressible fluid for very large reynolds numbers. *Dokl. Akad. Nauk. SSSR* **30**, 299–303.

Kovasznay, L. S. G. 1953 Turbulence in supersonic flow. *J. Aeronaut. Sci.* **20** (10), 657–674.

Kraichnan, R. H 1955 On the statistical mechanics of an adiabatically compressible fluid. *The Journal of the Acoustical Society of America* **27** (3), 438–441.

Lee, Kurnchul & Girimaji, SharathS. 2013 Flow-thermodynamics interactions in decaying anisotropic compressible turbulence with imposed temperature fluctuations. *Theoretical and Computational Fluid Dynamics* **27** (1-2), 115–131.

Lee, K., Girimaji, S. S. & Kerimo, J. 2009 Effect of compressibility on turbulent velocity gradients and small-scale structure. *J. Turbul.* **10**, 1–18.

Lee, S., Lele, S. K. & Moin, P. 1991 Eddy shocklets in decaying compressible turbulence. *Phys. Fluids* **3**, 657–664.

Lee, S., Lele, S. K. & Moin, P. 1993 Direct numerical simulation of isotropic turbulence interacting with a weak shock wave. *J. Fluid Mech.* **251**, 533–562.

Lele, S. K. 1992 Compact finite-difference schemes with spectral-like resolution. *J. Comp. Phys.* **103**, 16–42.

Lele, S. K. 1994 Compressibility effects on turbulence. *Annu. Rev. Fluid Mech.* **26**, 211–254.

Livescu, D., Jaberi, F. A. & Madnia, C. K. 2002 The effects of heat release on the energy exchange in reacting turbulent shear flow. *J. Fluid Mech.* **450** (-1), 35–66.

Lv, X-G. & Le, J. 2008 A note on solving nearly penta-diagonal linear systems. *Appl. Math. Comput.* **204**, 707–712.

Mahesh, K. 1996 The interaction of a shock wave with a turbulent shear flow. PhD thesis, Stanford University, Stanford.

Mininni, P. D., Rosenberg, D., Reddy, R. & Pouquet, A. 2011 A hybrid MPI-OpenMP scheme for scalable parallel pseudospectral computations for fluid turbulence. *Parall. Comp.* **37** (6-7), 316–326.

Miura, H. & Kida, S. 1995 Acoustic energy exchange in compressible turbulence. *Phys. Fluids* **7** (7), 1732–1742.

Moin, P. & Mahesh, K. 1998 Direct numerical simulation: A tool in turbulence research. *Annu. Rev. Fluid Mech.* **30**, 539–578.

Monin, A. S. & Yaglom, A. M. 1975 *Statistical Fluid Mechanics, Vol. II*. MIT Press, Cambirdge.

Nomura, K. K. & Post, G. K. 1998 The structure and dynamics of vorticity and rate of strain in incompressible homogeneous turbulence. *J. Fluid Mech.* **377**, 65–97.

Overholt, M. R. & Pope, S. B. 1996 Direct numerical simulation of a passive scalar with imposed mean gradient in isotropic turbulence. *Phys. Fluids* **8**, 3128–3148.

Overholt, M. R. & Pope, S. B. 1998 A deterministic forcing scheme for direct numerical simulations of turbulence. *Comput. Fluids* **27**, 11–28.

Pearson, B. R., Yousef, T. A., Haugen, N. E. L, Brandenburg, A. & Krogstad, P. 2004 Delayed correlation between turbulent energy injection and dissipation. *Phys. Rev. E* **70** (5), 056301.

Petersen, M. R. & Livescu, D. 2010 Forcing for statistically stationary compressible isotropic turbulence. *Phys. Fluids* **22**, 116101.

Pirozzoli, S. & Grasso, F. 2004 Direct numerical simulations of isotropic compressible turbulence: Influence of compressibility on dynamics and structures. *Phys. Fluids* **16**, 4386 – 4407.

Pumir, A. 1994 A numerical study of pressure fluctuations in three-dimensional, incompressible, homogeneous, isotropic turbulence. *Phys. Fluids* **6**, 2071.

Ristorcelli, JR 1997 A pseudo-sound constitutive relationship for the dilatational covariances in compressible turbulence. *J. Fluid Mech.* **347**, 37–70.

Rosales, C. & Meneveau, C. 2005 Linear forcing in numerical simulations of isotropic turbulence: Physical space implementations and convergence properties. *Phys. Fluids* **17**, 095106.

Sagaut, P. & Cambon, C. 2008 *Homogeneous Turbulence Dynamics*. Cambridge University Press Cambridge.

Samtaney, R., Pullin, D. I. & Kosovic, B. 2001 Direct numerical simulation of decaying compressible turbulence and shocklet statistics. *Phys. Fluids* **13**, 1415.

Sarkar, S. 1992 The pressure-dilatation correlation in compressible flows. *Physics of Fluids A: Fluid Dynamics* **4** (12), 2674–2682.

Sarkar, S., Erlebacher, G., Hussaini, M. Y. & Kreiss, H. O. 1991 The analysis and modelling of dilatational terms in compressible turbulence. *J. Fluid Mech.* **227**, 473–493.

Schmidt, W., Hillebrandt, W. & Niemeyer, J.C. 2006 Numerical dissipation and the bottleneck effect in simulations of compressible isotropic turbulence. *Comput. Fluids* **35** (4), 353–371.

Shivamoggi, BK 1997 Equilibrium statistical mechanics of compressible isotropic turbulence. *Europhys. Lett.* **38** (9), 657–662.

Sreenivasan, K. R. 1984 On the scaling of the turbulence energy-dissipation rate. *Phys. Fluids* **27**, 1048–1051.

Sreenivasan, K. R. 1995 On the universality of the Kolmogorov constant. *Phys. Fluids* **7** (11), 2778–2784.

Sreenivasan, K. R. 1998 An update on the energy dissipation rate in isotropic turbulence. *Phys. Fluids* **10**, 528–529.

Sreenivasan, K. R. & Antonia, R. A. 1997 The phenomenology of small-scale turbulence. *Annu. Rev. Fluid Mech.* **29**, 435–472.

Suman, S. & Girimaji, S. S. 2013 Velocity gradient dynamics in compressible turbulence: Characterization of pressure-hessian tensor. *Phys. Fluids* **25** (12), 125103.

Vedula, P. & Yeung, P. K. 1999 Similarity scaling of acceleration and pressure statistics in numerical simulations of isotropic turbulence. *Phys. Fluids* **11**, 1208–1220.

Vreman, A. W., Sandham, N. D. & Luo, K. H. 1996 Compressible mixing layer growth rate and turbulence characteristics. *J. Fluid Mech.* **320** (1), 235–258.

Wang, J., Shi, Y., Wang, L.P., Xiao, Z., He, XT & Chen, S. 2012 Effect of compressibility on the small-scale structures in isotropic turbulence. *J. Fluid Mech.* **1** (1), 1–44.

Wang, J., Wang, L.-P., Xiao, Z., Shi, Y. & Chen, S. 2010 A hybrid numerical simulation of isotropic compressible turbulence. *J. Comp. Phys.* **229**, 5257 – 5279.

Watanabe, T. & Gotoh, T. 2007 Inertial-range intermittency and accuracy of direct numerical simulation for turbulence and passive scalar turbulence. *J. Fluid Mech.* **590**, 117–146.

Williamson, J. H. 1980 Low-storage Runge-Kutta schemes. *J. Comp. Phys.* **35**, 48 – 56.

Yeung, P. K., Xu, S. & Sreenivasan, K. R. 2002 Schmidt number effects on turbulent transport with uniform mean scalar gradient. *Phys. Fluids* **14**, 4178–4191.

Yilmaz, E., Payli, R. U., Akay, H. U. & Ecer, A. 2009 Hybrid parallelism for CFD simulations: Combining MPI with OpenMP. In *Parallel Computational Fluid Dynamics 2007*, *Lecture Notes in Computational Science and Engineering*, vol. 67, pp. 401–408. Springer Berlin Heidelberg.

Zeman, O. 1990 Dilatation dissipation: The concept and application in modeling compressible mixing layers. *Physics of Fluids A: Fluid Dynamics* **2** (2), 178–188.

APPENDIX A

GOVERNING EQUATIONS AS IMPLEMENTED IN CDNS

A.1. Stress Tensor Relations

$$\tau_{xx} = \frac{2}{3}\mu\left(2\frac{\partial u}{\partial x} - \frac{\partial v}{\partial y} - \frac{\partial w}{\partial z}\right) \tag{A.1a}$$

$$\tau_{yy} = \frac{2}{3}\mu\left(2\frac{\partial v}{\partial y} - \frac{\partial u}{\partial x} - \frac{\partial w}{\partial z}\right) \tag{A.1b}$$

$$\tau_{zz} = \frac{2}{3}\mu\left(2\frac{\partial w}{\partial z} - \frac{\partial u}{\partial x} - \frac{\partial v}{\partial y}\right) \tag{A.1c}$$

$$\tau_{xy} = \mu\left(\frac{\partial u}{\partial y} + \frac{\partial v}{\partial x}\right) = \tau_{yx} \tag{A.1d}$$

$$\tau_{xz} = \mu\left(\frac{\partial w}{\partial x} + \frac{\partial u}{\partial z}\right) = \tau_{zx} \tag{A.1e}$$

$$\tau_{yz} = \mu\left(\frac{\partial v}{\partial z} + \frac{\partial w}{\partial y}\right) = \tau_{zy} \tag{A.1f}$$

A.2. Energy Equation Relations

$$\rho\frac{De}{Dt} + p\left(\nabla \cdot \mathbf{V}\right) = \frac{\partial Q}{\partial t} - \nabla \cdot \mathbf{q} + \Phi \tag{A.2}$$

$$T = \frac{(\gamma - 1)e}{R} \quad p = (\gamma - 1)\rho e \tag{A.3}$$

$$e = c_v T \quad h = c_p T \quad \gamma = \frac{c_p}{c_v} \quad c_v = \frac{R}{\gamma - 1} \quad c_p = \frac{\gamma R}{\gamma - 1} \tag{A.4}$$

$$\mu = C_1 \frac{T^{3/2}}{T + C_2} \quad k = C_3 \frac{T^{3/2}}{T + C_4} \tag{A.5}$$

$$p = \rho R T \quad Pr = \frac{c_p \mu}{k} \tag{A.6}$$

$$\begin{aligned} \frac{\partial}{\partial t}(\rho e) + \frac{\partial}{\partial x}(\rho u e) + \frac{\partial}{\partial y}(\rho v e) + \frac{\partial}{\partial z}(\rho w e) + p\left(\frac{\partial u}{\partial x} + \frac{\partial v}{\partial y} + \frac{\partial w}{\partial z}\right) = \\ \frac{\partial Q}{\partial t} - \left(\frac{\partial q_x}{\partial x} + \frac{\partial q_y}{\partial y} + \frac{\partial q_z}{\partial z}\right) + \Phi \end{aligned} \tag{A.7}$$

$$\frac{\partial}{\partial x}(\rho u e) = \frac{1}{2}\left[\frac{\partial}{\partial x}(\rho u e) + \rho u \frac{\partial e}{\partial x} + e\frac{\partial \rho u}{\partial x}\right] \tag{A.8}$$

$$\frac{\partial}{\partial y}(\rho v e) = \frac{1}{2}\left[\frac{\partial}{\partial y}(\rho v e) + \rho v \frac{\partial e}{\partial y} + e\frac{\partial \rho v}{\partial y}\right] \tag{A.9}$$

$$\frac{\partial}{\partial z}(\rho w e) = \frac{1}{2}\left[\frac{\partial}{\partial z}(\rho w e) + \rho w \frac{\partial e}{\partial z} + e\frac{\partial \rho w}{\partial z}\right] \tag{A.10}$$

$$\mathbf{q} = \left(-k\frac{\partial T}{\partial x}, -k\frac{\partial T}{\partial y}, -k\frac{\partial T}{\partial z}\right) \tag{A.11}$$

$$\begin{aligned} \nabla \cdot \mathbf{q} = -\Bigg[\frac{\partial k}{\partial T}\left(\frac{\partial T}{\partial x}\right)^2 + k\frac{\partial^2 T}{\partial x^2} + \frac{\partial k}{\partial T}\left(\frac{\partial T}{\partial y}\right)^2 + k\frac{\partial^2 T}{\partial y^2} \\ + \frac{\partial k}{\partial T}\left(\frac{\partial T}{\partial z}\right)^2 + k\frac{\partial^2 T}{\partial z^2}\Bigg] \end{aligned} \tag{A.12}$$

$$\begin{aligned} \Phi = \mu\Bigg[2\left(\frac{\partial u}{\partial x}\right)^2 + 2\left(\frac{\partial v}{\partial y}\right)^2 + 2\left(\frac{\partial w}{\partial z}\right)^2 + \left(\frac{\partial v}{\partial x} + \frac{\partial u}{\partial y}\right)^2 + \left(\frac{\partial w}{\partial y} + \frac{\partial v}{\partial z}\right)^2 \\ + \left(\frac{\partial u}{\partial z} + \frac{\partial w}{\partial x}\right)^2 - \frac{2}{3}\left(\frac{\partial u}{\partial x} + \frac{\partial v}{\partial y} + \frac{\partial w}{\partial z}\right)^2\Bigg] \end{aligned} \tag{A.13}$$

$$\Phi = \mu\left[\frac{4}{3}\left(\frac{\partial u}{\partial x}\right)^2 + \frac{4}{3}\left(\frac{\partial v}{\partial y}\right)^2 + \frac{4}{3}\left(\frac{\partial w}{\partial z}\right)^2 + \left(\frac{\partial v}{\partial x}\right)^2 + \left(\frac{\partial u}{\partial y}\right)^2 + 2\left(\frac{\partial v}{\partial x}\frac{\partial u}{\partial y}\right) + \left(\frac{\partial w}{\partial y}\right)^2 + \left(\frac{\partial v}{\partial z}\right)^2 + 2\left(\frac{\partial w}{\partial y}\frac{\partial v}{\partial z}\right) + \left(\frac{\partial u}{\partial z}\right)^2 + \left(\frac{\partial w}{\partial x}\right)^2 + 2\left(\frac{\partial u}{\partial z}\frac{\partial w}{\partial x}\right) - \frac{4}{3}\left(\frac{\partial u}{\partial x}\frac{\partial v}{\partial y} + \frac{\partial v}{\partial y}\frac{\partial w}{\partial z} + \frac{\partial w}{\partial z}\frac{\partial u}{\partial x}\right)\right] \tag{A.14}$$

A.3. Vector Form of Equations

Energy Equation not included in the matrix. Note :

$$\nabla \cdot (\rho \mathbf{v}\mathbf{v}) = \frac{\partial}{\partial x_i}(\rho v_i v_j) \text{ in j direction} \tag{A.15}$$

$$E = \begin{bmatrix} \frac{\partial}{\partial x}(\rho uu + p - \tau_{xx}) \\ \frac{\partial}{\partial x}(\rho uv - \tau_{xy}) \\ \frac{\partial}{\partial x}(\rho uw - \tau_{xz}) \\ \frac{\partial}{\partial x}(\rho u) \end{bmatrix}$$

$$F = \begin{bmatrix} \frac{\partial}{\partial y}(\rho vu - \tau_{xy}) \\ \frac{\partial}{\partial y}(\rho vv + p - \tau_{yy}) \\ \frac{\partial}{\partial y}(\rho vw - \tau_{yz}) \\ \frac{\partial}{\partial y}(\rho v) \end{bmatrix}$$

$$G = \begin{bmatrix} \frac{\partial}{\partial z}\left(\rho w u - \tau_{xz}\right) \\ \frac{\partial}{\partial z}\left(\rho w v - \tau_{yz}\right) \\ \frac{\partial}{\partial z}\left(\rho w w + p - \tau_{zz}\right) \\ \frac{\partial}{\partial z}\left(\rho w\right) \end{bmatrix}$$

A.3.a. Skew Symmetric Formulation

$$\frac{\partial}{\partial x}\left(\rho u u\right) = \frac{1}{2}\left[\frac{\partial}{\partial x}\left(\rho u u\right) + \rho u \frac{\partial u}{\partial x} + u \frac{\partial \rho u}{\partial x}\right] \tag{A.16a}$$

$$\frac{\partial}{\partial x}\left(\rho u v\right) = \frac{1}{2}\left[\frac{\partial}{\partial x}\left(\rho u v\right) + \rho u \frac{\partial v}{\partial x} + v \frac{\partial \rho u}{\partial x}\right] \tag{A.16b}$$

$$\frac{\partial}{\partial x}\left(\rho u w\right) = \frac{1}{2}\left[\frac{\partial}{\partial x}\left(\rho u w\right) + \rho u \frac{\partial w}{\partial x} + w \frac{\partial \rho u}{\partial x}\right] \tag{A.16c}$$

$$\frac{\partial}{\partial y}\left(\rho v u\right) = \frac{1}{2}\left[\frac{\partial}{\partial y}\left(\rho v u\right) + \rho v \frac{\partial u}{\partial y} + u \frac{\partial \rho v}{\partial y}\right] \tag{A.16d}$$

$$\frac{\partial}{\partial y}\left(\rho v v\right) = \frac{1}{2}\left[\frac{\partial}{\partial y}\left(\rho v v\right) + \rho v \frac{\partial v}{\partial y} + v \frac{\partial \rho v}{\partial y}\right] \tag{A.16e}$$

$$\frac{\partial}{\partial y}\left(\rho v w\right) = \frac{1}{2}\left[\frac{\partial}{\partial y}\left(\rho v w\right) + \rho v \frac{\partial w}{\partial y} + w \frac{\partial \rho v}{\partial y}\right] \tag{A.16f}$$

$$\frac{\partial}{\partial z}\left(\rho w u\right) = \frac{1}{2}\left[\frac{\partial}{\partial z}\left(\rho w u\right) + \rho w \frac{\partial u}{\partial z} + u \frac{\partial \rho w}{\partial z}\right] \tag{A.16g}$$

$$\frac{\partial}{\partial z}(\rho w v) = \frac{1}{2}\left[\frac{\partial}{\partial z}(\rho w v) + \rho w \frac{\partial v}{\partial z} + v\frac{\partial \rho w}{\partial z}\right] \tag{A.16h}$$

$$\frac{\partial}{\partial z}(\rho w w) = \frac{1}{2}\left[\frac{\partial}{\partial z}(\rho w w) + \rho w \frac{\partial w}{\partial z} + w\frac{\partial \rho w}{\partial z}\right] \tag{A.16i}$$

A.3.b. X Direction

$$\frac{\partial}{\partial x}(\rho u u) + \frac{\partial}{\partial y}(\rho v u) + \frac{\partial}{\partial z}(\rho w u) \tag{A.17}$$

$$\begin{aligned}\frac{1}{2}\left[\frac{\partial}{\partial x}(\rho u u) + \rho u \frac{\partial u}{\partial x} + u\frac{\partial \rho u}{\partial x}\right] + \frac{1}{2}\left[\frac{\partial}{\partial y}(\rho v u) + \rho v \frac{\partial u}{\partial y} + u\frac{\partial \rho v}{\partial y}\right] \\ + \frac{1}{2}\left[\frac{\partial}{\partial z}(\rho w u) + \rho w \frac{\partial u}{\partial z} + u\frac{\partial \rho w}{\partial z}\right]\end{aligned} \tag{A.18}$$

A.3.c. Y Direction

$$\frac{\partial}{\partial x}(\rho u v) + \frac{\partial}{\partial y}(\rho v v) + \frac{\partial}{\partial z}(\rho w v) \tag{A.19}$$

$$\begin{aligned}\frac{1}{2}\left[\frac{\partial}{\partial x}(\rho u v) + \rho u \frac{\partial v}{\partial x} + v\frac{\partial \rho u}{\partial x}\right] + \frac{1}{2}\left[\frac{\partial}{\partial y}(\rho v v) + \rho v \frac{\partial v}{\partial y} + v\frac{\partial \rho v}{\partial y}\right] \\ + \frac{1}{2}\left[\frac{\partial}{\partial z}(\rho w v) + \rho w \frac{\partial v}{\partial z} + v\frac{\partial \rho w}{\partial z}\right]\end{aligned} \tag{A.20}$$

A.3.d. Z Direction

$$\frac{\partial}{\partial x}(\rho u w) + \frac{\partial}{\partial y}(\rho v w) + \frac{\partial}{\partial z}(\rho w w) \tag{A.21}$$

$$\frac{1}{2}\left[\frac{\partial}{\partial x}(\rho u w)+\rho u\frac{\partial w}{\partial x}+w\frac{\partial \rho u}{\partial x}\right]+\frac{1}{2}\left[\frac{\partial}{\partial y}(\rho v w)+\rho v\frac{\partial w}{\partial y}+w\frac{\partial \rho v}{\partial y}\right] +\frac{1}{2}\left[\frac{\partial}{\partial z}(\rho w w)+\rho w\frac{\partial w}{\partial z}+w\frac{\partial \rho w}{\partial z}\right] \tag{A.22}$$

A.4. Viscous Terms

A.4.a. X Direction

$$-\left[\frac{\partial \tau_{xx}}{\partial x}+\frac{\partial \tau_{xy}}{\partial y}+\frac{\partial \tau_{xz}}{\partial z}\right] \tag{A.23}$$

Skip the negative sign and include it in the end.

$$=\left[\frac{\partial}{\partial x}\left(\frac{4\mu}{3}\frac{\partial u}{\partial x}-\frac{2\mu}{3}\frac{\partial v}{\partial y}-\frac{2\mu}{3}\frac{\partial w}{\partial z}\right)+\frac{\partial}{\partial y}\left(\mu\frac{\partial u}{\partial y}+\mu\frac{\partial v}{\partial x}\right)+\frac{\partial}{\partial z}\left(\mu\frac{\partial w}{\partial x}+\mu\frac{\partial u}{\partial z}\right)\right] \tag{A.24}$$

A.4.a.i. Properties not constant

$$\begin{aligned}=\frac{4}{3}\left[\frac{\partial \mu}{\partial T}\frac{\partial T}{\partial x}\frac{\partial u}{\partial x}+\mu\frac{\partial^2 u}{\partial x^2}\right]-\frac{2}{3}\left[\frac{\partial \mu}{\partial T}\frac{\partial T}{\partial x}\frac{\partial v}{\partial y}+\mu\frac{\partial}{\partial y}\left(\frac{\partial v}{\partial x}\right)\right]\\ -\frac{2}{3}\left[\frac{\partial \mu}{\partial T}\frac{\partial T}{\partial x}\frac{\partial w}{\partial z}+\mu\frac{\partial}{\partial z}\left(\frac{\partial w}{\partial x}\right)\right]+\left[\frac{\partial \mu}{\partial T}\frac{\partial T}{\partial y}\frac{\partial v}{\partial x}+\mu\frac{\partial}{\partial y}\left(\frac{\partial v}{\partial x}\right)\right]\\ +\left[\frac{\partial \mu}{\partial T}\frac{\partial T}{\partial y}\frac{\partial u}{\partial y}+\mu\frac{\partial}{\partial y}\left(\frac{\partial u}{\partial y}\right)\right]+\left[\frac{\partial \mu}{\partial T}\frac{\partial T}{\partial z}\frac{\partial w}{\partial x}+\mu\frac{\partial}{\partial z}\left(\frac{\partial w}{\partial x}\right)\right]\\ +\left[\frac{\partial \mu}{\partial T}\frac{\partial T}{\partial z}\frac{\partial u}{\partial z}+\mu\frac{\partial}{\partial z}\left(\frac{\partial w}{\partial z}\right)\right]\end{aligned} \tag{A.25a}$$

Final form of equations :

$$= \left[\frac{4}{3}\left(\frac{\partial\mu}{\partial T}\frac{\partial T}{\partial x}\frac{\partial u}{\partial x}\right) - \frac{2}{3}\left(\frac{\partial\mu}{\partial T}\frac{\partial T}{\partial x}\frac{\partial v}{\partial y}\right) - \frac{2}{3}\left(\frac{\partial\mu}{\partial T}\frac{\partial T}{\partial x}\frac{\partial w}{\partial z}\right)\right] + \left[\mu\frac{\partial^2 u}{\partial y^2} + \mu\frac{\partial^2 u}{\partial z^2}\right] + \left[\frac{\partial\mu}{\partial T}\frac{\partial T}{\partial z}\frac{\partial w}{\partial x} + \frac{\partial\mu}{\partial T}\frac{\partial T}{\partial z}\frac{\partial u}{\partial z}\right] + \left[\frac{4}{3}\mu\frac{\partial^2 u}{\partial x^2} + \frac{1}{3}\mu\frac{\partial}{\partial y}\left(\frac{\partial v}{\partial x}\right) + \frac{1}{3}\mu\frac{\partial}{\partial z}\left(\frac{\partial w}{\partial x}\right)\right] + \left[\frac{\partial\mu}{\partial T}\frac{\partial T}{\partial y}\frac{\partial u}{\partial y} + \frac{\partial\mu}{\partial T}\frac{\partial T}{\partial y}\frac{\partial v}{\partial x}\right] \tag{A.25b}$$

A.4.a.ii. Constant Properties

$$\mu\left[\frac{4}{3}\frac{\partial^2 u}{\partial x^2} + \frac{\partial^2 u}{\partial y^2} + \frac{\partial^2 u}{\partial z^2}\right] + \frac{\mu}{3}\frac{\partial}{\partial y}\left(\frac{\partial v}{\partial x}\right) + \frac{\mu}{3}\frac{\partial}{\partial z}\left(\frac{\partial w}{\partial x}\right) \tag{A.26}$$

A.4.b. Y Direction

$$-\left[\frac{\partial\tau_{xy}}{\partial x} + \frac{\partial\tau_{yy}}{\partial y} + \frac{\partial\tau_{yz}}{\partial z}\right] \tag{A.27}$$

Skip the negative sign and include it in the end.

$$= \left[\frac{\partial}{\partial x}\left(\mu\frac{\partial u}{\partial y} + \mu\frac{\partial v}{\partial x}\right) + \frac{\partial}{\partial y}\left(\frac{4\mu}{3}\frac{\partial v}{\partial y} - \frac{2\mu}{3}\frac{\partial u}{\partial x} - \frac{2\mu}{3}\frac{\partial w}{\partial z}\right) + \frac{\partial}{\partial z}\left(\mu\frac{\partial v}{\partial z} + \mu\frac{\partial w}{\partial y}\right)\right] \tag{A.28}$$

A.4.b.i. Properties not constant

$$= \left[\frac{\partial \mu}{\partial T}\frac{\partial T}{\partial x}\frac{\partial u}{\partial y} + \mu\frac{\partial}{\partial y}\left(\frac{\partial u}{\partial x}\right)\right] + \left[\frac{\partial \mu}{\partial T}\frac{\partial T}{\partial x}\frac{\partial v}{\partial x} + \mu\frac{\partial^2 v}{\partial x^2}\right] + \frac{4}{3}\left[\frac{\partial \mu}{\partial T}\frac{\partial T}{\partial y}\frac{\partial v}{\partial y} + \mu\frac{\partial^2 v}{\partial y^2}\right] - \frac{2}{3}\left[\frac{\partial \mu}{\partial T}\frac{\partial T}{\partial y}\frac{\partial u}{\partial x} + \mu\frac{\partial}{\partial y}\left(\frac{\partial u}{\partial x}\right)\right] - \frac{2}{3}\left[\frac{\partial \mu}{\partial T}\frac{\partial T}{\partial y}\frac{\partial w}{\partial z} + \mu\frac{\partial}{\partial y}\left(\frac{\partial w}{\partial z}\right)\right] + \left[\frac{\partial \mu}{\partial T}\frac{\partial T}{\partial z}\frac{\partial v}{\partial z} + \mu\frac{\partial}{\partial z}\left(\frac{\partial v}{\partial z}\right)\right] + \left[\frac{\partial \mu}{\partial T}\frac{\partial T}{\partial z}\frac{\partial w}{\partial y} + \mu\frac{\partial}{\partial z}\left(\frac{\partial w}{\partial y}\right)\right] \tag{A.29a}$$

Final form of equations :

$$= \left[\frac{4}{3}\left(\frac{\partial \mu}{\partial T}\frac{\partial T}{\partial y}\frac{\partial v}{\partial y}\right) - \frac{2}{3}\left(\frac{\partial \mu}{\partial T}\frac{\partial T}{\partial y}\frac{\partial w}{\partial z}\right) - \frac{2}{3}\left(\frac{\partial \mu}{\partial T}\frac{\partial T}{\partial y}\frac{\partial u}{\partial x}\right)\right] + \left[\mu\frac{\partial^2 v}{\partial z^2} + \mu\frac{\partial^2 v}{\partial x^2}\right] + \left[\frac{\partial \mu}{\partial T}\frac{\partial T}{\partial z}\frac{\partial v}{\partial z} + \frac{\partial \mu}{\partial T}\frac{\partial T}{\partial z}\frac{\partial w}{\partial y}\right] + \left[\frac{4}{3}\mu\frac{\partial^2 v}{\partial y^2} + \frac{1}{3}\mu\frac{\partial}{\partial y}\left(\frac{\partial u}{\partial x}\right) + \frac{1}{3}\mu\frac{\partial}{\partial z}\left(\frac{\partial w}{\partial y}\right)\right] + \left[\frac{\partial \mu}{\partial T}\frac{\partial T}{\partial x}\frac{\partial u}{\partial y} + \frac{\partial \mu}{\partial T}\frac{\partial T}{\partial x}\frac{\partial v}{\partial x}\right] \tag{A.29b}$$

A.4.b.ii. Constant Properties

$$\mu\left[\frac{\partial^2 v}{\partial x^2} + \frac{4}{3}\frac{\partial^2 v}{\partial y^2} + \frac{\partial^2 v}{\partial z^2}\right] + \frac{\mu}{3}\frac{\partial}{\partial y}\left(\frac{\partial u}{\partial x}\right) + \frac{\mu}{3}\frac{\partial}{\partial z}\left(\frac{\partial w}{\partial y}\right) \tag{A.30}$$

A.4.c. Z Direction

$$-\left[\frac{\partial \tau_{xz}}{\partial x} + \frac{\partial \tau_{yz}}{\partial y} + \frac{\partial \tau_{zz}}{\partial z}\right] \tag{A.31a}$$

Skip the negative sign and include it in the end.

$$= \left[\frac{\partial}{\partial x}\left(\mu\frac{\partial w}{\partial x}+\mu\frac{\partial u}{\partial z}\right)+\frac{\partial}{\partial y}\left(\mu\frac{\partial v}{\partial z}+\mu\frac{\partial w}{\partial y}\right)+\frac{\partial}{\partial z}\left(\frac{4\mu}{3}\frac{\partial w}{\partial z}-\frac{2\mu}{3}\frac{\partial u}{\partial x}-\frac{2\mu}{3}\frac{\partial v}{\partial y}\right)\right] \tag{A.31b}$$

A.4.c.i. Properties not constant

$$\begin{aligned}= &\left[\frac{\partial\mu}{\partial T}\frac{\partial T}{\partial x}\frac{\partial w}{\partial x}+\mu\frac{\partial}{\partial x}\left(\frac{\partial w}{\partial x}\right)\right]+\left[\frac{\partial\mu}{\partial T}\frac{\partial T}{\partial x}\frac{\partial u}{\partial z}+\mu\frac{\partial}{\partial z}\left(\frac{\partial u}{\partial x}\right)\right]\\ &+\left[\frac{\partial\mu}{\partial T}\frac{\partial T}{\partial y}\frac{\partial v}{\partial z}+\mu\frac{\partial}{\partial z}\left(\frac{\partial v}{\partial y}\right)\right]+\left[\frac{\partial\mu}{\partial T}\frac{\partial T}{\partial y}\frac{\partial w}{\partial y}+\mu\frac{\partial}{\partial y}\left(\frac{\partial w}{\partial y}\right)\right]\\ &+\frac{4}{3}\left[\frac{\partial\mu}{\partial T}\frac{\partial T}{\partial z}\frac{\partial w}{\partial z}+\mu\frac{\partial^2 w}{\partial z^2}\right]-\frac{2}{3}\left[\frac{\partial\mu}{\partial T}\frac{\partial T}{\partial z}\frac{\partial u}{\partial x}+\mu\frac{\partial}{\partial z}\left(\frac{\partial u}{\partial x}\right)\right]\\ &-\frac{2}{3}\left[\frac{\partial\mu}{\partial T}\frac{\partial T}{\partial z}\frac{\partial v}{\partial y}+\mu\frac{\partial}{\partial z}\left(\frac{\partial v}{\partial y}\right)\right]\end{aligned} \tag{A.31c}$$

Final form of equations :

$$\begin{aligned}= &\left[\frac{4}{3}\left(\frac{\partial\mu}{\partial T}\frac{\partial T}{\partial z}\frac{\partial w}{\partial z}\right)-\frac{2}{3}\left(\frac{\partial\mu}{\partial T}\frac{\partial T}{\partial z}\frac{\partial u}{\partial x}\right)-\frac{2}{3}\left(\frac{\partial\mu}{\partial T}\frac{\partial T}{\partial z}\frac{\partial v}{\partial y}\right)\right]\\ &+\left[\mu\frac{\partial^2 w}{\partial x^2}+\mu\frac{\partial^2 w}{\partial y^2}\right]+\left[\frac{\partial\mu}{\partial T}\frac{\partial T}{\partial x}\frac{\partial w}{\partial x}+\frac{\partial\mu}{\partial T}\frac{\partial T}{\partial x}\frac{\partial u}{\partial z}\right]\\ &+\left[\frac{4}{3}\mu\frac{\partial^2 w}{\partial z^2}+\frac{1}{3}\mu\frac{\partial}{\partial z}\left(\frac{\partial u}{\partial x}\right)+\frac{1}{3}\mu\frac{\partial}{\partial z}\left(\frac{\partial v}{\partial y}\right)\right]\\ &+\left[\frac{\partial\mu}{\partial T}\frac{\partial T}{\partial y}\frac{\partial v}{\partial z}+\frac{\partial\mu}{\partial T}\frac{\partial T}{\partial y}\frac{\partial w}{\partial y}\right]\end{aligned} \tag{A.31d}$$

A.4.c.ii. Constant Properties

$$\mu\left[\frac{\partial^2 w}{\partial x^2}+\frac{\partial^2 w}{\partial y^2}+\frac{4}{3}\frac{\partial^2 w}{\partial z^2}\right]+\frac{\mu}{3}\frac{\partial}{\partial z}\left(\frac{\partial u}{\partial x}\right)+\frac{\mu}{3}\frac{\partial}{\partial z}\left(\frac{\partial v}{\partial y}\right) \tag{A.32}$$

A.5. Continuity Equation

$$\frac{\partial \rho}{\partial t} + \frac{\partial}{\partial x}(\rho u) + \frac{\partial}{\partial y}(\rho v) + \frac{\partial}{\partial z}(\rho w) = 0 \tag{A.33}$$

A.6. Scalars

$$\boxed{\frac{\partial}{\partial t}(\rho\phi) + \frac{\partial}{\partial x_i}(\rho\phi u_i) = \frac{\partial}{\partial x_i}\left(D\frac{\partial \phi}{\partial x_i}\right)} \tag{A.34}$$

$$\frac{\partial}{\partial t}(\rho\phi) + \frac{\partial}{\partial x}(\rho\phi u) + \frac{\partial}{\partial y}(\rho\phi v) + \frac{\partial}{\partial z}(\rho\phi w) = \frac{\partial}{\partial x}\left(D\frac{\partial \phi}{\partial x}\right) + \frac{\partial}{\partial y}\left(D\frac{\partial \phi}{\partial y}\right) + \frac{\partial}{\partial z}\left(D\frac{\partial \phi}{\partial z}\right) \tag{A.35}$$

$$\frac{\partial}{\partial x}(\rho\phi u) = \frac{1}{2}\left[\frac{\partial}{\partial x}(\rho\phi u) + \rho\phi\frac{\partial u}{\partial x} + u\frac{\partial \rho\phi}{\partial x}\right] \tag{A.36}$$

$$\frac{\partial}{\partial y}(\rho\phi u) = \frac{1}{2}\left[\frac{\partial}{\partial y}(\rho\phi v) + \rho\phi\frac{\partial v}{\partial y} + v\frac{\partial \rho\phi}{\partial y}\right] \tag{A.37}$$

$$\frac{\partial}{\partial z}(\rho\phi u) = \frac{1}{2}\left[\frac{\partial}{\partial z}(\rho\phi w) + \rho\phi\frac{\partial w}{\partial z} + w\frac{\partial \rho\phi}{\partial z}\right] \tag{A.38}$$

$$RHS = D\frac{\partial^2\phi}{\partial x^2} + \frac{\partial D}{\partial T}\frac{\partial T}{\partial x}\frac{\partial \phi}{\partial x} + D\frac{\partial^2\phi}{\partial y^2} + \frac{\partial D}{\partial T}\frac{\partial T}{\partial y}\frac{\partial \phi}{\partial y} + D\frac{\partial^2\phi}{\partial z^2} + \frac{\partial D}{\partial T}\frac{\partial T}{\partial z}\frac{\partial \phi}{\partial z} \tag{A.39}$$

Constant Diffusivity:

$$RHS = D\frac{\partial^2\phi}{\partial x^2} + D\frac{\partial^2\phi}{\partial y^2} + D\frac{\partial^2\phi}{\partial z^2} \tag{A.40}$$

A.6.a. Constant Mean Scalar Gradient

$$\phi = \langle\phi\rangle + \phi' \tag{A.41}$$

$$\frac{\partial}{\partial t}\left(\rho\langle\phi\rangle + \rho\phi'\right) + \frac{\partial}{\partial x_i}\left(\rho\langle\phi\rangle u_i + \rho\phi' u_i\right) = \frac{\partial}{\partial x_i}\left(D\frac{\partial}{\partial x_i}\left(\langle\phi\rangle + \phi'\right)\right) \tag{A.42}$$

$$\frac{\partial}{\partial t}\left(\rho\langle\phi\rangle\right) + \frac{\partial}{\partial t}\left(\rho\phi'\right) + \frac{\partial}{\partial x_i}\left(\rho\langle\phi\rangle u_i\right) + \frac{\partial}{\partial x_i}\left(\rho\phi' u_i\right) = \frac{\partial}{\partial x_i}\left(D\frac{\partial\langle\phi\rangle}{\partial x_i}\right) + \frac{\partial}{\partial x_i}\left(D\frac{\partial\phi'}{\partial x_i}\right) \tag{A.43}$$

$$\frac{\partial}{\partial t}\left(\rho\phi'\right) + \frac{\partial}{\partial x_i}\left(\rho\phi' u_i\right) + \rho\frac{\partial\langle\phi\rangle}{\partial t} + \langle\phi\rangle\frac{\partial\rho}{\partial t} + \langle\phi\rangle\frac{\partial}{\partial x_i}\left(\rho u_i\right) + \rho u_i\frac{\partial\langle\phi\rangle}{\partial x_i} = \text{RHS} \tag{A.44}$$

$$\text{RHS} = \frac{\partial}{\partial x_i}\left(D\frac{\partial\langle\phi\rangle}{\partial x_i}\right) + \frac{\partial}{\partial x_i}\left(D\frac{\partial\phi'}{\partial x_i}\right) \tag{A.45}$$

$$\text{Constant Mean scalar gradient: } \frac{\partial\langle\phi\rangle}{\partial t} = 0; \quad \frac{\partial\langle\phi\rangle}{\partial x_i} = \text{const}; \tag{A.46}$$

$$\text{Continuity: } \frac{\partial\rho}{\partial t} + \frac{\partial}{\partial x_i}\left(\rho u_i\right) = 0; \tag{A.47}$$

$$\boxed{\frac{\partial}{\partial t}\left(\rho\phi'\right) + \frac{\partial}{\partial x_i}\left(\rho\phi' u_i\right) = -\rho u_i\frac{\partial\langle\phi\rangle}{\partial x_i} + \frac{\partial\langle\phi\rangle}{\partial x_i}\frac{\partial D}{\partial T}\frac{\partial T}{\partial x_i} + \frac{\partial}{\partial x_i}\left(D\frac{\partial\phi'}{\partial x_i}\right)} \tag{A.48}$$

Compare the boxed Eqns. A.34 and A.48, then the "artificial forcing term" (only in isotropic turbulence with no mean gradients) can be attributed to the terms :

$$\frac{\partial\langle\phi\rangle}{\partial x_i}\frac{\partial D}{\partial T}\frac{\partial T}{\partial x_i}; \quad -\rho u_i\frac{\partial\langle\phi\rangle}{\partial x_i} \tag{A.49}$$

Final set of equations:

$$\boxed{\frac{\partial}{\partial t}\left(\rho\phi'\right)+\frac{\partial}{\partial x_i}\left(\rho\phi' u_i\right)=-\rho u_i\frac{\partial\langle\phi\rangle}{\partial x_i}+\frac{\partial\langle\phi\rangle}{\partial x_i}\frac{\partial D}{\partial T}\frac{\partial T}{\partial x_i}+\frac{\partial\phi'}{\partial x_i}\frac{\partial D}{\partial T}\frac{\partial T}{\partial x_i}+D\frac{\partial^2\phi'}{\partial {x_i}^2}} \tag{A.50}$$